Summer 2022

The Development of a Monolithic Spatial Heterodyne Spectrometer for Extreme Environments

Arelis Michelle Colón

THE DEVELOPMENT OF A MONOLITHIC SPATIAL HETERODYNE SPECTROMETER FOR EXTREME ENVIRONMENTS

by

Arelis Michelle Colón

Bachelor of Science
Alvernia University, 2018

Submitted in Partial Fulfillment of the Requirements

For Degree of Doctor of Philosophy in

Chemistry

College of Arts and Sciences

University of South Carolina

2022

Accepted by:

S. Michael Angel, Major Professor

John L. Ferry, Committee Member

Hui Wang, Committee Member

Alan W. Decho, Committee Member

J. Chance Carter, Committee Member

Tracey L. Weldon, Vice Provost and Dean of the Graduate School

DEDICATION

I dedicate this work to my mother Arelis Ortiz, my father Angel Colón II, and my brother Angel Colón III. I would not have accomplished what I did without all your support.

I would also like to dedicate this work to my soon to be husband Alex Harris. You always picked me back up when I was down, and you did not let me quit.

You all do not know how grateful and fortunate I am to have you.

ACKNOWLEDGEMENTS

Getting here was one of the most difficult endeavors and this would all not be possible without the help and support of many people. I would first like to thank my committee members Dr. John Ferry, Dr. Hui Wang, Dr. Alan Decho, and Dr. Chance Carter for challenging me and teaching me how to think more like a scientist. You all took the time to read my work and give the constructive feedback and critiques to help me advance and better myself in the sciences.

I would also like to thank my former lab mate Dr. Waldron for helping me survive the hardest part of grad school through a pandemic. You showed me so much patience and answered so many of my questions about my research and for that I am incredibly grateful. I would also like to thank Dr. Egan who took the time to answer my questions when he was on a time crunch to finish his research during his short visit to USC and for always being willing to take a phone call and have conversations about research. Along with my former lab mates would like to thank my current lab mate Mandy Agrawal. I learned so much from mentoring you.

Special shout out to my parents and my brother. You always kept me on track and reminded me who was when I was doubting myself. Although I lived so far away you always tried to visit as much as you could and give the me well needed morality boost. I would also like to thank the rest of my family and friends for always believing me and assuring me that I could accomplish anything I wanted to.

Thank to my fiancé and best friend Alex Harris. You were with me every step of the way and I would not have made it without you being there. You supported me and pushed me through the most difficult parts of my journey here. Thank you for listening to me and helping me decompress. Also, thank you for motivating me and letting me know daily that there are no challenges I cannot overcome. I already know you are going to tell me “I told you so,” and I will for once admit you were right.

I would also like to thank my undergraduate professor Dr. Chinni for encouraging me to go to grad school. I never envisioned myself earning a PhD, but you believed in me and inspired me to do it which I am truly grateful for.

Finally, my upmost gratitude goes to Dr. Angel. I learned so much from you and I am grateful for the patience you had with me. Thank you for always answering my questions and teaching me how to be a better scientist. You gave me such an amazing opportunity, and I will not forget the life lessons you taught me both research and non-research related lessons.

ABSTRACT

This work describes improvements to a novel instrument, the monolithic spatial heterodyne Raman spectrometer (mSHRS), which has potential to be utilized in space exploration and deep-ocean marine sensing. In previous work, the spatial heterodyne Raman spectrometer (SHRS) was demonstrated, as a small, high resolution, wide field of view spectrometer, originally developed for space applications where small size and compactness is a key consideration or where a wide field of view is advantageous, such as in remote spectroscopy. The spatial heterodyne spectrometer (SHS) was then later utilized for remote Laser-Induced Breakdown Spectroscopy (LIBS). The high throughput, high spectral resolution, and large spectral range of the SHRS were shown to not be limited by the size of the device, pointing the way to monolithic construction, the subject of this work. Several mSHRS devices were designed for Raman and LIBS spectroscopy. These fabricated for the group by a company that does custom optics. Most of the mSHRS spectrometers are compact, measuring about 3.5 x 2.5 x 2.5 cm in size and weigh about 80 g. The preliminary tests showed that the mSHRS has greatly improved the long-term stability and much improved the sensitivity over the original free-standing SHRS.

This work extends the mSHRS in three areas: remote LIBS, studies of a novel cross-dispersion mSHRS, and testing designs to further reduce the size of the mSHRS. The large field of view and large acceptance angle makes the spatial heterodyne spectrometer (SHS) spectrometer well suited for remote Raman and remote

LIBS measurements. The mSHRS was recently demonstrated for remote LIBS for samples at a 4.5-meter distance, using no collection optics other than the mSHS gratings. In other work, improvements in the signal to noise ratio (SNR) for weak bands in Raman spectra were demonstrated using the mSHRS in a novel cross-dispersion mode. Like any interferometer, noise in the mSHRS is equally distributed, meaning weak bands have the same noise as strong bands. This is an issue when weak bands are measured in a spectrum that has other strong bands. The SHS interferometer offers a potential solution to this problem by taking advantage of the 2-dimensional (2D) charge coupled device (CCD) detector, using the vertical dimension to produce a low-resolution separation of the spectral bands. This is accomplished by using a prism or diffraction grating to disperse the light in the vertical direction (cross-dispersion) onto the CCD. In other work, the area of the mSHRS footprint was decreased by a factor of ~4, and the volume was decreased by a factor of ~5. The smaller mSHRS devices measure 2.2 x 2.2 x 1.3 cm in size and weigh ~17 g yet have similar spectral resolution as the larger mSHRS devices. Together, the mSHRS improvements will enable their use in new applications, including sensors for exploration of the moons of the gaseous planets, such as Europa and Enceladus, comets, and asteroids, as well as near Earth exploration in extreme environments such as the chemical measurements around deep-ocean hydrothermal vents.

TABLE OF CONTENTS

LIST OF TABLES

LIST OF FIGURES

CHAPTER 1

INTRODUCTION

1.1 Planetary and Space Exploration

Venturing into space started October 4, 1957 with the launch of Sputnik 1, the first artificial satellite to orbit Earth.[1] Since the first launch there have been many missions and many discoveries have been made about the solar system. For example, NASA's Stratospheric Observatory for Infrared Astronomy (SOFIA) has confirmed that there is water on the sunlit surface of the Moon.[2] NASA spacecraft have also found signs of water in permanently shadowed craters on Mercury,[3] and recent volcanic activity on Venus.[4] Along with this, other scientific discoveries lead to evidence that the solar system contains a significant amount of water. Water is found in primitive bodies like comets and asteroids, and dwarf planets like Ceres. The four giant planets Jupiter, Saturn, Uranus and Neptune are thought to contain enormous quantities of water, and their moons and rings have substantial water ice.[5] NASA's Hubble Space Telescope provided powerful evidence that Ganymede (a moon of Jupiter) had a saltwater, sub-surface ocean, in between two layers of ice. Europa and Enceladus are thought to have an ocean of liquid water beneath their surface in contact with mineral-rich rock.[5] NASA's Cassini mission revealed that Enceladus had icy geysers and recent research suggested it may have hydrothermal activity on its ocean floor, an environment potentially suitable for living

organisms.[6] On Mars, NASA spacecraft have found clear evidence of water on its surface for long periods in the distant past. NASA's Curiosity Mars Rover discovered an ancient stream that existed amidst conditions favorable for life as we know it. NASA's Spitzer Space Telescope has observed signs of a hail of water-rich comets raining down on a young solar system, much like the bombardment planets in our solar system endured in their youth[7] and even on Pluto and the asteroid Ceres.[8,9] One discovery closer to home has been the presence of extremophiles, organisms found on Earth any place where there is liquid water under extreme conditions, including high temperature, high alkalinity or acidity, and even high radiation environments.[10] With these discoveries NASA's missions have been directed towards the search for extraterrestrial life.

While planetary science has grown tremendously in the past 60 years, there are still many questions left unanswered about our solar system. In the 2013 Planetary Decadal Survey, NASA released some questions and motivation for planetary science into three themes: building new worlds, planetary habitats, and workings of solar systems.[11] Each of which had its own set of questions. The first, was focused on understanding the origins of these solar systems and trying to answer what were the initial stages, conditions, and processes of the solar system formation and the nature of the interstellar matter that was incorporated. The second, was the search for life in planetary habitats, including finding the primordial sources of organic material of the planets. For example, Mars and Venus are believed to have ancient aqueous environments conducive to early life. The third involves, determining planetary processes through time through focuses on the workings of solar systems. This category of study looks at how studying the other planets and their atmospheres could help with

understanding Earth's atmosphere as well as how the chemical and physical processes that shaped the solar system have operated, interacted, and evolved over time.[11] These questions from the survey cannot be addressed by a single space mission and it cannot hint at one or more solar system bodies that may hold clues or other important information necessary for their resolution. Thus, it is vital to develop technology that facilitates our efforts to explore and research the space that surrounds planet Earth to continue and adapt as new technology becomes available.

1.2 Space Exploration

As mentioned previously, orbital space flight began in 1957 with the launch of the first artificial satellite, Sputnik I and then four years later the first human astronaut, Yuri Gagarin, made one orbit around earth in 1961.[1] In response, eight years following that, Neil Armstrong became the first human to set foot on the moon in 1969 through three NASA programs Mercury, Gemini, and Apollo.[12] However, since the 1970's, human space exploration has been limited to low Earth orbit missions that are both complex and costly due to the need for life support systems, food, water, waste management, radiation protection and return fuel. In order to explore beyond low Earth orbit unmanned probes and rovers have been sent into the solar system to gather information and aid in the determination of solar system locations for further investigation.[4] Therefore the next phase of space exploration began by sending spacecrafts to orbit to image many of the planets and large moons in the solar system. Both the U.S.S.R and U.S.A. launched a series of probes during the Cold War to study Venus and Mars, named the Venera and Mariner respectively.[13,14] In the 1970s, Pioneer 10 was launched to study Jupiter and provide images of the planet and its inner moons and became the first spacecraft to

escape the solar system.[15] Following the Pioneer launch, the twin spacecrafts Voyager 1 and 2 were launched in 1977.[16] Their primary mission was to conduct close studies of Jupiter and Saturn. They made several discoveries including the active volcanoes on Jupiter's moon Io and the intricacies of Saturn's rings. Voyager 2 then went on to explore Uranus and Neptune, and remains the only spacecraft to have visited those outer planets to date. In 2012 Voyager 1 later entered into interstellar space, the region between stars, and Voyager 2 joined its twin there six years later in 2018.[16] In 1989, the spacecraft Galileo was launched by NASA and reached Jupiter in 1995, becoming the first spacecraft to orbit an outer planet. It orbited Jupiter for almost eight years and found several key discoveries including that a global ocean of liquid water exists under the icy surface of Jupiter's moon Europa.[17] Currently the most advanced planetary satellite in orbit is the Mars Reconnaissance Orbiter (MRO) which has been studying the terrain of Mars since 2006. The MRO includes four imaging systems: the High Resolution Imaging Science Experiment (HiRISE) camera which can photograph Mars' surface; the Compact Reconnaissance Imaging Spectrometer for Mars (CRISM), a near infrared (IR) imaging spectrometer that can identify mineralogical surface features; the Mars Color Imager 4 (MARCI), a UV imager designed for climate tracking, and the Context Camera (CTX), a camera designed to provide wide swath pictures to provide spatial context for other MRO observations. In addition to these systems, the MRO has instruments for tracking the weather, vapor pressure, and dust variations of the Martian atmosphere, radar designed to detect underground layers of rock, ice, or water, and radio communication Doppler shift monitoring to study the gravitational fields of Mars.[18-21] Although spacecrafts have explored much of our solar system, there is still much more to be discovered, and while

the planetary satellites can provide considerable information, there is a limit to the amount and types of information that can be gathered from above a planet's surface. Therefore, it is necessary to use planetary landers to explore complex chemical processes or search for extraterrestrial life.

1.3 Exploring Planetary Surfaces

The U.S.S.R and the U.S.A. sent the Venera and the Pioneer landers respectively to Venus, with both sets of landers containing a payload of instruments including but not limited to seismic monitors, gas chromatographs, mass spectrometers, x-ray fluorescence spectrometers, UV, visible, and IR photometers and spectrometers, gamma-ray spectrometers, anemometers, and hygrometers.[13,22] NASA's Viking Project became the first U.S. mission to land a spacecraft safely on the surface of Mars and return images of the surface.[23] Viking 1 and 2 landers made it to Mars in 1976 and acquired photographs of the Martian soil as well as conducted three biology experiments to look for possible signs of life.[23] While these lander provided the most complete view of the planets surfaces, the decline of the Cold War caused a halt in exploration of planetary surfaces. There was a resurgence of surface exploration missions in the 1990s due to NASA's Sojourner, the first Mars rover. Sojourner was part of the Pathfinder mission, a project designed to demonstrate a low-cost method for delivering and implementing scientific instruments on Mars as the first wheeled vehicle to be used on another planet.[24] The rover landed on the planet using an air bag landing system and innovative petal design, which is still being used in various arrangements to land rovers on the surface of Mars. Originally Sojourner was meant to last 7 days but had an 83 day mission. Sojourner used a variety of cameras for imaging the surface and an alpha photon x-ray spectrometer

(APXS) for determination of composition of mineral samples.[24] Following Sojourner, in 2004 the twin rovers Spirit and Opportunity landed on opposite sides of Mars. Both rovers had a much larger scientific payload, including a microscopic imager (MI), a miniature thermal emission spectrometer (Mini – TES), a Mössbauer Spectrometer (MB), an APXS, a Rock Abrasion Tool (RAT), and an array of imaging cameras. While each rover only had a planned 90-day mission, they both lasted much longer than expected, with Spirit's mission ending in May 2011 after becoming permanently stuck in soft soil and with Opportunity's last communication coming in on June 10, 2018.[25-27] NASA's next mission to Mars was Curiosity, a 900 kg rover which landed on the surface of Mars in 2012. At 10 feet long, it was about twice as long and five times as heavy as the twin rovers. The size of Curiosity prevented it from taking advantage of the airbag-assisted landing. Instead, the Mars Science Laboratory used a guided entry and sky crane touchdown system to land the rover, which allowed for a gentle, high precision delivery. Thanks to Curiosity's size and new delivery system, its scientific payload was much larger and more complex than the previous rovers. Curiosity's payload includes a variety of cameras, an APXS, a remote Laser Induced Breakdown Spectrometer (LIBS) and remote Micro-Imager (RMI) known as ChemCam that can make measurements up to 7 meters away, a x-ray powder diffraction (XRD) spectrometer, x-ray fluorescence (XRF) spectrometer, quadrupole mass spectrometer, gas chromatograph, tunable laser spectrometer, and dynamic albedo of neutron instruments to detect hydrogen or liquid and solid water. To date Curiosity continues to operate and explore the Martian surface.[28] One of the latest missions to Mars is NASA's Perseverance rover which landed on the surface in early February 18, 2021, whose key objective for its mission on Mars

is astrobiology, including the search for signs of ancient microbial life.[29] Along with an impressive array of cameras, Perseverance also includes an upgrade to ChemCam, named SuperCam, which is capable of Raman spectroscopy, time resolved fluorescence (TRF) spectroscopy, visible and infrared (VISIR) reflectance spectroscopy, LIBS, and RMI, as well as other instruments such as a UV Raman spectrometer, a ground penetrating radar (GPR) system, and sensors for measuring temperature, humidity, radiation, dust, pressure, thermal IR, and wind speed and a sensitive microphone. There is also the Mars Oxygen In-Situ Resource Utilization Experiment (MOXIE), an instrument that will take carbon dioxide from the Martian atmosphere and convert it into oxygen.[29] After Perseverance landed in the Jezero Crater on Mars, it spent more than a year studying outcrops, boulders, and regolith (broken rock and dust) in the area, gathering samples along the way. This led to the discovery of the origin of igneous rocks that formed billions of years ago from molten rock that cooled either underground or after volcanic eruptions.[30] The team also found evidence that the igneous rocks interacted with water and could have once hosted habitable microenvironments, and the sedimentary rocks that dominate the Jezero delta provide an ideal site to look for signs of past life. However, confirmation of this will be made after the samples that Perseverance is currently gathering are brought to Earth and analyzed with powerful lab equipment that is too large to bring to Mars. Subsequent NASA missions, in cooperation with ESA (European Space Agency), will send spacecraft to Mars to collect these sealed samples.[30]

Finally, Perseverance carried an experimental helicopter named Ingenuity which tested the first flight on Mars. Ingenuity weighed about 2 kg and had counter rotating blades designed to spin very fast in the thin Mar's atmosphere at about 2400 rpm, much

faster than a helicopter would spin on earth. Having cameras in the air in future Mars missions would provide scientists a new perspective on a region's geology and allow them access to areas too slippery or steep to navigate using a rover.[31] Once Ingenuity was release it performed a series of test flights over a 30 Martian day period. The helicopter completed its technology demonstration after three successful flights which was a major milestone as the first powered controlled flight in the Martian atmosphere. Afterwards the helicopter successfully performed additional experimental flights and will transition to an operations demonstration phase to show how future rovers and aerial explorers can work together.[31] Overall, Perseverance played host to several highly prescience scientific instruments, many of which had never been used on another planet's surface before, which has led to important discoveries about the planet and possibly information about the existence of early life on Mars. The rover will characterize the planet's geology and past climate, pave the way for human exploration of the Red Planet, and be the first mission to collect and cache Martian rock and regolith.

1.4 Optical Spectrometers

Optical spectroscopy is starting to become more widely used in planetary exploration NASA has implemented optical spectrometers on missions to Mars which include the ChemCam and SuperCam instruments on the Curiosity and Perseverance rovers respectively. With optical spectroscopy, elemental and/or structural chemical information about a given sample or even mapping the locations of chemical components in a sample via imaging can be obtained, thus making it a particularly useful technique for planetary exploration. There are many different types of spectroscopies with attributes that can include, being fast, nondestructive, performed with no sample contact or no sample

preparation, small or requiring low power. The ChemCam is a remote LIBS spectrometer that can make measurements at up to 7 m away from the rover with a full 360° view. By ablating a small sample spot size ChemCam can rapidly identify the rocks being studied, determine the composition of soils and pebbles, measure the abundance of all chemical elements, including trace elements and those that might be hazardous to humans, recognize ice and minerals with water molecules in their crystal structures, measure the depth and composition of weathering rinds on rocks, and provide visual assistance during drilling of rock cores.[32] The SuperCam on the Perseverance rover examines rocks and soils with a camera like the LIBS spectrometer on ChemCam laser and that seeks spectrometers to seek organic compounds that could be related to past life on Mars.[33] Raman is a vibrational spectroscopy technique that is nondestructive and capable of providing a molecular fingerprint of solid, liquid, and gaseous samples without any sample preparation.[34] This technique is fast and can be used to identify minerals, water, ice, and organic molecules that may be indicative of past or present life.[35,36] SuperCam can be used to perform Raman measurements using a 532 nm pulsed laser for samples up to 12 m away from the rover, and provide information about the mineralogy and molecular structure of the samples.[37] Perseverance also has one other Raman spectrometer, the Scanning Habitable Environments with Raman and Luminescence for Organics and Chemicals (SHERLOC), which is a deep UV resonance Raman spectrometer capable of highly sensitivity detection and useful for characterization of organics and minerals in the Martian surface and near subsurface. While SHERLOC does not have the same remote capabilities as SuperCam's Raman spectrometer, it can provide an image of a 7 x 7 mm area that will allow scientists to assess past aqueous history,

detect the presence and preservation of potential biosignatures, and select samples for return to Earth.[38]

1.5 The monolithic Spatial Heterodyne Spectrometer

This thesis focuses on the development of a new type of miniature spectrometer, the monolithic spatial heterodyne spectrometer (mSHRS), an instrument that would be suitable for future planetary missions. The mSHRS is a fixed grating interferometer that has many features that are beneficial for space applications: large spectral range, high resolution, wide acceptance angle, and high throughput that can be obtained with an instrument size much smaller than conventional Raman spectrometers.[39] Additionally, since the mSHRS has all of the optical components bounded together with UV curable epoxy it is a small and stable spectrometer with optical components in one piece. The mSHRS has a large entrance aperture and a wide acceptance angle, which when combined, allow for large areas of the sample to be viewed simultaneously with a large field of view (FOV). The ability to view large areas of the sample simultaneously has proven to be useful for one shot 1D and 2D hyperspectral Raman imaging [40,41] and can be used to reduce laser-induced photodegradation of the sample by allowing a large laser spot size for sample excitation. This has been shown to be useful for deep-UV Raman measurements, where the Raman cross section is greatly increased but where sample photodegradation caused by the use of a tightly focused laser, can greatly reduce the observed intensity which eliminates photodegradation.[42] The many qualities of the mSHRS that make it suitable for planetary exploration will be discussed in later chapters.

1.6 Thesis Outline

Chapter 2 will describe the theoretical background of Spatial Heterodyne Spectroscopy along with a further explanation of Raman spectroscopy and underlying theory, a combination of the general SHS with Raman spectroscopy to form the SHRS, an and explanation of Laser induced breakdown spectroscopy in tandem with the SHLS.

Chapter 3 describes the wide field of view of the mSHLS by measuring standard copper LIBS samples at a distance of 4.5 meters. Successful recovery of spectra with LIBS plasma deviating from the optical axis of the spectrometer by ~ 0.6^{o} was obtained and the addition of a small telescope for light collection increased the amount of signal light collected by an order of magnitude, even while accumulating 500 fewer laser shots per spectrum.

Chapter 4 describes the use of a transmission grating paired with a monolithic SHRS (x_gmSHRS), to demonstrate that the crossed-dispersed method facilitates the measurement of weak Raman spectral features in various Raman reference samples that, in a traditional mSHRS, would be overpowered by multiplicative photon noise. The x_gmSHRS showed overall improvement in SNR compared to the traditional mSHRS.

Chapter 5 describes initial tests of a further miniaturized mSHRS (half-inch mSHRS). The half-inch mSHS is about 2.2 x 2.2 x 1.3 cm in size and weigh about 17 g, and is constructed in a 1D configuration. The spectral resolution of the 1D mSHRS is shown to be about of 8 - 10 cm^{-1}.

Lastly, Chapter 6 describes preliminary tests of high-pressure LIBS. A pressure cell was custom made to mimic deep ocean hydrothermal vents environments and a pulse

ND:YAG laser operating at 532 nm was focused into the pressure to create the LIBS plasma. Data was collected using grating spectrometer paired with an intensified charged coupled device (ICCD). 1 ppm lithium-ion concentration of 1 ppm is shown to have higher signal detection was lower laser powers (3- 40 mJ).

1.7 References

1. Wilkinson, Freddie. "The History of Space Exploration." *The History of Space Exploration | National Geographic Society*, National Geographic, 6 Feb. 2022, education.nationalgeographic.org/resource/history-space-exploration.
2. Potter, Sean. "NASA's SOFIA Discovers Water on Sunlit Surface of Moon." *NASA*, 4 Jan. 2021, www.nasa.gov/press-release/nasa-s-sofia-discovers-water-on-sunlit-surface-of-moon.
3. "Water Ice on Mercury." *NASA*, 7 Aug. 2017, www.nasa.gov/image-feature/water-ice-on-mercury.
4. "NASA - NASA-Funded Research Suggests Venus Is Geologically Alive." *NASA*, 4 Aug. 2010, www.nasa.gov/topics/solarsystem/features/magellan20100408.html#:%7E:text=The%20observations%20reveal%20that%20volcanoes,the%20last%203%20million%20years.
5. "The Solar System and Beyond Is Awash in Water." *NASA*, 7 Apr. 2015, www.nasa.gov/jpl/the-solar-system-and-beyond-is-awash-in-water.
6. "Enceladus | Science –." *NASA Solar System Exploration*, solarsystem.nasa.gov/missions/cassini/science/enceladus/#:%7E:text=Cassini%20re

vealed%20the%20dramatic%20truth,from%20this%20fascinating%20ocean%20world. Accessed 07 July 2022.

7. "NASA Confirms Evidence That Liquid Water Flows on Today's Mars." *NASA*, 15 Sept. 2015, www.nasa.gov/press-release/nasa-confirms-evidence-that-liquid-water-flows-on-today-s-mars.
8. Tavares, Frank. "Pluto's Ice Caps Made of Methane, Turns Earth's Process Upside Down." *NASA*, 2 Mar. 2021, www.nasa.gov/feature/ames/pluto-ice-caps.
9. "Where Is the Ice on Ceres? New NASA Dawn Findings." *NASA*, 15 Dec. 2015, www.nasa.gov/feature/jpl/where-is-the-ice-on-ceres-new-nasa-dawn-findings.
10. Gabriel, São. "NCBI - WWW Error Blocked Diagnostic." *National Library of Medicine*, 7 Aug. 2013, www.ncbi.nlm.nih.gov/pmc/articles/PMC4187170.
11. "Vision and Voyages for Planetary Science in the Decade 2013–2022." *NASA Solar System Exploration*, 7 Mar. 2011, solarsystem.nasa.gov/resources/598/vision-and-voyages-for-planetary-science-in-the-decade-2013-2022.
12. "NASA: 60 Years and Counting - Human Spaceflight." *NASA*, www.nasa.gov/specials/60counting/spaceflight.html. Accessed 07 July 2022.
13. "Venera Missions to Venus." *NASA*, nssdc.gsfc.nasa.gov/planetary/venera.html. Accessed 07 July 2022.
14. Williams, David. "The Mariner Missions." *NASA*, nssdc.gsfc.nasa.gov/planetary/mars/mariner.html. Accessed 07 July 2022.
15. "In Depth | Pioneer 10 –." *NASA Solar System Exploration*, solarsystem.nasa.gov/missions/pioneer-10/in-depth. Accessed 07 July 2022.

16. “Voyager - Planetary Voyage.” *NASA*, voyager.jpl.nasa.gov/mission/science/planetary-voyage. Accessed 07 July 2022.
17. NASA. “Galileo” https://solarsystem.nasa.gov/missions/galileo/overview/ Accessed 07 July 2022.
18. M.C. Malin et al. “Context Camera Investigation on board the Mars Reconnaissance Orbiter”. J. Geophys. Res. 2007. 112(E5): E05S04
19. A.S. McEwen et al. “Mars Reconnaissance Orbiter’s High Resolution Imaging Science Experiment (HiRISE)”. J. Geophys. Res. 2007. 112(E5): E05S02.
20. S. Murchie et al. “Compact reconnaissance Imaging Spectrometer for Mars (CRISM) on Mars Reconnaissance Orbiter (MRO)”. J. Geophys. Res. 2007. 112(E5): E05S03.
21. NASA. “Mars Reconnaissance Orbiter - Mars Missions - NASA Jet Propulsion Laboratory”. www.jpl.nasa.gov/missions/mars-reconnaissance-orbiter-mro/ Accessed 08 July 2022.
22. “Venus Exploration Timeline.” *NASA*, nssdc.gsfc.nasa.gov/planetary/chronology_venus.html. Accessed 09 July 2022.
23. Mars.Nasa.Gov. “Viking 1 and 2.” *NASA Mars Exploration*, mars.nasa.gov/mars-exploration/missions/viking-1-2. Accessed 08 July 2022.
24. “Mars Pathfinder - Mars Missions - NASA Jet Propulsion Laboratory.” *NASA Jet Propulsion Laboratory (JPL)*, www.jpl.nasa.gov/missions/mars-pathfinder-sojourner-rover. Accessed 08 July 2022.

25. NASA Jet Propulsion Laboratory. “Mars Exploration Rover – Spirit”. https://www.jpl.nasa.gov/missions/mars-exploration-rover-spirit-mer-spirit/ Accessed 08 July 2022.
26. NASA. “Spirit”. https://solarsystem.nasa.gov/missions/spirit/in-depth/ Accessed 08 July 2022.
27. NASA Jet Propulsion Laboratory. “Mars Exploration Rover – Opportunity”. https://www.jpl.nasa.gov/missions/mars-exploration-rover-opportunity-mer/ Accessed 08 July 2022.
28. NASA Jet Propulsion Laboratory. “Mars Exploration Rover - Curiosity”. https://www.jpl.nasa.gov/missions/mars-science-laboratory-curiosity-rover-msl/ Accessed 08 July 2022.
29. “Mars 2020 Perseverance Rover.” *NASA Mars*, mars.nasa.gov/mars2020. Accessed 09 July 2022.
30. M. Baker. “Searching for Sand Transport.” *NASA Mars*, 7 July 2022, mars.nasa.gov/mars2020/mission/status/389/searching-for-sand-transport.
31. Mars.Nasa.Gov. “Mars Helicopter.” *NASA Mars*, mars.nasa.gov/technology/helicopter/#Overview. Accessed 09 July 2022.
32. Mars.Nasa.Gov. “ChemCam.” *NASA Mars Exploration*, mars.nasa.gov/msl/spacecraft/instruments/chemcam. Accessed 09 July 2022.
33. “SuperCam.” *NASA Mars*, mars.nasa.gov/mars2020/spacecraft/instruments/supercam. Accessed 09 July 2022.
34. R.L. McCreey, “Raman Spectroscopy for Chemical Analysis”. John Wiley & Sons, New York. 2000.

35. S.K. Sharma, P.G. Lucey, M.G. Hugh, W.H. Keith A. Horton, “Stand-off Raman spectroscopic detection of minerals on planetary surfaces”. Spectrochimica Acta Part A 2003. (59): 2391-2407.

36. S.M. Angel, S.K. Sharma, N.R. Gomer, C. McKay, “Remote Raman Spectroscopy for Planetary Exploration: A Review”. Applied Spectroscopy. 2012. 66(2): 137-150.

37. W.M. Sylvestre, F.R. Perez, SuperCam Team, “The SuperCam Remote Instrument Suite for Mars 2020 Rover”. Los Alamos National Laboratory. 2017

38. “Scanning Habitable Environments with Raman and Luminescence for Organics & Chemicals (SHERLOC).” *NASA Mars*, mars.nasa.gov/mars2020/spacecraft/instruments/sherloc. Accessed 09 July 2022.

39. A. Waldron, A. Allen, A. Colón, J. Chance Carter, S. Michael Angel. “A Monolithic Spatial Heterodyne Raman Spectrometer: Initial Tests”. Applied Spectroscopy. 2021. 75(1): 57-69.

40. A.K. Strange Fessler, A. Waldron, A. Colón, J.C. Carter, S.M. Angel, “A demonstration of spatial heterodyne spectrometers for remote LIBS, Raman spectroscopy, and 1D imaging” Spectrochimica Acta Part B. 2021. 178.

41. A. Allen, A. Waldron, J.M. Ottaway, C.J. Carter, S.M. Angel, “Hyperspectral Raman Imaging Using a Spatial Heterodyne Raman Spectrometer with a Microlens Array”. Applied Spectroscopy. 2020. Vol. 74(8): 921-931.

42. N. Lamsal, S.M. Angel. ‘‘Deep-Ultraviolet Raman Measurements Using a Spatial Heterodyne Raman Spectrometer (SHRS)’’. Applied Spectroscopy. 2015. 69(5): 525–534.

CHAPTER 2

THEORETICAL BACKGROUND

2.1 Introduction of the Spatial Heterodyne Spectrometer (SHS)

The spatial heterodyne spectrometer (SHS) was first developed by Dohi et al. in 1970,[1] and later adapted by Harlander et al. in 1991 for emission studies.[2] The many features of the SHS makes it suitable for a variety of spectroscopic applications. For example, it has a compact size, large spectral range using a relatively small number of detector elements, high spectral resolution, and high light throughput in comparison to dispersive spectrometers of comparable size.[3,4] Conventional dispersive spectrometers generate spectra by optically separating incoming signal into its spectral components and require long focal length optics and very narrow slits to achieve high resolution. This decreases light throughput and increases the footprint of the instrument. Unlike conventional grating spectrometers these requirements are not needed for the SHS which ultimately can lead to further minimizing its instrument footprint.[5,6]

Fourier transform spectrometers (FTS), such as the Michelson interferometer, have a Fellgett or multiplex advantage where the signal-to-noise ratio is equal to the square root of the number of resolution elements being scanned.[7] Multiplexing is attributed to the observation system as a whole.[8] For example, in the case of using a

detection system like a charged coupled device (CCD), the multiplex advantage can be achieved but obtaining spectra in one shot. Conversely, the use of a scanning wave

analyzer would eliminate the multiplex advantage.[8,9] While the SHS does not share the full multiplex advantage, it does gain a partial multiplex advantage over dispersive systems due to the photon flux at each detector element being greater than those experienced by the dispersive system, as a result of the high light throughput of the SHS.[10] Since interferometers do not need a slit to achieve high spectral resolution the etendue of these systems are much larger than dispersive spectrometers, generally 200 times greater.[2] Similarly, the SHS also has this advantage and can achieve sensitivities up to two orders of magnitude greater than those of conventional dispersive spectrometers for instances in which spectral quality would be degraded when using a grating spectrometer like extended sources.[3,10]

Another advantage that the SHS has over dispersive systems like grating spectrometers is its wide acceptance angle. In the basic design of the SHS the acceptance angle is ~1° which can be further increased up to 10° with the use of field-widening prisms, placed between the beam splitter and the gratings.[2,4] Using the SHS, an entire spectrum can be collected simultaneously with no moving parts because the SHS is non-scanning, which helps avoid certain types of noise that would be typically observed in FTS systems. For example, scintillation noise which is caused by variations in the source intensity can introduce artifacts and distort the FTS spectrum.[11] Overall, the advantages of the SHS include its relatively small footprint (compared to a conventional spectrometer of similar spectral resolution) and the ability to be built monolithically, making it extremely robust, easy to align, and deployable. Thus, monolithic construction

produces a spectrometer that is immune to the effects of external vibrations and shocks, which is a common issue with interferometers.[12]

2.2 Theory

The SHS is a fixed-grating heterodyne interferometer that is like a Michelson interferometer but with tilted diffraction gratings and no moving parts as shown in Figure 2.1.[3,4] A sample (S) is excited by a monochromatic light source to produce a signal that is collimated and directed into the SHS by a lens (L_1) The collimated signal entering the SHS is split into two beams by the beam splitter (BS). The beams strike the tilted diffraction gratings (G_1 and G_2) and are diffracted back along the same direction. As the beams re-enter the beam splitter, they recombine to produce a crossing wavefront (CW) which is then imaged onto a CCD detector (D) with a camera lens (L_2). The image produces a wavelength dependent fringe image (FI) from which a spectrum is extracted using a fast fourier transform (FFT) method. The grating tilt angle defines the Littrow wavenumber (λ_L), the wavenumber at which both beams exactly retro-reflect and produce no fringe pattern at the detector.[4] For any wavelength other than Littrow, the recombined light produces a crossed wave front, of which the crossing angle is wavenumber dependent and produces an interference pattern at the interferometer output. The interference pattern recorded by the CCD is an image of vertical fringes with intensity as a function of detector position as shown in Eq.2.1:

$$I(x) = \int_0^\infty B(\sigma)[1+\cos\{8\pi(\sigma-\sigma_L)x\tan\theta_L\}]d\sigma \qquad \text{Eq. 2.1}$$

Where $I(x)$ is the intensity distribution of the fringe pattern as a function of the detector position, $B(\sigma)$ is the input spectral intensity at wavenumber σ, σ_L is the Littrow

wavenumber, and θ_L is the Littrow angle. The number of fringes (i.e., spatial frequency), *f*, across the CCD is related to the Littrow wavenumber by Eq. 2.2:

$$f = 4(\sigma-\sigma_L)tan\theta_L \quad \text{Eq. 2.2}$$

Where *f* is in fringes/cm and σ wavenumber of interest. The resolving power, *R*, is determined by the total number of grooves illuminated on the two gratings shown in Figure 4.1. Eq. 2.3:

$$R= 2Wd \quad \text{Eq. 2.3}$$

Where W is the width of the grating and d is the grating density (grooves/mm). The theoretical maximum bandpass of the SHRS is determined by the resolving power, *R*, and the number of pixels, *N*, in the horizontal direction on the detector. The Nyquist limit sets the highest fringe frequency that can be measured by the detector to the frequency that produces N/2 fringes.[3-6,13,14] The theoretical bandpass, BP, can be calculated using Eq. 2.4:

$$BP = N\lambda/2R \quad \text{Eq. 2.4}$$

Where *N* is the number of pixels in the horizontal direction, λ is the Littrow wavelength, and *R* is the resolving power. The collection solid angle of the SHS is the same as conventional FTS systems with a full acceptance angle equal to $\sqrt{\Omega}$, which is ~1º for a typical SHRS.[3] The equation for the collection solid angle is shown in Eq. 2.5:

$$\Omega = 2\pi/R \quad \text{Eq. 2.5}$$

This design allows for miniaturization of the SHRS because the spectral resolution is not strongly dependent on the size of the device or a slit size as with conventional dispersive

spectrometers. Compared to conventional spectrometers, the optical throughput, or optical etendue determines the maximum spectral sensitivity for a given laser power. The optical Etendue of the SHS is several orders of magnitude higher than conventional slit based spectrometers of the same resolving power. The amount of light that can be collected by an optical system, the optical etendue, is shown in Eq. 2.6:

$$E = \Omega A \qquad \text{Eq. 2.6}$$

Where Ω (in sr) is the collection solid angle of the system and A (in cm^2) is the area viewed. The large entrance aperture of the SHS allows for very large diameter fibers to be used. The area measured by the fiber probe is proportional to the collection fiber diameter. The sampling distance from the probe tip is directly proportional to the collection fiber diameter and the sampling volume is proportional to the cube of the fiber diameter.[15,16] This is especially significant for measuring solids or opaque samples because it makes it easier to maintain the proper working distance from the probe to sample and it minimizes changes in measured intensity for small changes in the probe to sample distance.

Spectral bands with larger wavenumber shifts produce higher frequency fringes and because of the symmetry in Eq. 2.2, the spatial fringe frequency is identical for $+\sigma$ and $-\sigma$. These spectral features at wavenumbers both above and below Littrow overlap on the detector and cause band fold over which can lead to ambiguity in determining the wavenumber of spectral features. While a bandpass filter can be added to the optical system to block a spectral region, the preferred method for extracting wavelengths above and below Littrow simultaneously and with no overlapping features first involves introducing a slight vertical tilt one grating to avoid the degeneracy described by eq. 2.1

and 2.2. Thus, results in a rotation of the fringe pattern clockwise for bands below Littrow and counterclockwise for bands above Littrow.[4] The vertical tilt introduces a spatial phase shift along the axis orthogonal to the dispersion plane of the diffraction gratings, (i.e., the y-axis), resulting in a new intensity function at the detector as shown in eq. 2.7.[5]

$$I(x,y) = \int_0^{\infty} B(\sigma)[1+\cos\{2\pi*4\tan\theta_L\,(\sigma-\sigma_L)x + 2\alpha\sigma y\}]d\sigma \qquad \text{Eq.2.7}$$

Where σ is the angle of the vertical diffraction grating tilt resulting in an additional term which corresponds to the spatial frequency in the y-axis of the detector. In this case the frequency term in the y-axis is not heterodyne and it does not correspond to the fringes distributed in the x-axis of the detector. In this design, the Fizeau fringes that correspond to wavenumbers higher than Littrow are rotated in one direction while the Fizeau fringes corresponding to wavenumbers lower than Littrow are rotated in the opposite direction to produce a cross-hatched interference pattern.[4,5] By applying a two-dimensional Fourier transform to the cross-hatched interference pattern, spectral features above and below Littrow may be recovered without any ambiguity and this technique can also be used to double the spectral range of the SHS without increasing the number of CCD pixels used.[5]

2.3 Raman Spectroscopy

Raman spectroscopy is an inelastic scattering technique first observed by C.V. Raman in 1928. This technique requires little to no sample preparation with essentially no spectral pressure effect for most chemical species. Raman spectra can be used to identify organic and inorganic chemical compounds and minerals based on the vibrational frequencies, relative intensities, and the overall molecular ‘fingerprint’ provided by

spectra. As with many optical spectroscopy techniques, Raman has also been demonstrated for remote measurements where the sample can be tens of meters away from the spectrometer.[17,18] Since water is a relatively weak Raman scatterer, there would be little interference with under water measurements.

Raman spectroscopy requires a change in polarizability.[19] The polarization and scattering intensities are linear with the laser intensity with light being scattered at three different frequencies.[19] This as illustrated in Figure 2.2 The first term is Rayleigh scattering, which is the same frequency as the laser. The second and third terms are anti-Stokes Raman scattering and Stokes Raman scattering, respectively. Only a very small fraction of light is Raman scattered due to its small cross section which is proportional to the probability of an incident photon being scattered (1 in 10 million).[19] For this reason, the widespread adoption of Raman spectroscopy was initially very limited until the advent of the laser as an excitation source combined with other instrumentation technologies. Eq. 2.8 shows the theoretical Raman signal that can be detected in terms of instrumental variables comprising the collection function.

$$S = (P\beta DK)(A\Omega TQ) \qquad \text{Eq.2.8}$$

where S is Raman signal (photoelectrons pulse^{-1}), P is laser power (photons pulse^{-1}cm^{-2}), β is the Raman cross-section for a particular Raman band of a particular sample (cm^{2}molcule^{-1}sr^{-1}), D is number density of the sample (molecule cm^{-3}), K is sample path length (cm), A is area view by the collection optics and spectrometer (cm^2), Ω is collection solid angle of the collection optics and spectrometer (sr), T is transmission of the optics (unitless) and Q is the quantum efficiency of the detector (e^{-1}photon^{-1}). The laser and sample function relate to the variables in the first set of parentheses and the

collections optics and detector function relate to the variables in the second set of parentheses. Technological advancements in recent decades have advanced Raman to a very mature state with many commercial products offered to address a wide application space. Specific advances include the development of the charge-coupled device (CCD) detectors, monochromatic laser sources, and optical filters. The latter is very important since the elastic Rayleigh scattered light must be rejected using a narrow band notch filter to enable collecting Raman signal from sample. The laser source used can be focused to a spot on the sample, providing high spatial resolution.

A Raman system consists of a spectrometer or interferometer for sorting wavelengths, an excitation laser source, and a detector (usually a cooled charge coupled device detector). The ideal Raman spectrometer depends on the application. For measurements in extreme environments such as planetary and deep ocean exploration, the overall size, weight, and power (SWaP) requirements of the spectrometer subsystem and its ability to discriminate sample signals from mixtures and complex matrices are critically important. In such applications, the spectrometer should have high spectral resolution, large spectral range, high light throughput, and be small and lightweight for operating outside of the pristine laboratory. Additionally, the Raman spectrometer should be compatible with near infrared, visible, UV, or deep UV laser excitation. The SHRS meets all the aforementioned requirements and is compatible with any wavelength Raman.[3]

2.4 Laser Induced Breakdown Spectroscopy (LIBS)

Laser-induced breakdown spectroscopy (LIBS) was first reported by Brech and Cross in 1962.[20] LIBS, also sometimes called laser-induced plasma spectroscopy (LIPS) or laser spark spectroscopy (LSS)[21], is a spectroscopic technique that allows rapid multi-

elemental analysis of solids, liquids, and gases with little to no sample preparation. LIBS is well suited for in situ, non-contact, and remote elemental analysis. This technique uses a low-energy pulsed laser which is focused onto a sample using a lens to produce a plasma that heats, ablates, and ionizes a small amount of the sample. Soon after ablation, the plasma starts to decay within microseconds, and the excited atoms and ions relax down to a ground energy level. As the plasma decays an emission of continuum and ionic spectra are observed[21] using very similar instrumentation as required for pulsed Raman measurements. These processes are followed by spectra from neutral atoms, and eventually simple molecules formed from the recombination of atoms.[20-26] The continuum spectra are observed due to bremsstrahlung (free–free) and recombination (free–bound) events. In the bremsstrahlung process, photons are emitted by electrons accelerated or decelerated in collisions. Recombination occurs when a free electron is captured into an ionic or atomic energy level and gives up its excess kinetic energy in the form of a photon. An energy level diagram of these processes is shown in Figure 2.4. The emission spectra produce specific characteristics per sample like a fingerprint which allows the determination of the atomic composition of the sample.

LIBS is one of the few analytical techniques which can measure many chemical elements simultaneously. LIBS and Raman spectroscopy can be conducted is conjunction;[27-39] and, the very similar requirements for a Raman spectrometer operating in extreme environments follow for a LIBS spectrometer in extreme environments. High spectral resolution, large spectral range, high light throughput, and be small and lightweight for analyses outside of the laboratory are all necessary characteristics for LIBS as with Raman. Thus, SHS technologies are ideally suitable for both.

2.5 Monolithic SHRS and SHLS (mSHRS and mSHLS)

One of the advantages of the SHS solid state design is that it can be built monolithically. The SHS monoliths are made of fused silica components with two 15 mm gratings and a beam splitter that is approximately 25 x 25 mm as shown in Figure 2.3. mSHRS measurements have been demonstrated using a cooled complementary metal oxide semiconductor (CMOS) detector which offered similar SNR to that of a cooled CCD. Results using both 1D and 2D SHS configurations included wide spectral range, high resolution data comparable to an industrial microRaman spectrometer, remote Raman and LIBS measurement, 1D imaging, and cross dispersive mSHRS.[12,40] Overall, the mSHRS offers many advantages over the conventional dispersive Raman systems. These advantages include 10 to 100 times larger acceptance angle, 10^2 to 10^4 higher light throughput, very high spectral resolution, a wide spectral range, and its robustness.[6,7]

2.6 References

1. T. Dohi, T. Suzuki. “Attainment of High Resolution Holographic Fourier Transform Spectroscopy”. Applied Optics. 1971. 10(5): 1137 – 1140.
2. J. M. Harlander. Spatial Heterodyne Spectroscopy: Interferometric Performance at Any Wavelength without Scanning. [Ph.D. Dissertation]. Madison, WI: University of Wisconsin-Madison, 1991.
3. N. Lamsal, S.M. Angel, “Performance Assessment of a Plate Beam Splitter for Deep-UV Raman Measurements with a Spatial Heterodyne Raman Spectrometer”. Applied Spectroscopy. 2017. 71(6): 1263-1270.

4. N. R. Gomer, C.M Gordon, P. Lucey, S.K. Sharma, J.C. Carter, S.M. Angel, “Raman Spectroscopy Using a Spatial Heterodyne Spectrometer: Proof of Concept”. Applied Spectroscopy. 2011. (65): 849-857.
5. J. M. Harlander, F. L. Roesler, C.R. Englert, J. G. Cardon, R. R. Conway, C. M. Brown, J. Wimperis. “Robust Monolithic Ultraviolet Interferometer for the SHIMMER Instrument on STPSat-1”. Applied Optics 2003. 42(15): 2829-2834.
6. P.D. Barnett, S. M. Angel, “Miniature Spatial Heterodyne Raman Spectrometer with a Cell Phone Camera Detector”. Applied Spectrscopy. 2016. 71(5): 988-995.
7. W.D. Perkins “Fourier Transform Infrared Spectroscopy”. Topics in chemical instrumentation. 1987. 64(11): A269-A271.
8. P. Fellgett, “Conclusions on Multiplex Methods”. Journal de Physique Colloques. 1967. 28(C2): 165-171.
9. J.T McWhirter, A.J. Sievers, “Time-Resolved Spectroscopy with Fourier Transform Spectrometers: Maintaining the Felllgett Advantage”. Applied Spectroscopy. 1991. 45(9): 1391-1394.
10. D. Dewey, “Extended source analysis for Grating Spectrometers”. MSSL. 2002. 1-6.
11. J. M. Harlander, F. L. Roesler. “Spatial Heterodyne Spectroscopy: A Novel Interferometric Technique for Ground-Based and Space Astronomy”. Proc. SPIE. 1990. 1235: 622-633.
12. A. Waldron, A. Allen, A. Colón, J. Chance Carter, S. Michael Angel. “A Monolithic Spatial Heterodyne Raman Spectrometer: Initial Tests”. Applied Spectroscopy. 2021. 75(1): 57-69.

13. N. Lamsal, S. M. Angel, “Deep-UV Raman Measurements Using Spatial Heterodyne Raman Spectrometer (SHRS)”. Applied Spectroscopy. 2015. 69(5): 525-234.
14. P.D. Barnett, N. Lamsal, S. M. Angel, “Standoff LIBS using a Miniature Wide Field of View Spatial Heterodyne Spectrometer with Sub-Microsteradian Collection Optics”. Applied Spectroscopy. 2017. 71(4): 583-590.
15. T.F. Cooney, T. F., Skinner, H. T., Angel, S. M., “Comparative Study of some Fiber-Optic Remote Raman Probe Designs. Part I: Model for Liquids and Transparent Solids”. Applied Spectrscopy. 1996. 50(7): 836-848.
16. T.F. Cooney, H.T. Skinner, S.M. Angel, “Comparative Study of some Fiber-Optic Remote Raman Probe Designs. Part II: Tests of Single-Fiber, Lensed, and Flat- and Bevel-Tip Multi-Fiber Probes”. Applied Spectroscopy. 1996. 50(7): 849-860.
17. J.P. Urmos, S.K Sharma, F.T. Mackenzie, “Characterization of some biogenic carbonates with Raman Spectroscopy”. American Mineralogist. 1991. 76: 642-646.
18. A. Wang, J. Han, L. Guo, J. Yu, P. Zeng, “Database of standard Raman-spectra of minerals and related inorganic crystals”. Applied Spectroscopy. 1994. 48: 959-968.
19. R.L. McCreey, “Raman Spectroscopy for Chemical Analysis”. John Wiley & Sons, New York. 2000.
20. F. Brech, L. Cross, “Optical microemission stimulated by a ruby laser” Applied Spectroscopy. 1962. 16: 59.
21. D.A. Cremers, L.J. Radziemski, “Handbook of Laser-Induced Breakdown Spectroscopy”. John Wiley & Sons. 2013.

22. A. Ciucci, M. Corsi, V. Palleschi, S. Ratelli, A. Salvetti, E. Tognoni, “New procedure for quantitative elemental analysis by laser-induced plasma spectroscopy”. Applied Spectroscopy. 1999. 53: 960–964.
23. D.A. Cremers, “The analysis of metals at a distance using laser-induced breakdown spectroscopy”. Applied Spectroscopy. 1987. 41: 572–578.
24. T.R. Loree, L.J. Radziemski, “Laser-induced breakdown spectroscopy: time integrated applications”. Plasma Chemistry and Plasma Processing. 1981. 1:271-280.
25. J.F. Ready, “Effects of High-Power Laser Radiation”. New York: Academic Press. 1971.
26. W.W. Schroeder, J.J. van Niekirk, L. Dicks, A. Strasheim, H.v.d Piepen, “A new electronic time resolution system for direct reading spectrometers and some applications in the diagnosis of spark and laser radiations”. Spectrochimica Acta Part B. 1971. 26: 331–340.
27. S.K. Sharma, A.K. Misra, P.G. Lucey, R.C.F. Lentz, “A combined remote Raman and LIBS instrument for characterizing minerals with 532nm laser excitation”. Spectrochimica Acta Part B. 2009. 73: 468–476.
28. K. M. Muhammed Shameem, V. S. Dhanada, V. K. Unnikrishnan, et al., “A hyphenated echelle LIBS-Raman system for multi-purpose applications”. Review of Scientific Instruments. 2018. 89: 073108.
29. S. Choi, J. Choi, J.J. Yoh, “Advancing the experimental design for simultaneous acquisition of laser induced plasma and Raman signals using a single pulse”. Spectrochimica Acta Part B. 2016. 123:1–5.

30. Q. Lin, G. Niu, Q. Wang, Q. Yu, Y. Duan, “Combined Laser-Induced Breakdown with Raman Spectroscopy: Historical Technology Development and Recent Applications” Applied Spectroscopy Reviews. 2013. 48:487–508.
31. S.K. Sharma, A.K. Misra, P.G. Lucey, R.C. Wiens, S.M. Clegg, “Combined remote LIBS and Raman spectroscopy at 8.6m of sulfur-containing minerals, and minerals coated with hematite or covered with basaltic dust”. Spectrochimica Acta Part A. 2007. 68: 1036–1045.
32. J. Yang, H. M. Jun, J.J. Yoh, “Double-pulse laser synchronization aimed at simultaneous detection of enhanced atomic and molecular signals at low pressure conditions”. Spectrochimica Acta Part B. 2019. 157: 12–21.
33. J. Moros, M.M. ElFaham, J.J Laserna, “Dual-Spectroscopy Platform for the Surveillance of Mars Mineralogy Using a Decisions Fusion Architecture on Simultaneous LIBS-Raman Data”. Analytical Chemistry 2018. 90: 2079−2087.
34. K.M. Muhammed Shameem, V.S. Dhanada, S. Harikrishnan, S.D. George, V.B. Kartha, C. Santhosh, V.K. Unnikrishnan, “Echelle LIBS-Raman system: A versatile tool for mineralogical and archaeological applications”. Elsevier B.V. 2020.
35. F. Matroodi, S. H. Tavassoli, “Experimental investigation on concurrent laser-induced breakdown spectroscopy Raman spectroscopy”. Applied Optics. 54(3): 2015.
36. R.C. Wiens, S.K. Sharma, J. Thompson, A. Misra, P.G. Lucey, “Joint analyses by laser-induced breakdown spectroscopy (LIBS) and Raman spectroscopy at stand-off distances”. Spectrochimica Acta Part A. 2005. 61: 2324–2334.

37. J. Moros, J.A. Lorenzo, P. Lucena, L.M. Tobaria, J.J. Laserna, “Simultaneous Raman-LIBS for the standoff analysis of explosive materials”. Spectroscopy Europe. 2010. 22(3).

38. J. Moros, J.A. Lorenzo, P. Lucena, L.M. Tobaria, J.J. Laserna “Simultaneous Raman Spectroscopy-Laser-Induced Breakdown Spectroscopy for Instant Standoff Analysis of Explosives Using a Mobile Integrated Sensor Platform”. Analytical Chemistry 2010. 82: 1389–1400.

39. J. Moros, J. A. Lorenzo, J. J. Laserna, “Standoff detection of explosives: critical comparison for ensuing options on Raman spectroscopy–LIBS sensor fusion”. Analytical and Bioanalytical Chemistry. 2011. 3353–3365.

40. A.K. Strange Fessler, A. Waldron, A. Colón, J.C. Carter, S.M. Angel, “A demonstration of spatial heterodyne spectrometers for remote LIBS, Raman spectroscopy, and 1D imaging”. Spectrochimica Acta Part B. 2021. 179.

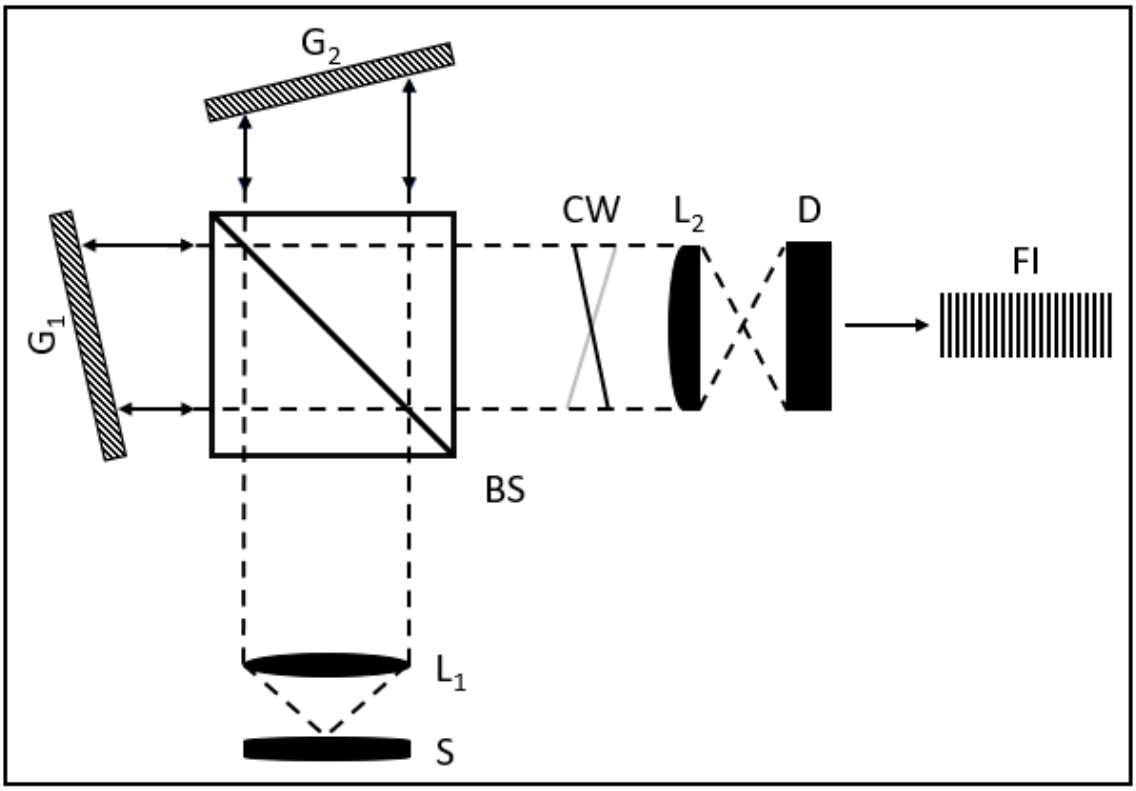

Figure 2.1 Schematic diagram of the SHS system. S: sample; L_1: collection lens; BS: beam splitter; G_1 and G_2: dispersive gratings, CW: crossing wavefront, L_2: imaging lens, D: CCD detector, FI: fringe image.

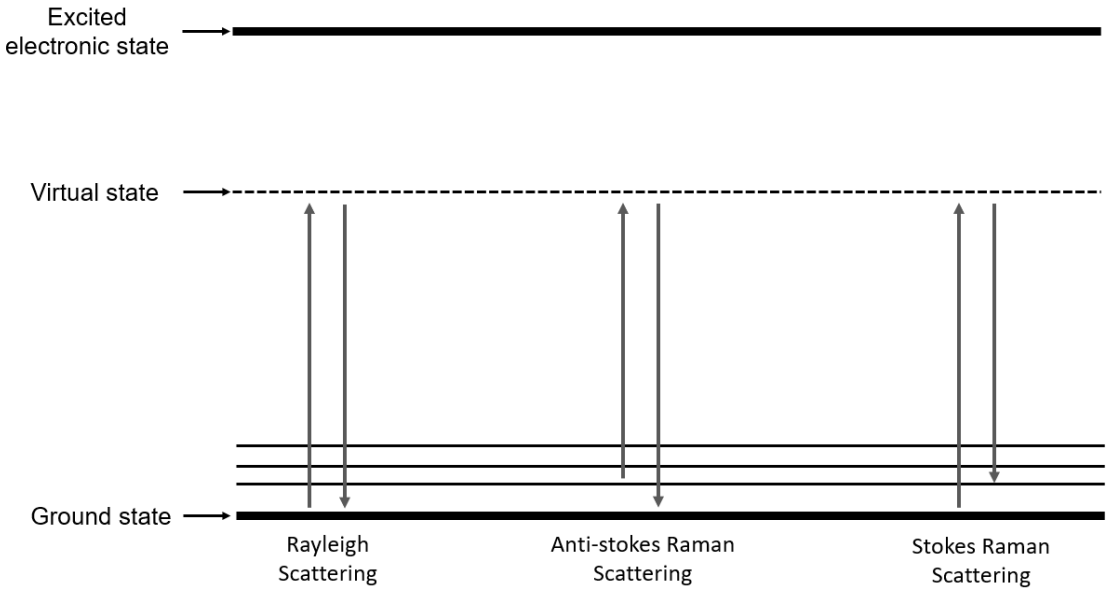

Figure 2.2 Jablonski energy level diagram for Rayleigh scattering and Raman anti-Stokes scattering and Stokes scattering.

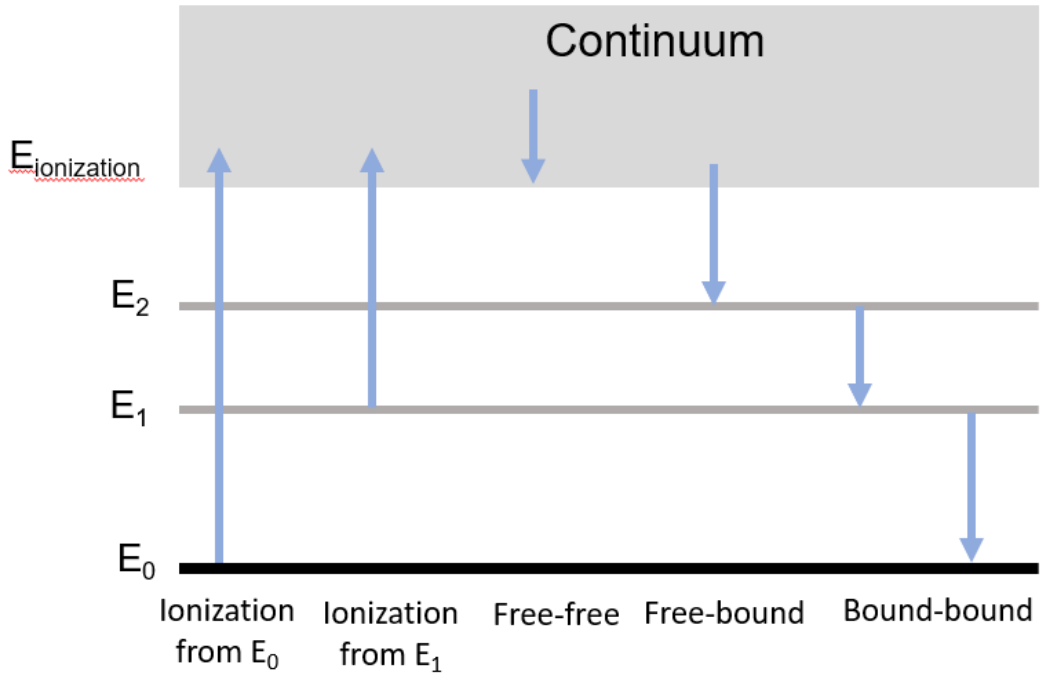

Figure 2.3 Energy level diagram of LIBS for emission of excited atoms and ions.

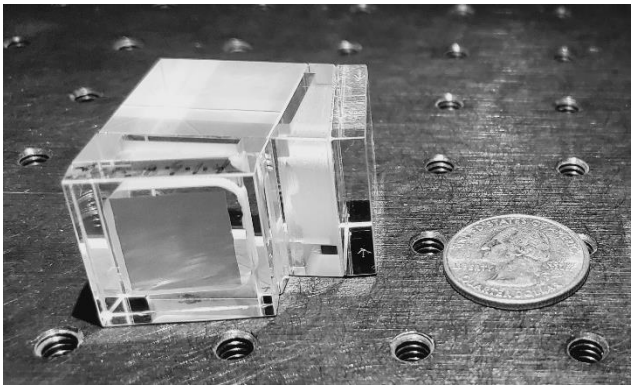

Figure 2.4 monolithic Spatial Heterodyne Spectrometer.

CHAPTER 3

CHARACTERIZATION OF MONOLITHIC SPATIAL HETERODYNE LASER INDUCED BREAKDOWN SPECTROSCOPY: INITIAL TESTS

3.1 Introduction

Laser induced breakdown spectroscopy (LIBS) is an important analysis technology that permits fast and direct analysis.[1] First reported by Brech and Cross in 1962,[4] LIBS yields simultaneous sensitivity to many elements in the parts-per-million (ppm) range for solids, liquids, gases, and aerosols with no sample preparation required. It is also fast, requiring under 1s for a measurement making it ideal for real-time analysis. These characteristics are some of the most important advantages of LIBS compared to other analytical approaches.[1] LIBS produces a plasma which ablates and ionizes the sample. This plasma is photo absorption dominated by inverse Bremsstrahlung (IB) absorption, in which free electrons get kinetic energy directly from the laser beam and photoionization of excited species. Because early time continuum radiation cannot be reduced by averaging, LIBS spectra are obtained by gating the detector so that data collection is delayed relative to the laser pulse. Plasma lifetime at atmospheric pressure is typically 30-50 μs, so that delay times of 1-10 μs and data collection intervals of 5-20 μs are typical. Elements in LIBS spectra can be qualitatively identified by comparison to standard libraries of spectral data maintained by NIST.[3]

This has lead to the development of remote (or remote) LIBS where measurements are made on samples many tens of meters distant from the spectrometer. Remote LIBS has been used for applications as diverse as explosives detection[4-6] underwater exploration and mining, planetary exploration,[7,8] and assessment of damage to historical monuments,[9] Remote LIBS has been shown to be useful at distances up to many tens of meters and has also been combined with remote Raman.[10,11]

Measuring samples remotely using LIBS introduces issues with low collection solid angle, which results in low LIBS signal levels. To overcome this issue telescopes are usually used for light collection. However, the amount of light collected is limited by the throughput of the spectrometer, which is inherently very low because of the need for small slits (approximately 50-100 um) to achieve the spectral resolution needed for LIBS. Another problem unique to remote LIBS is movement of the laser focus on the sample when plasmas are being produced. For samples at large distances it can be difficult maintaining the laser focus within the field of view of the spectrometer thus, laser pointing stability issues can make spectrometer alignment issues more severe.

In this chapter, a new type of LIBS spectrometer, the monolithic spatial heterodyne LIBS spectrometer (mSHLS) is introduced to combat these issues. The spatial heterodyne spectrometer (SHS) was described by Harlander in 1991. The design is like a Michelson interferometer but with tilted diffraction gratings, so there are no moving parts, and there are no entrance or exit slits.[11,12] This design allows for miniaturization[13-16] of the spectrometer because the spectral resolution is not strongly dependent on the size of the device or a slit size as with conventional dispersive spectrometer and it has a high throughput since the optical etendue of the SHLS is several orders of magnitude higher

than conventional slit based LIBS spectrometers of the same resolving power. Since the SHLS has no moving parts, it can be built as a solid state or monolithic device. The mSHLS has been recently described.[17] This spectrometer has demonstrated higher stability and precision than the previous free standing SHLS design and offers many advantages over the conventional LIBS spectrometers. These advantages include 10 to 100 times larger acceptance angle, 10^2 to 10^4 higher light throughput, very high spectral resolution, a wide spectral range, and robustness.[17,18]

3.2 Experimental

The monolithic Spatial Heterodyne Spectrometer (mSHS) described here was custom built by LightMachinery, Inc. (Canada). The mSHS was cemented together using a UV-curable epoxy, to make the monolithic interferometer. The interferometer consisted of two 15 mm by 15 mm diffraction gratings, a 25 mm N-BK7 50:50 cube beam splitter, and two N-BK7 spacers that define the angle in which the gratings are tilted in the horizontal plane (e.g., the dispersion plane), with respect to the optical axis. All optical faces were antireflection coated to minimize spurious reflections from the zeroth- and second-order diffracted beams. For this experiment, 150 grooves/mm gratings blazed at 500 nm, with the grating angle set by the spacers, to give a 531.6 nm Littrow wavelength (spacer angles of 2.288°) was used.

Figure 3.1 shows the monolithic spatial heterodyne LIBS spectrometer. For LIBS measurements, a plasma was generated on the sample using a Continuum Surelite III (Continuum, San Jose, CA, USA) pulsed laser, doubled to 532 nm at ~87 mJ/pulse for benchtop (non-remote) measurements and ~200 mJ/pulse for all remote measurements. The laser was focused onto the sample off-axis, using an f/2, silica lens (L_1) for benchtop

measurements. In the case of remote LIBS measurements, samples were excited off axis using either a 5x beam expander or an f/4 fuse silica lens to control the spot size on the sample. The only collection optics used was the mSHLS and the signal was collimated using two irises, I_1 and I_2 set 14 mm in size to ensure that the signal does not over fill the gratings of the mSHLS. Two filters (F), 532 nm long-pass filter (Semrock RazorEdge, LP03-532RE-25) were placed in front of the mSHLS to block wavelengths below the Littrow wavelength for samples the had lines above the Littrow wavelength and no filters were used for other measurements. A Nikon AF Nikkor 85 mm f/4 1:1.8D lens (Nikon, Tokyo, Japan), L_2, was used to image the plane of the mSHLS diffraction gratings onto a 1024 x 256 pixel, gated ICCD array detector with 26 μm pixels (Princeton Instruments, Model PIMAX4) and operated using Lightfield 6.3 software at the following settings: thermoelectric cooling to -25^{0}C, 100 kHz ADC; high gain and low noise. The imaging lens provided a ~1.7x magnification so the image of the 14 mm diffraction grating on the detector was ~24 mm, almost filling the detector in the horizontal direction but overfilling the vertical direction. For all measurements, a spatial filter, I_3, was placed one focal length behind the imaging camera lens, L_2, on the CCD side, to block higher mSHLS grating diffraction orders.

3.3 Samples

Copper plates of unknown purity were obtained from an industrial supply company along with magnesium rods (99.9+%, item number: 299405, Sigma Aldrich, St. Louis, MO, USA), manganese chips (99%, item number: 266167, Sigma-Aldrich, St. Louis, MO, USA) and iron filings of unknown purity pressed into a pellet.

3.4 Results and discussions

Light entering the mSHLS is split into two beams by the beam splitter. The beams strike the tilted diffraction gratings such that one wavelength, the Littrow wavelength λ_L, is retro-reflected along the incident light path which recombines at the beamsplitter and are diffracted back along the same direction. The grating tilt angle defines the Littrow wavelength, the wavelength at which both beams exactly retro-reflect and produce no fringe pattern at the detector.[11] This means that the angle of incidence is equal to the angle of diffraction and a zero-path difference is produced between the two beams meaning no interference pattern will be observed for this particular wavelength. The grating angle which corresponds to the Littrow wavelength is known as the Littrow angle and can be calculated using the grating equation Eqn. 3.1

$$n\lambda = d(sin\alpha + sin\beta) \tag{3.1}$$

where n is the diffraction order, λ is the desired wavelength, d is the grating groove density, α is the angle of incidence, and β is the angle of diffraction. By setting the angle of incidence and angle of diffraction equal, Eq. 3.1 can be simplified and the Littrow angle, θ_L, of a specific wavelength λ can be calculated in Eq. 3.2 as,

$$\theta_L = sin^{-1}(\lambda/2d) \tag{3.2}$$

For any wavelength other than Littrow, the recombined light produces a crossed wave front, of which the crossing angle is wavenumber dependent and produces an interference pattern at the interferometer output. This output is then imaged onto the detector, and the spectrum is extracted using a Fourier Transform method. The number of fringes, f, across the CCD is related to the Littrow wavenumber by Eq. 3.3:

$$f = 4(\sigma-\sigma_L)\tan\theta_L \quad (3.3)$$

where f is in fringes/cm, σ_L is the Littrow wavenumber, and σ is wavenumber of interest. According to Eq. 3.3, emission lines above or below the Littrow wavelength may show identical fringe patterns and can lead to degenerate lines (i.e., line overlap). It has been demonstrated that by tilting one grating vertically the fringes rotate and overlap can be removed. In this case, the fringe pattern is rotated clockwise for bands below the Littrow wavenumber and rotated counterclockwise for bands above the Littrow wavenumber. The tilted grating design result in a doubling of the spectral range of the mSHLS and is referred to as a 2D mSHLS.[12]

The resolving power, R, is determined by the total number of grooves illuminated on the two gratings. Therefore, the mSHLS does not require a narrow slit to achieve high resolution as is common with dispersive spectrometers because there is no dependence of resolution upon entrance aperture width. This allows the mSHLS to employ very large entrance apertures, greatly increasing the throughput of the system, which is advantageous when signal strength is low such as when the source is very far from the detector in a remote configuration.[14] For a mSHLS built with two fully illuminated gratings of size W and groove density d, the resolving power is expressed as Eq. 3.4

$$R = 2Wd \quad (3.4)$$

The resolving power in this case is R = 4200, giving a theoretical resolution of ~ 0.1 nm at 500 nm. The collection solid, Ω, angle of the mSHLS is related to the resolving power shown by Eq. 3.5[12]

$$\Omega = 2\pi/R \quad (3.5)$$

For this spectrometer the maximum, resolution-limited solid angle field of view (FOV) is then 1.4×10^{-3} sr, and the full acceptance angle is ~ 1.3°. The theoretical maximum bandpass of the mSHLS is determined by the resolving power, *R*, and the number of pixels, *N*, in the horizontal direction on the detector.[15-17] The Nyquist limit sets the highest fringe frequency that can be measured by the detector to the frequency that produces N/2 fringes. The theoretical bandpass, *BP*, can be calculated using Eq. 3.6

$$BP = N\lambda_L/2R \tag{3.6}$$

where N is the number of pixels in the horizontal direction. Due to the limits of the intensifier on the detector about 700 ICCD pixels were illuminated horizontally, thus about 350 wavelength elements can be measured giving, a theoretical ICCD-limited spectral range of ~ 44 nm on either side of the Littrow wavelength. This range is doubled if wavelengths above and below Littrow are considered.

Benchtop LIBS measurements of copper, magnesium, iron, and manganese were taken by placing solid samples on the optical axis, 1.0 m from the mSHLS entrance aperture. No collection optics were used to obtain the LIBS emission into the system; light was collected only by the 14 mm diffraction gratings. Laser pulses were ~ 86.7 mJ/pulse with a 0.41 mm diameter spot size at the target and each sample spectrum was acquired using 500 laser shots at an ICCD gain of 100. Figure 3.2 shows LIBS emission spectra of (a) Cu and (b) Mn metal samples. Cu spectra were measured at wavelengths below the 531.6 nm Littrow but close to the laser wavelength and Mn spectra were measured at wavelengths above the Littrow wavelength. These elements show relatively strong emission lines in this spectral range with good signal to noise ratio. The FWHM of the strongest emission lines for both elements are about 0.2 nm which is very close the

mSHS theoretical resolution. The insets show the interference fringe patterns, I, background subtracted cross section and the fringe images, FI. The FV is 0.11 for Cu and 0.29 for Mn. This low value is likely due to the slight tilt on the fringes added by the monolith. The three strong Cu lines at ~ 510, 515 and 522 nm (note, these are below the mSHLS Littrow wavelength) match Cu emission lines listed in the NIST spectral data base.[4] The Cu spectrum was calibrated in wavelength using the known wavelengths of the three strong Cu I lines. This calibration curve was useful in identifying lines in spectra collected from different samples as well as for identifying lines at wavelengths above the Littrow wavelength that overlapped the spectral region shown. Two very weak lines, at ~ 496 and 502 nm match Cu I emission lines that appear above the Littrow wavelength at 570.0 and 562.9 nm, respectively. As shown by Eq. 3.3, lines like this above the Littrow wavelength also show up below Littrow, unless blocked by appropriate filters.[18] In the case of the Mn emission spectra, a 532 nm long pass filter was used to prevent overlap of lines below the Littrow wavelength. Figure 3.3 shows emission spectra of (a) Mg and (b) Fe metal samples. The FV were 0.05 and 0.06 for Mg and Fe respectively. The three strongest Mg lines at 516.7, 517.3 and 518.4 match known Mg I emission lines that are listed in the NIST spectral data base. The very weak line at ~ 512 nm matches a Mg I emission line that appears above the Littrow wavelength at 552.8 nm. Note that the Fe and Mn emission spectrum is shown above the Littrow wavelength. Since a 532 nm long pass filter was used for both measurements of Fe and Mn there is no overlap from lines below the Littrow wavelength.

Remote mSHLS measurements were conducted at a distance of 4.5 meters. The 4.5 m of the laser pulse from the laser to the sample, and the resulting LIBS emission

returning to the mSHLS takes about 0.25 – 0.40 μs, an order of magnitude smaller than the gate delays used in the benchtop configuration. Because the signal was weaker, the number of summed laser shots was increased from 500 to 1000. A 63.5 mm diameter fused silica lens with a 609.6 mm focal length was introduced on-axis with the mSHLS for light collection and an f/4 lens was used to focus a plasma on the sample. Figure 3.4 shows LIBS spectra of (a) Cu, (b) Mn, (c) Mg and (d) Fe using this setup. For these measurements 1000 laser shots were accumulated for each spectrum and detector gain remained at 100.

The field of view for the SHS is the maximum acceptance angle for which the widest angle of light does not produce an interferogram which differs from the interferogram produced by on-axis light by more than one fringe.[9] As described above, without using any collection optics the acceptance angle of the SHLS is 1.3°, corresponding to a FOV of ~ 100 mm for a sample distance of 4.5 m. Thus, light originating from greater than ~ 0.65° on either side of the optical axis should degrade the quality of the interferogram. To test this, the FOV was measured by placing a 110 mm wide strip of Cu, 4.5 m from the front of the spectrometer with the center of the Cu strip aligned with the optical axis of the spectrometer. Spectra were collected in triplicate with the laser focus directed by a 5x beam expander in random order to positions along the Cu strip and no collection optics except for that of the mSHLS were used. Figure 3.5 shows that the baseline-subtracted intensity of the 522 nm metal Cu line, plotted as a function of angle from the optical axis. This is relatively constant within +/- 0.2 degrees from the optical axis, then drops off quickly at larger angles. This result agrees well with the expected theoretical acceptance angle of the SHLS. The rapid decrease in intensity at

angles greater than ~ 0.6° is because the light travels through the mSHLS at such an extreme angle that part of the beam completely misses the ICCD.[12] The fact that light can enter the system up to 0.6° off axis through a large aperture without detriment to the interferogram also allows for relaxed alignment requirements for coupling collection optics to the mSHLS. This makes it easier to introduce a telescope to improve light collection, since it is much easier to align to the large aperture of the mSHLS than with the small slit on a conventional dispersive spectrometer.

3.5 Conclusion

Remote LIBS with the monolithic spatial heterodyne spectrometer has been demonstrated. The wide field of view of the mSHLS, demonstrated successful recovery of spectra with LIBS plasma deviating from the optical axis of the spectrometer by ~ 0.6°, and high throughput of the mSHLS allowing LIBS spectra to be collected at distances up to 4.5 m with no collection optics. The addition of a small telescope for light collection increased the amount of light collected by an order of magnitude, even while accumulating 500 fewer laser shots per spectrum.

3.6 References

1. J. Scaffidi, S.M. Angel, D.A. Cremers, “Emission Enhancement Mechanism in Dual-Pulse”. American Chemical Society. 2006. 25-32.
2. Brech, F., Cross, L., “Optical microemission stimulated by a ruby laser”. Applied Spectroscopy. 1962. 16: 59.
3. A. Kramida, Y. Ralchenko, J. Reader, NIST ASD Team. “NIST Atomic Spectra Database (version 5.3).” National Institute of Standards and Technology, Gaithersburg, MD. http://physics.nist.gov/asd [accessed July 30 2020].

4. S. Rosenwasser, G. Asimellis, B. Bromley, R. Hazlett, J. Martin, T. Pearce, A. Zigler, “Development of a method for automated quantitative analysis of ores using LIBS”. Spectrochimica Acta Part B. 2001. 56: 707-714.
5. Bonvallet J.C. Issues in Laser Induced Breakdown Spectroscopy for Measurements in the Deep Ocean and Other High-Pressure Environments. [PhD Dissertation]. University of South Carolina, 2016.
6. C. López-Moreno, S. Palanco, J.J. Laserna, F. DeLucia Jr., A.W. Miziolek, J. Rose, R.A. Walters, A.I. Whitehouse. “Test of a stand-off laser-induced breakdown spectroscopy sensor for the detection of explosive residues on solid surfaces”. Journal of Analytical Atomic Spectrometry. 2006. 21: 55-60.
7. R. González, P. Lucena, L.M. Tobaria, J.J. Laserna. “Standoff LIBS detection of explosive residues behind a barrier”. Journal of Analytical Atomic Spectrometry. 2009. 24(8): 1123– 1126.
8. V. Lazic, A. Palucci, S. Jovicevic, M. Carapanese, C. Poggi, E. Buono. “Detection of explosives at trace levels by Laser Induced Breakdown 126 Spectroscopy (LIBS)”. Chemical, Biological, Radiological, Nuclear, and Explosives (CBRNE) Sensing XI, Proceedings of SPIE. 2010. 7665.
9. S.K. Sharma, A.K. Misra, P.G. Lucey, R.C.F. Lentz. “A combined remote Raman and LIBS instrument for characterizing minerals with 532 nm laser excitation”. Spectrochim. Acta, A. 2009. 73: 468-476. (24)
10. S.K. Sharma, A.K. Misra, P.G. Lucey, R.C. Wiens, S.M. Clegg. “Combined remote LIBS and Raman spectroscopy at 8.6 m of sulfur-containing minerals, and minerals

coated with hematite or covered with basaltic dust". Spectrochim. Acta, A. 2007. 68(4): 1036-1045.

11. J. Moros, J.A. Lorenzo, P. Lucena, L.M. Tobaria, J.J. Laserna. "Simultaneous Raman Spectroscopy-Laser-Induced Breakdown Spectroscopy for Instant Standoff Analysis of Explosives Using a Mobile Integrated Sensor Platform". Analytical Chemistry. 2010. 82: 1389–1400.
12. J.M. Harlander. Spatial Heterodyne Spectroscopy: Interferometric Performance at Any Wavelength without Scanning. [Ph.D. Dissertation]. Madison, Wisconsin: University of Wisconsin-Madison, 1991.
13. N. R. Gomer, C.M Gordon, P. Lucey, S.K. Sharma, J.C. Carter, S.M. Angel, "Raman Spectroscopy Using a Spatial Heterodyne Spectrometer: Proof of Concept". Applied Spectroscopy. 2011. (65): 849-857.
14. P.D. Barnett, S. M. Angel, "Miniature Spatial Heterodyne Raman Spectrometer with a Cell Phone Camera Detector". Applied Spectroscopy. 2017. 71(5): 988–995.
15. P.D. Barnett, N. Lamsal, S. M. Angel, "Standoff LIBS using a Miniature Wide Field of View Spatial Heterodyne Spectrometer with Sub-Microsteradian Collection Optics". Applied Spectroscopy. 2017. 71: 583-590.
16. A. Waldron, A. Allen, A. Colón, J. C. Carter, and S. M. Angel, "A Monolith Spatial Heterodyne Raman Spectrometer: Initial Tests". Applied Spectroscopy. 2020. 75(1): 57-69.
17. N.S. Lamsal, S. M. Angel, "Deep-UV Raman Measurements Using Spatial Heterodyne Raman Spectrometer (SHRS)". Applied Spectroscopy. 2015. 69: 525-234.

18. K. A. Strange Fessler, A. Waldron, A. Colón, J.C. Carter, S.M. Angel, “A demonstration of spatial heterodyne spectrometers for remote LIBS, Raman spectroscopy, and 1D imaging”. Spectrochimica Acta Part B. 2021. 179.

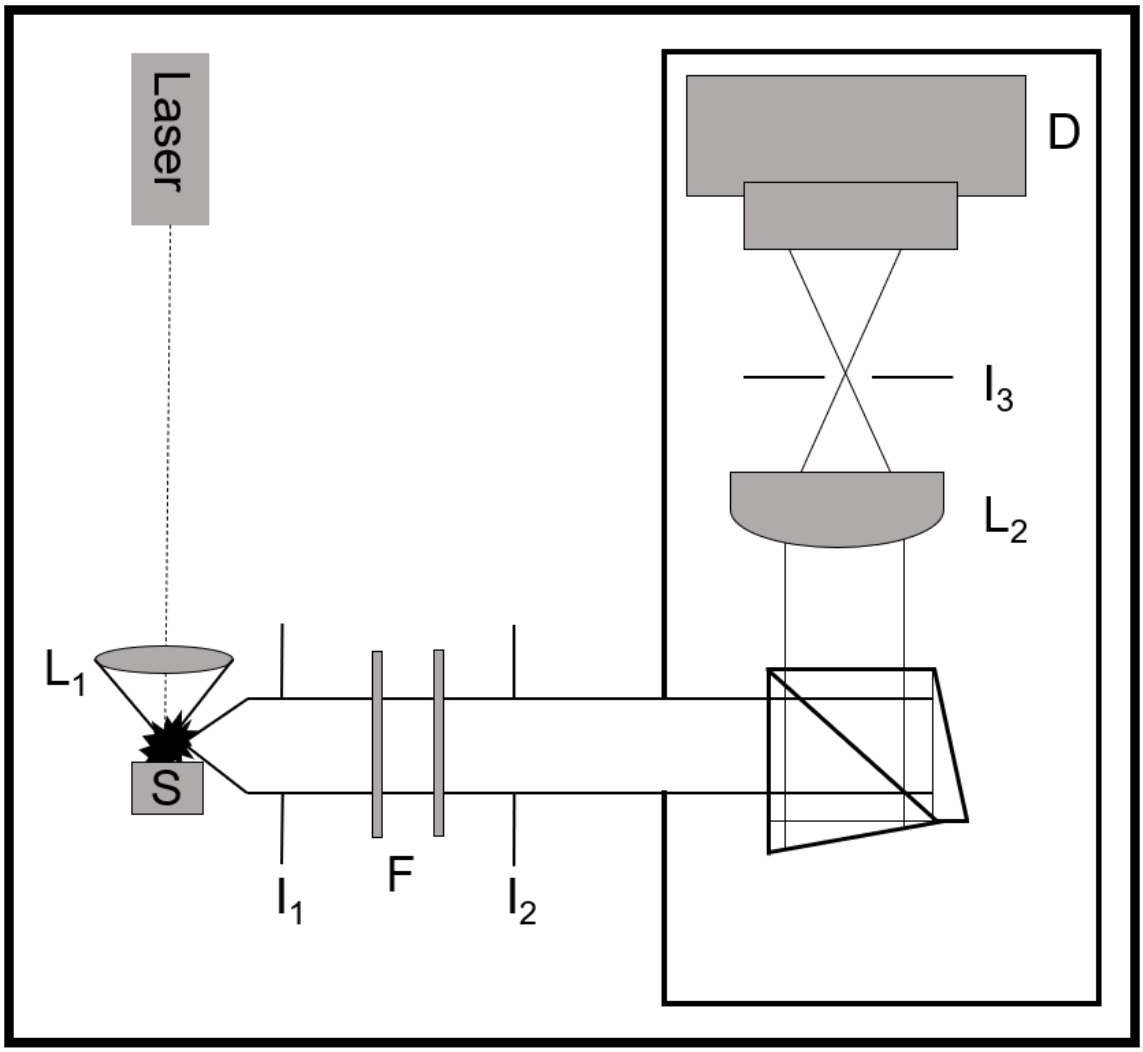

Figure 3.1 Schematic diagram of the mSHLS system. S: sample, L_1: focusing lens, F: filters, I1 and I2: iris, L_2: imaging lens, I_3: spatial filter; D: ICCD detector.

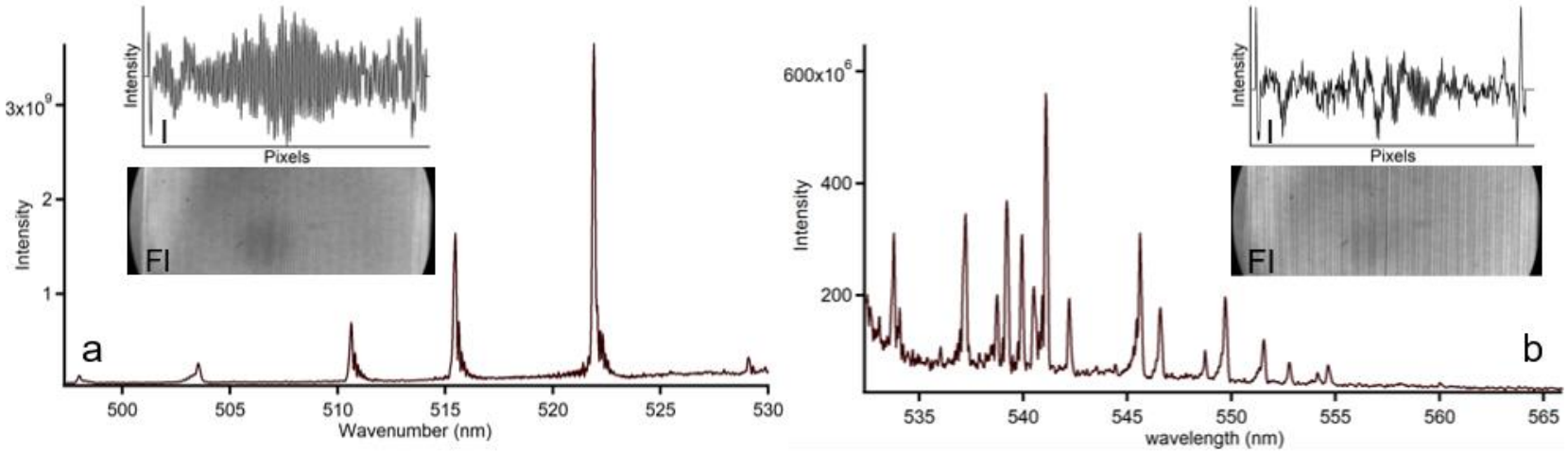

Figure 3.2 Benchtop LIBS spectra of (a) copper metal and (b) manganese metal using the monolithic SHLS, for samples at 1 m. Insets: interferogram/cross sections, I, for each spectrum, generated by summing the intensity of each column of pixels in the fringe image, FI, and applying background subtraction. The gate delay was 2.2 μs and the gate width was 10 μs. Benchtop measurements were made using 500 laser shots.

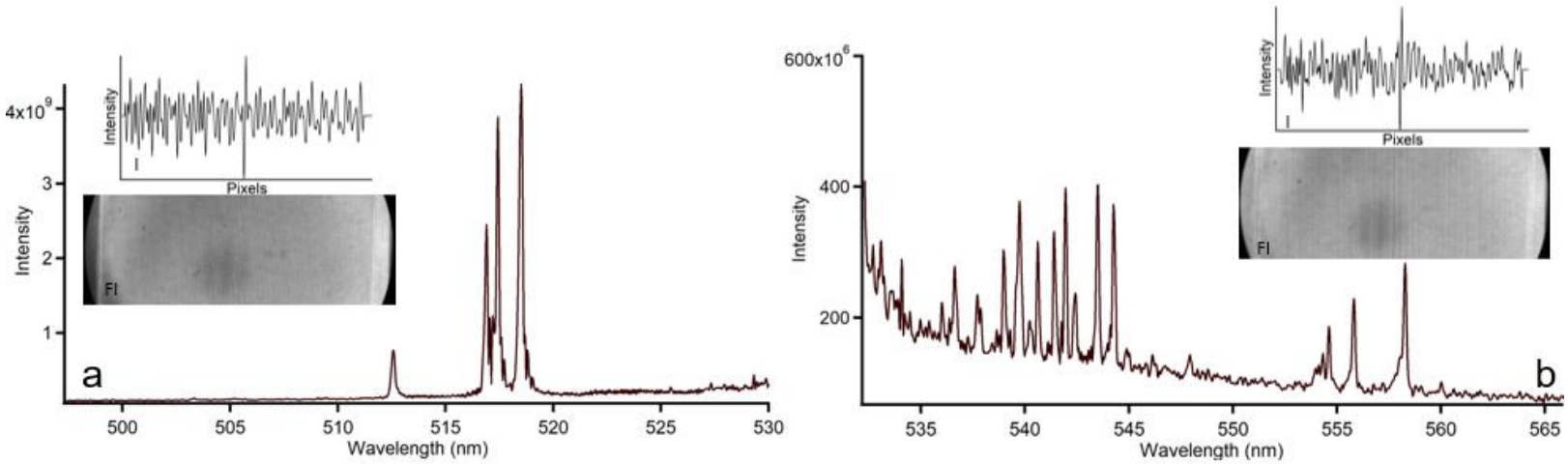

Figure 3.3 Benchtop LIBS spectra of (a) magnesium metal and (b) Fe metal using the monolithic SHLS, for samples at 1 m. Insets: interferogram/cross sections, I, for each spectrum, generated by summing the intensity of each column of pixels in the fringe image, FI, and applying background subtraction. The gate delay was 2.6 μs and 2.4 μs for magnesium and iron respectively. The gate width was 10 μs for both. Benchtop measurements were made using 500 laser shots.

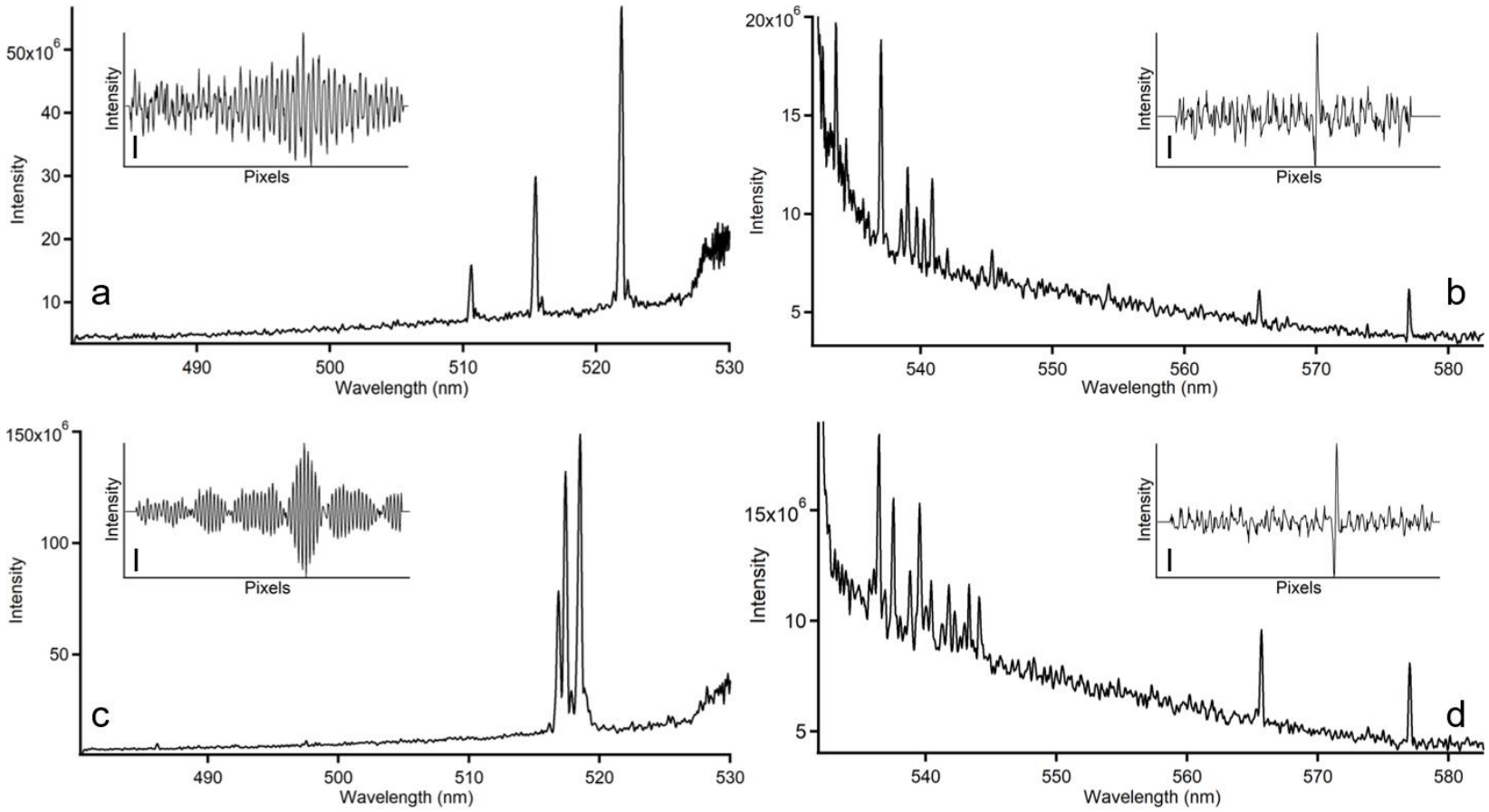

Figure 3.4 Remote LIBS spectra of (a) Cu, (b) Mn, (c) Mg and (d) Fe using the monolithic SHLS, for samples at 4.5 m. Insets: interferogram/cross sections, I. The gate delay was 0.35 us, 0.45, 0.45, and 0.20 for copper, manganese, magnesium, and iron, respectively. Because of software issues, the gate width, rather than gate delay, was changed to compensate for the delay of the emission signal reaching the detector after the laser shot, a gate width of 2000 μs for all remote measurements was used. This resulted in higher than expected noise for the remote measurements. Remote measurements were made using 1000 shots.

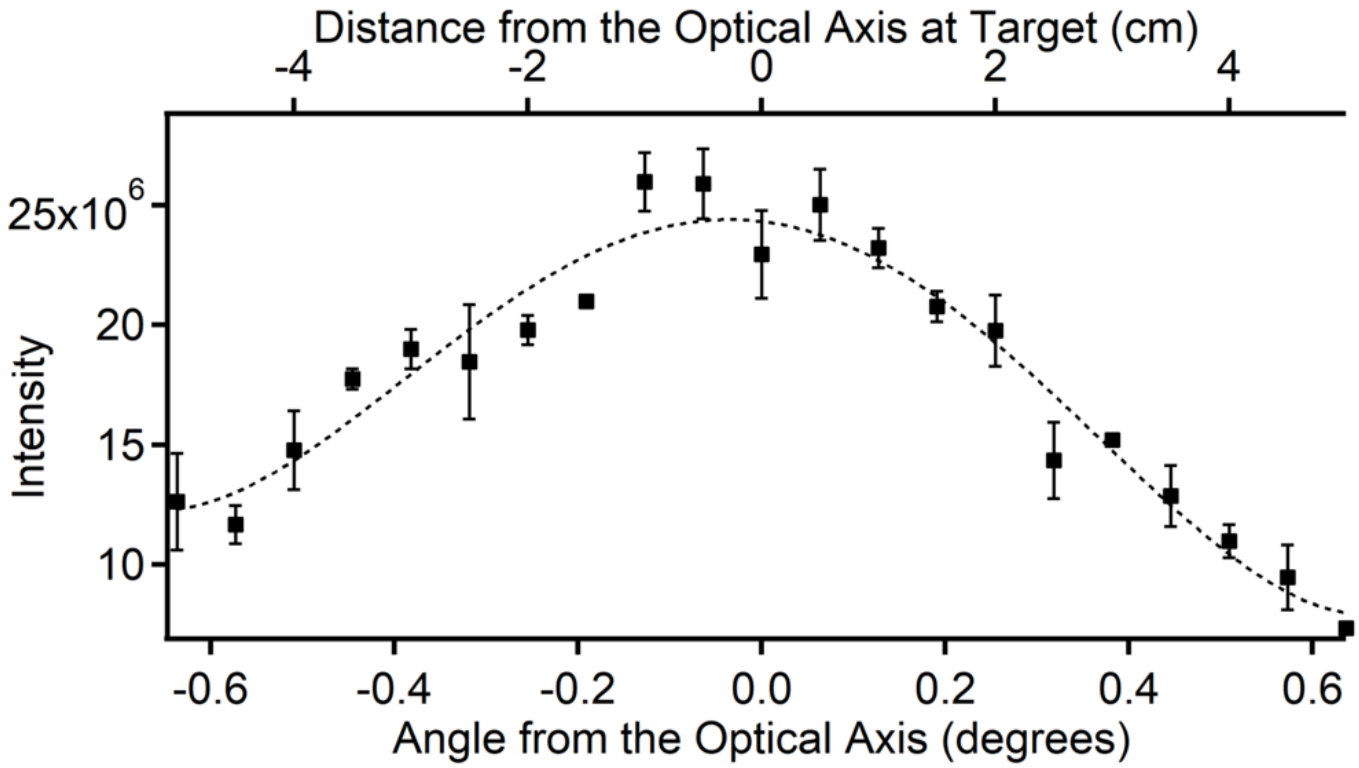

Figure 3.5 Metal copper remote LIBS emission intensity, plotted versus the position of the focused laser spot on the sample, relative to the optical axis, with the copper sample placed 4.5 m from the mSHLS. Each position was repeated in triplicate with the position of the laser spot randomized. No collection optics were used for these measurements, other than the 15 mm mSHS gratings.[1]

CHAPTER 4

CROSS-DISPERSED MONOLITHIC SPATIAL HETERODYNE SPECTROSCOPY WITH A TRANSMISSION GRATING

4.1 Introduction

The spatial heterodyne spectrometer (SHS), described by Harlander[1] and Harlander et al.,[2] is a fixed grating interferometer with no moving parts that can provide high spectral resolution in a very small footprint. The SHS has a large entrance aperture and wide acceptance angle that provides high light throughput for extended sources, at least two orders of magnitude higher than a conventional dispersive spectrometer.[1,3] The first description of a spatial heterodyne Raman spectrometer (SHRS) was demonstrated for visible Raman spectroscopy,[4] UV Raman,[5,6] remote Raman,[5,7] laser-induced breakdown spectroscopy,[8,9] hyperspectral Raman imaging[10] and recently for cross-dispersion SHRS.[11] The SHRS design has advantages for Raman spectroscopy when a small, high-resolution spectrometer with a wide field of view is desired. Lamsal et al., showed that the wide field of view can be used to minimize sample degradation in deep-UV Raman measurements by using a defocused laser.[5,6] In the case of remote Raman, the wide acceptance angle and large aperture makes the SHRS relatively easy to couple with telescopic optics and minimizes laser pointing stability issues because small movements of the laser spot on the target do not reduce the amount of light collected by the

spectrometer aperture, unlike the case of a dispersive spectrometer where the output of the telescope has to be held in focus on a narrow input slit.[7,12] However, the throughput advantage of the SHS does not typically result in increased sensitivity. When an SHS interferogram is limited by photon noise, the SHS suffers from the multiplex disadvantage, meaning that photon noise associated with any one spectral feature is distributed equally into every other spectral feature as well. As the total photon noise increases, so does the multiplex noise floor, thus limiting the detection of weak spectral features.[11] There are a number of ways to attain SHS spectra with high signal-to-noise ratios (SNR), for example one way is achieved by utilizing bandpass filters that reject spectral light beyond the Nyquist wavelength.[13,14] Other attempts have been made to limit the spectral density within an SHS interferogram, notably the echelle grating SHS variant which uses various high diffraction grating orders to spatially offset narrow bandpass onto a CCD.[15] Recently the cross-dispersion technique with a free-standing SHRS (x_ASHRS) was demonstrated.[11] This was done by pairing an Amici prism with the SHRS which diminished the multiplex disadvantage and minimized the shot noise in weak bands, by dispersing Raman wavelengths vertically across the detector, separating strong and weak Raman bands, thus increasing the SNR of the weaker Raman bands in cyclohexane.[11] The x_ASHRS technique could be improved by employing a more robust and stable interferometer such as the monolithic spatial heterodyne spectrometer (mSHRS) that we recently described,[16-18] and using a dispersion optic with higher linear dispersion than the Amici prism to give less shot noise and higher SNR. In the mSHRS, all of the optical components of the spectrometer are bonded together. This makes the system robust to vibrations and shock and very stable.[16-18] In this paper we combine a

mSHRS with a cross-dispersion transmission grating (x_gmSHRS) and compare the resolution and signal to noise ratio (SNR) of spectral features for a variety of samples with the use of the mSHRS without a cross-dispersion element.

4.2 Experimental

Monolithic Spatial Heterodyne Raman Spectrometer (mSHRS)

The mSHRS described here was custom-built by LightMachinery, Inc. (Canada) based on our original design. The interferometer consists of two 15 mm x 15 mm 600 grooves/mm diffraction gratings, blazed at 500 nm, a 25 mm N-BK7 50:50 cube beam splitter, and two N-BK7 spacers to set the angle of the gratings at 9.326^o in the horizontal plane (i.e., the dispersion plane), to provide a 541.27 nm Littrow wavelength for the mSHRS (see Figure 1). All optical faces were antireflection coated to minimize spurious reflections from the zeroth- and second-order diffracted beams. The 1D mSHRS device is about 3.5 x 3.5 x 2.5 cm in size and weighs about 80 g and was used for 180° backscatter measurements.

A 532 nm continuous wave (CW) neodymium-doped yttrium aluminum garnet laser (Opto Engine, MGL-FN-532nm-1W) was used as the excitation source for all spectra shown, with laser power on the samples varying from 7 mW to 150 mW. For most sample studies, the laser beam was directed onto the sample using a 50 mm diameter, 550 nm long-pass dichroic mirror, M_1, (ThorLabs, DMLP550L) at 45^o, then focused onto the sample using a 25.4 mm, NBK coated, f/4 achromatic lens, L1, (Thorlabs AC254-100-A). The same lens also collected the Raman scattered light and collimated it, sending the signal into the mSHRS through two 10 mm circular apertures,

I_1, placed approximately 25 mm apart, to ensure beam collimation. The 10 mm collimated beam was reflected using two aluminum mirrors, $M_{2,3}$, at 45^o, through the 13.5 mm x 12.5 mm transmission grating, G, (Ibsen Photonics, Spectrometer grating, FSTG-VIS1379-911), at an angle of about 20^o so that the first order diffraction, in the vertical direction, was on the input optical axis of the mSHRS. An iris, I_2, was placed ~ 25 mm away from the transmission grating to block overlapping diffraction orders. A 100 mm focal achromatic cylindrical lens, CL, (Thorlabs, ACY254-100-A) was used to focus diffracted light, to form a vertically dispersed spectrum on the mSHRS gratings. Two filters (F), a 532 nm long-pass filter (Semrock RazorEdge, LP03-532RE-25) and a 532 nm holographic notch filter (Thorlabs, NF533-17) were placed in front of the mSHRS to remove strong laser scatter. For sulfur samples, an additional 559 nm band-pass filter (Thorlabs, MF559-34) was used. A back-illuminated thermoelectrically cooled, UV-enhanced, 2048x512 pixel charge-coupled device (CCD, Princeton Instruments-PI, PIXIS-2048 2K/BUV) detector, with 13.5 um pixels, cooled to -70^o C, and run at 100 kHz with ADC gain high and in the low noise setting, was used to image the grating faces onto the CCD detector at a magnification of 1.7x, so as to fill as much of the detector in the horizontal direction as possible. All spectra were measured using Lightfield 6.3 software. The magnified image filled 1900 pixels in the horizontal direction, limited by the camera mount. For all measurements, a spatial filter, I_3, was placed one focal length behind the imaging f/X camera lens, L_2, on the CCD side, to block higher mSHRS grating diffraction orders. For non-cross dispersed mSHRS measurements, M_2, M_3, G, and CL were removed. All other parameters stayed the same. Specifications for our previously described prism based x_ASHRS[11] are shown in Table 4.1, in comparison to the

current grating-based device. For measurements of sulfur isotopes, the SNR of the mSHRS and x_gmSHRS were also compared to measurements made using a conventional microRaman spectrometer (Horiba Model LabRam). All data processing was done using MatLab version 2020b and Igor Pro 8.

mSHRS Spectrometer specifications

The nominal resolving power, R, of the mSHRS, as determined by the total number of grooves illuminated on the two gratings is 12,000, which gives a theoretical resolution of ~ 1.6 cm^{-1} at the laser wavelength of 532 nm. The experimentally measured spectral resolution is usually lower than the calculated value, limited by CCD image contrast and the ability to resolve closely-spaced fringes on the CCD. A feature of the SHS design is a large collection solid angle, Ω, for extended sources (given by Eq. 1:). For the mSHS used in these studies, the maximum, resolution-limited collection solid angle is $5.2x10^{-4}$ sr, giving a full acceptance angle of ~ 1.3°

$$\Omega = 2\pi/R \qquad 4.1$$

The spectral range, or theoretical maximum bandpass, BP, of the mSHRS is determined by the resolving power, R, and the number of pixels, N, illuminated in the horizontal direction on the detector.[4] The BP of the mSHS used here, calculated using Eq. 2, is ~43 nm from the Littrow wavelength (~1335 cm^{-1}). This should be taken as an estimate only because of uncertainties in things like the beam size, beam spread, grating angle, and other things that affect R and N.

$$BP = N\lambda_L/2R \qquad 4.2$$

4.3 Samples

Sulfur (Sigma-Aldrich), potassium perchlorate (Alfa Aesar), and sodium sulfate (Sigma-Aldrich) were purchased at 99% purity and pressed into pellets using a hydraulic pellet press (Carver Laboratory Equipment, model 3912) using a 13mm stainless steel pellet die. Barite was obtained from an Introductory Earth Science Collection (American Educational, #1201-000). Sulfur isotopes ^{34}S and ^{32}S were purchased at 99.8% and 99.9% respectively (Buy isotope Neonest AB). Isopropanol (Sigma-Aldrich), and cyclohexane (Sigma-Aldrich) with 99% purity were measured in 1 cm quartz cuvettes.

4.4 Results and Discussion

Monolithic Spatial Heterodyne Raman Spectrometer

The monolithic spatial heterodyne Raman spectrometer (mSHRS) is a fixed-grating heterodyne interferometer. The basic design and operation of the mSHRS has been discussed previously.[1–10,21–42] Collimated light entering the mSHRS is split into two beams by a 50:50 beam splitter, directed onto two tilted diffraction gratings and diffracted back along the same direction. The gratings are tilted at an angle, θ_L, such that a particular wavelength, the Littrow wavelength, λ_L, is retro-reflected and recombined so that no interference pattern is produced. For any wavelength other than Littrow, the recombined light produces a crossed wave front of which the crossing angle is wavenumber dependent and produces an interference pattern at the interferometer output. This output is imaged onto the detector, and the spectrum is revealed upon Fourier transform of the resulting fringe pattern. The interference pattern produced on the CCD is an image of vertical fringes with intensity as a function of detector position as shown in Eq. 3:

$$I(x) = \int_0^\infty B(\sigma)\{1 + \cos[8\pi(\sigma - \sigma_L)x \tan\theta_L]\}d\sigma \qquad 4.3$$

where B(σ) is the input spectral intensity at wavenumber σ, σ_L is the Littrow wavenumber, x is the position on the detector, and the other variables are defined above. The fringe frequency on the detector is given by Eq. 4:[19]

$$f = 4(\sigma\text{-}\sigma_L)\tan\theta_L \qquad 4.4$$

where f is in fringes/cm, σ_L is the Littrow wavenumber, σ is wavenumber of interest and θ_L is the Littrow angle. According to Eq. 2, emission lines above or below the Littrow wavelength may show identical fringe patterns, leading to degenerate lines (i.e., line overlap) for wavelengths equally above and below Littrow. It has been demonstrated before that this overlap can be removed by tilting vertically, or rotating one grating, causing the fringe pattern to be rotated on the CCD.[25] Thus, fringes rotate clockwise for bands below the Littrow wavenumber and rotate counterclockwise for bands above the Littrow wavenumber. In this paper we unambiguously resolve line overlap in a different way, by implementing the cross-dispersion technique (x_gmSHRS). Cross-dispersion eliminates degenerate lines by spatially separating out unique fringe patterns for each band into stacked rows in the vertical direction of the CCD, as shown in the FI inset of figure 4.2(b). The inset in Figure 4.2 shows the fringe image of both traditional mSHRS fringes 4.2(a) and cross-dispersion (x_gmSHRS) fringes 4.2(b) along with Raman spectra of the sulfur sample that was measured.

Figure 4.2 shows sulfur Raman spectra measured using the mSHRS spectrometer (a) and the x_gmSHRS spectrometer (b). In (a), the inset shows a series of vertical fringes in the CCD image, corresponding to the Raman bands of sulfur, both above and below Littrow. Since the Littrow wavenumber for this spectrometer is 321.9 cm^{-1}, the 219.1 cm^{-}

^{1} and 153.8 cm^{-1} bands are below Littrow, while the 473.2 cm^{-1} band is above Littrow. The 219.1 cm^{-1} band is well separated, but the 153.8 cm^{-1} and 473.2 cm^{-1} bands partially overlap in the spectrum, since they are similar distances from the Littrow wavenumber (168.1 and 151.3 cm^{-1}, respectively). In (b), the inset shows how the x_gmSHRS produces a unique fringe pattern for each Raman band, with the Raman shift increasing from bottom to top. The complete Raman spectrum is produced by selecting each row in the image, performing an FFT unambiguously and summing the result. Vertical dispersion in the x_gmSHRS removes the degeneracy of overlapping bands, as shown in the spectrum of Figure 2(b). The cross-dispersion technique has little effect on the spectral resolution. The measured band width for both sulfur spectra was ~6 cm^{-1}. For the 219.1 cm^{-1} band. However, removing the degeneracy of bands using the x_gmSHRS technique effectively doubles the spectral range. More importantly, the signal to noise ratio (SNR) increases in the x_gmSHRS spectrum, because vertical dispersion of the spectrum reduces contributions of shot noise from stronger Raman bands to weaker bands. The exact amount of the SNR increase depends on the relative band intensity, with weaker bands showing large improvements. This is discussed further with respect to Figure 5 below.

Figure 4.3 shows Raman spectra of cyclohexane measured (a) using the mSHRS and (b) using the x_gmSHRS. The resolution of both spectra is about 5 cm^{-1}. The two arrows point at the 1347 and 1444 cm^{-1} bands in the x_gmSHRS spectrum which don't appear in the mSHRS spectrum. Although these bands are outside of the calculated theoretical spectral range for the mSHRS, as stated above the resolving-power limited calculated value is just an estimate. The bands likely are resolved in the x_gmSHRS spectrum because of higher SNR in that spectrum and higher fringe visibility, FV (shown

in I insets: FV calculated using Eqn. 5 as 0.18 and 0.49 for mSHRS and x_gmSHRS, respectively) that results from the ability to optimize the fringe focus for the part of the image that contains weaker band fringes. Fringe visibility is a measure of fringe contrast and is reduced by out of band light that does not contribute to the interference fringes. For example, sample luminescence, or other types of broadband background light, which does not produce resolvable fringes, can reduced FV significantly and reduce the overall spectrum SNR. In a previous paper, we showed that this contribution to FV is greatly reduced by the x_gmSHRS, because broadband light is separated from Raman bands on the CCD.[11]

$$FV = (I_{max} - I_{min})/(I_{max}+I_{min}) \quad 4.5$$

Figure 4.4-4.7 shows Raman spectra of 4.4 isopropyl alcohol, 4.5 barite, 4.6 sodium sulfate, and 4.7 potassium perchlorate, measured using both the mSHRS (dotted line spectra) and the x_gmSHRS (solid line spectra), for comparison of the signal to noise ratio. The mSHRS and x_gmSHRS spectra for each sample are normalized to the highest intensity band. There was no difference in the resolution of the spectra with either spectrometer. The insets show fringe cross sections of the fringe images for the mSHRS spectra (grey lines) and x_gmSHRS spectra (black lines). Fringe cross sections for the x_gmSHRS were taken from the fringe image rows that corresponded to the strongest Raman band. In the case of mSHRS fringe images, the bands are not separated on the CCD, so all bands, resolved or unresolved, contribute to the fringe cross sections. Therefore the FV is much better in the x_gmSHRS spectra. The FV values were 0.19, 0.19, 0.17, and 0.24 using the mSHRS, and 0.46, 0.21, 0.27 and 0.30 using the x_gmSHRS for isopropyl alcohol, barite, sodium sulfate, and perchlorate, respectively.

In general, weaker Raman bands show the greatest improvement in fringe visibility and SNR using the x_gmSHRS, by reducing shot noise contributions from strong bands to the weaker features. An example of this is shown by the band inset (I_2) in Figure 4.4. The weak 430.2 cm^{-1} and 487.6 cm^{-1} isopropyl alcohol bands are clearly seen in the x_gmSHRS spectrum but are not discernible using the mSHRS.

Table 4.2 summarizes the SNR for the main bands of the four spectra in Figure 4.4-4.7, and also shows the SNR ratio improvements for spectra measured using the x_gmSHRS and mSHRS, ratio improvements. SNR was calculated by taking the band amplitude divided by standard deviation of the baseline. In the case of the x_gmSHRS spectra this was done for each band using the relevant rows of on the CCD.

The SNR improvements using the x_gmSHRS ranged from 1.0 (no improvement) to as large as 8.6. As expected, the SNR improvements were in general larger for weaker bands. Minimal or no SNR improvement was observed for strong sharp bands in samples that had only a few other weak bands. This is expected, since the strongest spectral feature would contribute the most shot noise to the total spectrum, so any shot noise improvement for this band would be minimal. The largest SNR improvement was for the very weak and broad bands of isopropanol, in the 400-500 cm^{-1} region. We also found larger SNR improvements all bands of this liquid sample than for the solid samples. This is attributed to better laser focus on the liquid sample (see FI insets in Figure 4.4 and 4.7), since this provides a better row separation of the vertical plane of the CCD in the cross-dispersion image than in the images of the solid samples, and to higher luminescence in the alcohol sample which is efficiently removed using the x_gmSHRS. A few of the sample's weaker bands do not show as large a SNR improvement as medium intensity

bands. This might be an effect of out-of-band light, whose removal by the x_gmSHRS has a large effect on SNR than the relatively less intense Raman bands.

Our first demonstration of the cross-dispersion technique with an SHRS used an Amici prism as the dispersive element, and a free standing SHRS (x_ASHRS).[11] The main differences between the prism based and the transmission grating-based spectrometers are, higher dispersion (~2x higher) more stable monolithic SHS with the transmission grating instrument. The x_gmSHRS transmission grating also had higher light transmission than the Amici prism, which was not anti-reflection coated. Cyclohexane spectra were used to compare the SNR improvement of the transmission grating (x_gmSHRS) and the Amici prism (x_ASHRS) cross-dispersion spectrometers. The overall SNR improvement of the grating-based spectrometer varied from 2x to as high as 132x for the weakest bands of cyclohexane. However, much of this improvement seems to be from the use of the monolithic SHS rather than the grating itself, as indicated by the mSHRS/SHRS SNR improvements of ~2-25, also shown in Table 4.3.

Sulfur Isotope Measurements using X_gmSHRS

The ^{34}S isotope is an important tracer for deep sea hydrothermal systems vent fluid and mineral deposit chemistry and has a natural abundance of about 4%.[19] It has been shown by multiple sulfur isotope studies many modern biologically mediated processes are characterized by mass-dependent fractionation that are different than equilibrium predictions. Temperature-dependent equilibrium isotopic exchange between sulfur-containing species also generates differences across sulfur isotope signatures, making it possible to distinguish between mixing and isotope exchange processes.[20,21] Raman is sensitive to isotope composition because different masses change the frequency

and intensity of Raman bands. The Raman ^{34}S band shows up as a prominent shoulder on the stronger ^{32}S band, as can be seen by comparing the natural abundance sulfur spectrum (Figure 4.8a solid line) with the pure ^{32}S, and pure ^{34}S spectra, shown in Figure 4.8a dashed line and Figure 4.8b, respectively. With the improvements of SNR and sensitivity that x_gmSHRS has over traditional mSHRS, weaker spectral features in Raman bands that are overlapped with stronger Raman bands can be detected with higher SNR. For example, x_gmSHRS can be used to measure isotopic shifts with greater sensitivity compared to other techniques. In Figure 4.8(a) representative spectra of sulfur of natural isotopic distribution (^{Nat}S) and pure sulfur-32 isotope (^{32}S) are shown.

These were measured with the x_gmSHRS. ^{Nat}S the (solid black line) is normalized to ^{32}S (dotted black line) to show the ^{34}S isotope shoulder which is indicated with an arrow. The pure ^{34}S isotope at 458.6 cm^{-1} in 4.8(b) shows the 15 cm^{-1} wavenumber shift of the highest intensity band that lines up with the shoulder of the ^{Nat}S sample. All sulfur measurements were made with an exposure time of 60 s, with a laser power of 30 mW and 7 mW for x_gmSHRS and mSHRS respectively. The reason for the difference in laser power is because the signal reaching the detector in the x_gmSHRS system shown in Figure 4.1 decreases by ~2x compared to the mSHRS system. The difference in laser power helped equalize the signal intensity obtained on these two systems. Since there would be ambiguity with the 473.2 cm^{-1} sulfur Raman band due to the mSHRS fold over effects explained with Figure 2, a bandpass filter was implemented to block the 153.8 cm^{-1} and the 219.1 cm^{-1} Raman bands for comparison.

The SNR of the x_gmSHRS had ~2x improvement over the mSHRS and the microRaman. These values are shown in Table 4.4. These isotopic bands could be further

extracted by using a x_gmSHRS with higher linear dispersion. The x_gmSHRS has overall higher sensitivity and SNR than the mSHRS which leads to better detection of weak spectral features.

4.5 Conclusion

In this chapter, we described the use of a transmission grating paired with a monolithic SHRS (mSHRS), to demonstrate that the crossed-dispersed method facilitates the measurement of weak Raman spectral features in various Raman reference samples that, in a traditional mSHRS, would be overpowered by multiplicative photon noise. The x_gmSHRS showed overall improvement in SNR compared to the traditional mSHRS and the Amici prism x_ASHRS. This method demonstrated measurements of sulfur isotopes with improved SNRs of weak spectral features that are overlapped with strong spectral features. Cross-dispersed mSHRS could allow the analysis of isotopes of other elements in the environment. This technique could be further improved by incorporating a transmission grating with higher grating groove density, and by using the same focal length cylindrical lens as in the current configuration, the linear dispersion of the system can be increased without needing to increase the overall size of the optical setup and spectrometer.

4.6 References

1. J.M. Harlander. Spatial Heterodyne Spectroscopy: Interferometric Performance at Any Wavelength Without Scanning. [Ph.D. Dissertation]. Madison, WI: University of Wisconsin–Madison, 1991.

2. J.M. Harlander, F.L. Roesler, R.J. Reynolds, et al. ‘‘Differential, Field-Widened Spatial Heterodyne Spectrometer for Investigations at High Spectral Resolution of the Diffuse Far Ultraviolet 1548 A° Emission Line from the Interstellar Medium’’. Proc. SPIE. 1993. 2006: 139–148.
3. P.C.D. Hobbs. “Building Electro-Optical Systems: Making It All Work”. Hoboken, NJ: John Wiley and Sons, 2009. 240–242.
4. N. R. Gomer, C.M Gordon, P. Lucey, S.K. Sharma, J.C. Carter, S.M. Angel, “Raman Spectroscopy Using a Spatial Heterodyne Spectrometer: Proof of Concept”. Applied Spectroscopy. 2011. (65): 849-857.
5. N. Lamsal, S.K. Sharma, T.E. Acosta, et al. ‘‘Stand-off UV and Visible Raman Measurements Using a Gated Spatial Heterodyne Raman Spectrometer’’. Applied Spectroscopy. 2016. 70(4): 666–685.
6. N. Lamsal, S.M. Angel. ‘‘Deep-Ultraviolet Raman Measurements Using a Spatial Heterodyne Raman Spectrometer (SHRS)’’. Applied Spectroscopy. 2015. 69(5): 525–534.
7. N. Lamsal, S.M. Angel, S.K. Sharma, et al. ‘‘Visible and UV Stand Off Raman Measurements in Ambient Light Conditions Using a Gated Spatial Heterodyne Raman Spectrometer’’. Paper 1459, presented at: LPSC 2015. Woodland, TX; March 16–20, 2015.
8. P.D. Barnett, N. Lamsal, S.M. Angel. ‘‘Standoff Laser-Induced Breakdown Spectroscopy (LIBS) Using a Miniature Wide Field of View Spatial Heterodyne Spectrometer with Sub-Microsteradian Collection Optics’’. Applied Spectroscopy. 2017. 71(4): 585–590.

9. I.B. Gornushkin, B.W. Smith, U. Panne, et al. ‘‘Laser-Induced Breakdown Spectroscopy Combined with Spatial Heterodyne Spectroscopy’’. Applied Spectroscopy. 2014. 68(9): 1076–1084.
10. A.N. Allen, A.M. Waldron, J.M. Ottaway, et al. ‘‘Hyperspectral Raman Imaging Using a Spatial Heterodyne Raman Spectrometer with a Microlens Array’’. Applied Spectroscopy. 2020. 74(8): 921-931.
11. M.J. Egan, A. Colón, S.M. Angel, S.K. Sharma. “Suppressing the Multiplex Disadvantage in Photon-Noise Limited Interferometry Using Cross-Dispersed Spatial Heterodyne Spectrometry”. Applied Spectroscopy. 2021. 75(2).
12. Y. Maruyama, J. Blacksberg, E. Charbon. ‘‘A 1024_8, 700 ps Time- Gated SPAD Line Sensor for Planetary Surface Exploration with Laser Raman Spectroscopy and LIBS’’. IEEE J. Solid-State Circuits. 2014. 49(1): 179–189.
13. J.M. Harlander, F.L. Roesler, J.G. Cardon, C.R. Englert, R.R. Conway. ‘‘SHIMMER: A Spatial Heterodyne Spectrometer for Remote Sensing of Earth’s Middle Atmosphere’’. Applied Optics 2002. 41(7): 1343–1352.
14. A.I. Sheinis, E. Mierkiewicz, F. Roesler, J. Harlander, A. Bodkin. ‘‘A Spatial Heterodyne Spectrometer for Diffuse H-a Spectroscopy’’. Proc. SPIE. 2008. 7014: 70140I-1–70140I-12.
15. V. Sweedler, R.D. Jalkian, G.R. Sims, M.B. Denton. ‘‘Crossed Interferometric Dispersive Spectroscopy’’. Applied Spectroscopy. 1990. 44(1): 14–20.
16. A. Waldron, A. Allen, A. Colón, J.C. Carter, S.M. Angel. “A Monolithic Spatial Heterodyne Raman Spectrometer: Initial Tests”. Applied Spectroscopy. 2021. 75(1): 57-69.

17. A.K. Strange Fessler, A. Waldron, A. Colón, C.J. Carter, S. Michael Angel, “A demonstration of spatial heterodyne spectrometers for remote LIBS, Raman spectroscopy, and 1D imaging”. Spectrochimica Acta Part B. 2021. 178.
18. E.M. Kelly, M.J. Egan, A. Colón, S.M. Angel, S.K. Sharma. “Remote Raman Sensing using a Single-Grating Monolithic Spatial Heterodyne Raman Spectrometer—A Potential Tool for Planetary Exploration” Applied. Spectroscopy. In press 2022.
19. X. Wu, Y. Tan, Y. Yi, et al. ‘‘Two–dimensional Spatial Heterodyne Spectrometer for Atmospheric Nitrogen Dioxide Observations’’. Optics Express. 2019. 27(15): 20942–20957.
20. Y. Yi, S. Zhang, F. Liu, et al. ‘‘Laboratory Fabrication of Monolithic Interferometers for One and Two–Dimensional Spatial Heterodyne Spectrometers’’. Optics Express. 2017. 25(23): 29121–29134.
21. P. Barnett, S.M. Angel. ‘‘Miniature Spatial Heterodyne Raman Spectrometer with a Cell Phone Camera Detector’’. Applied. Spectroscopy. 2016. 71(5): 988–995.
22. K.A. Strange, K.C. Paul, S.M. Angel. ‘‘Transmission Raman Measurements Using a Spatial Heterodyne Raman Spectrometer (SHRS)’’. Applied. Spectroscopy. 2017. 71(2): 250–257.
23. A.N. Allen, S.M. Angel. ‘‘Miniature Spatial Heterodyne Spectrometer for Laser Induced Breakdown Spectroscopy and Raman Spectroscopy Using Fresnel Collection Optics’’. Spectrochimca Acta, Part B. 2018. 149: 91–98.

24. P.D. Barnett, K.A. Strange, S.M. Angel. ‘‘Improving Spectral Results Using Row-by-Row Fourier Transform of Spatial Heterodyne Raman Spectrometer Interferogram’’. Applied Spectroscopy. 2017. 71(6): 1380–1386.

25. J.M. Ottaway, A.N. Allen, A.M. Waldron, et al. ‘‘Spatial Heterodyne Raman Spectrometer (SHRS) for In Situ Chemical Sensing Using Sapphire and Silica Optical Fiber Raman Probes’’. Applied Spectroscopy. 2019. 73(10): 1160–1171.

26. J. Liu, Bayanheshig, X. Qi, et al. ‘‘Backscattering Raman Spectroscopy Using Multi-Grating Spatial Heterodyne Raman Spectrometer’’. Applied Optices. 2018. 57(33): 9735–9745.

27. J. Qiu, X. Qi, X. Li, et al. ‘‘Raman Measurements Using a Field– Widened Spatial Heterodyne Raman Spectrometer’’. Journal of Raman Spectroscopy. 2019. 50: 1602–1613.

28. M.J. Egan, S.M. Angel, S.K. Sharma. ‘‘Standoff Spatial Heterodyne Raman Spectrometer for Mineralogical Analysis’’. Journal of Raman Spectroscopy. 2017. 48: 1613–1617.

29. M.J. Egan, S.M. Angel, S.K. Sharma. ‘‘Optimizing Data Reduction Procedures in Spatial Heterodyne Raman Spectroscopy with Applications to Planetary Surface Analogs’’. Applied Spectroscopy. 2018. 72(6): 933–942.

30. G. Hu, W. Xiong, H. Shi, et al. ‘‘Raman Spectroscopy Detection for Liquid and Solid Targets Using a Spatial Heterodyne Spectrometer’’. Journal of Raman Spectroscopy. 2016. 47: 289–298.

31. J. Qui, X. Qi, X. Li, et al. ‘‘Broadband transmission Raman Measurements Using a Field Widened Spatial Heterodyne Raman Spectrometer with Mosaic Grating Structure’’. Optics Express. 2018. 26(20): 26106–26119.

32. J. Qiu, X. Qi, X. Li, et al. ‘‘Broadband, High-Resolution Raman Observations from a Double–Echelle Spatial Heterodyne Raman Spectrometer’’. Applied Optics. 2018. 57(30): 8936–8941.

33. J. Qiu, X. Qi, X. Li, et al. ‘‘Development of a Spatial Heterodyne Raman Spectrometer with Echelle–Mirror Structure’’. Optics Express. 2018. 26(9): 11994–12006.

34. G. Hu, W. Xiong, H. Luo, et al. ‘‘Research of Spatial Heterodyne Raman Spectroscopy with Standoff Detection’’. Spectroscopy and Spectral Analysis. 36(12): 3951-3957.

35. G. Hu, W. Xiong, H. Luo, et al. ‘‘Raman Spectroscopic Detection for Simulants of Chemical Warfare Agents Using a Spatial Heterodyne Spectrometer’’. Applied Spectroscopy. 2018. 72(1): 151–158.

36. G. Hu, W. Xiong, H. Luo, et al. ‘‘Spectral Restoration Method for Spatial Heterodyne Raman Spectrometer’’. Journal of Raman Spectroscopy. 2017. 48: 1633–1643.

37. E.A. McCormack, A.H. Mortimer, L. Ciaffoni. ‘‘Compact Spatial Heterodyne Static Interferometer’’. Applied Optics. 2020. 59: 4271–4278.

38. M.J. Foster, J. Storey, M.A. Zentile. ‘‘Spatial Heterodyne Spectrometer for Transmission Raman Observations’’. Optics Express. 2016. 25(2): 1598–1604.

39. J.M. Harlander, F.L. Roesler, S. Chakrabarti. ‘‘Spatial Heterodyne Spectroscopy: A Novel Interferometric Technique for the FUV’’. Proc. SPIE. 1990. 1344: 120–131.

40. P. Barnett. The Development of a Miniature Spatial Heterodyne Raman Spectrometer for Applications in Planetary Exploration and Other Extreme Environments. [Ph.D. Dissertation]. Columbia, SC: University of South Carolina-Columbia, 2016.

41. McDermontt, J.M., Ono, S., Tivey, M.K., Seewald, J.S., Shanks, W.C.III, Solow, A.R., “Identification of sulfur isotopic equilibria in submarine hot-springs using multiple sulfur isotopes” Geochimica et Cosmochimica Acta. 2015. 160: 169-187.

42. Tomaso R. R., Bontognalia, Alex L. Sessionsa, Abigail C. Allwoodb, Woodward W. Fischera, John P. Grotzingera, Roger E. Summonsc, and John M. Eilera, “Sulfur isotopes of organic matter preserved in 3.45-billion-year-old stromatolites reveal microbial metabolism” Geological and Planetary Sciences. 2012. 109.

43. Sessions, A.L., Doughty, D.M., Welander, P.V., Summons, R.E., Newman, D.K., “The Continuing Puzzle of the Great Oxidation Event,” Current Biology. 2009. 19: R567-R574.

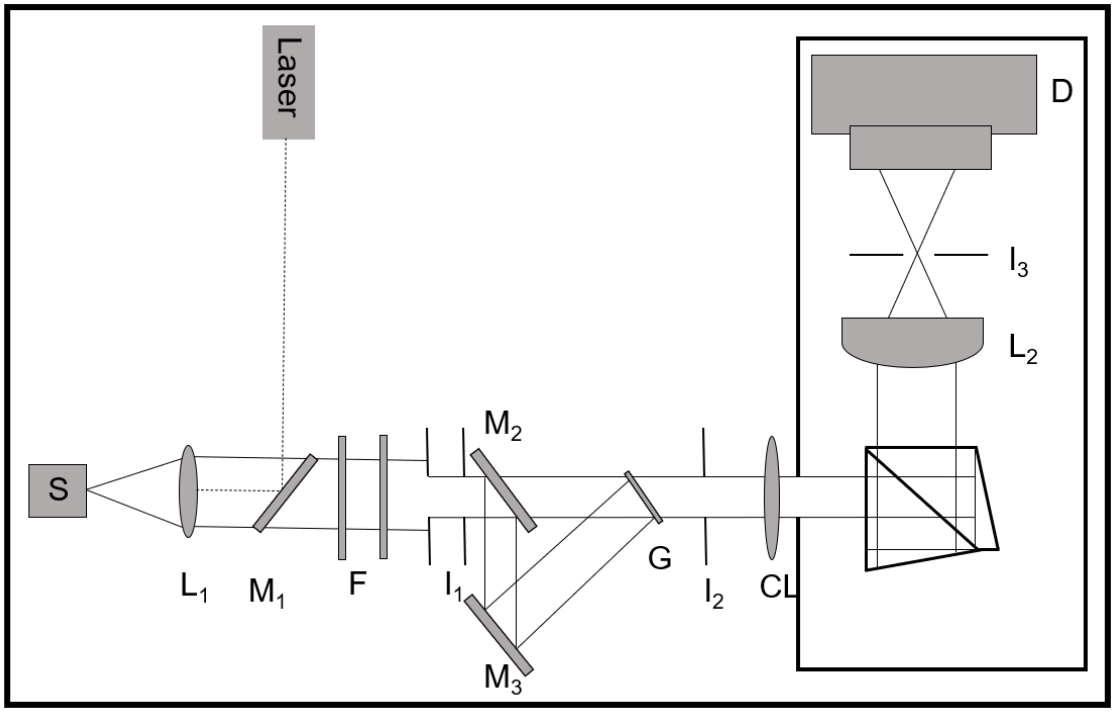

Figure 4.1 Schematic diagram of the x_gmSHRS system. S: sample; L_1: collection lens; M_1: dichroic mirror; F: filters, I_1 and I_2: iris, M_2 and M_3: aluminum mirrors, G: transmission grating, CL: cylindrical lens, L_2: imaging lens, I_3: spatial filter; D: CCD detector.

Specs	Amici Prism[11]	Transmission Grating
Linear Dispersion	37.7 nm/mm	77.5 nm/mm
Angular Dispersion	0.02 deg/nm	0.08 deg/nm
AR coated	None	Fused silica high power dielectric coated
Transmission efficiency	0.78 at 532 nm	0.82 at 532 nm
Littrow wavelength	532 nm	541.27 nm
Spot size	8 mm	10 mm
SHS	Free standing	Monolithic
Groove density of SHS grating	150 grooves/mm	600 grooves/mm
Resolving Power	2116	12000
Spectral Range	2102.50 cm^{-1}	1351.38 cm^{-1}
Magnification	0.9	1.7
Cylindrical lens focal	75 mm circular lens	100 mm circular achromat lens
CCD	Pixis BUV	Pixis BUV

Table 4.1: Comparison of Amici prism and transmission grating specs and set up are shown. The improvements of x_gmSHRS over the x_ASHRS are described.

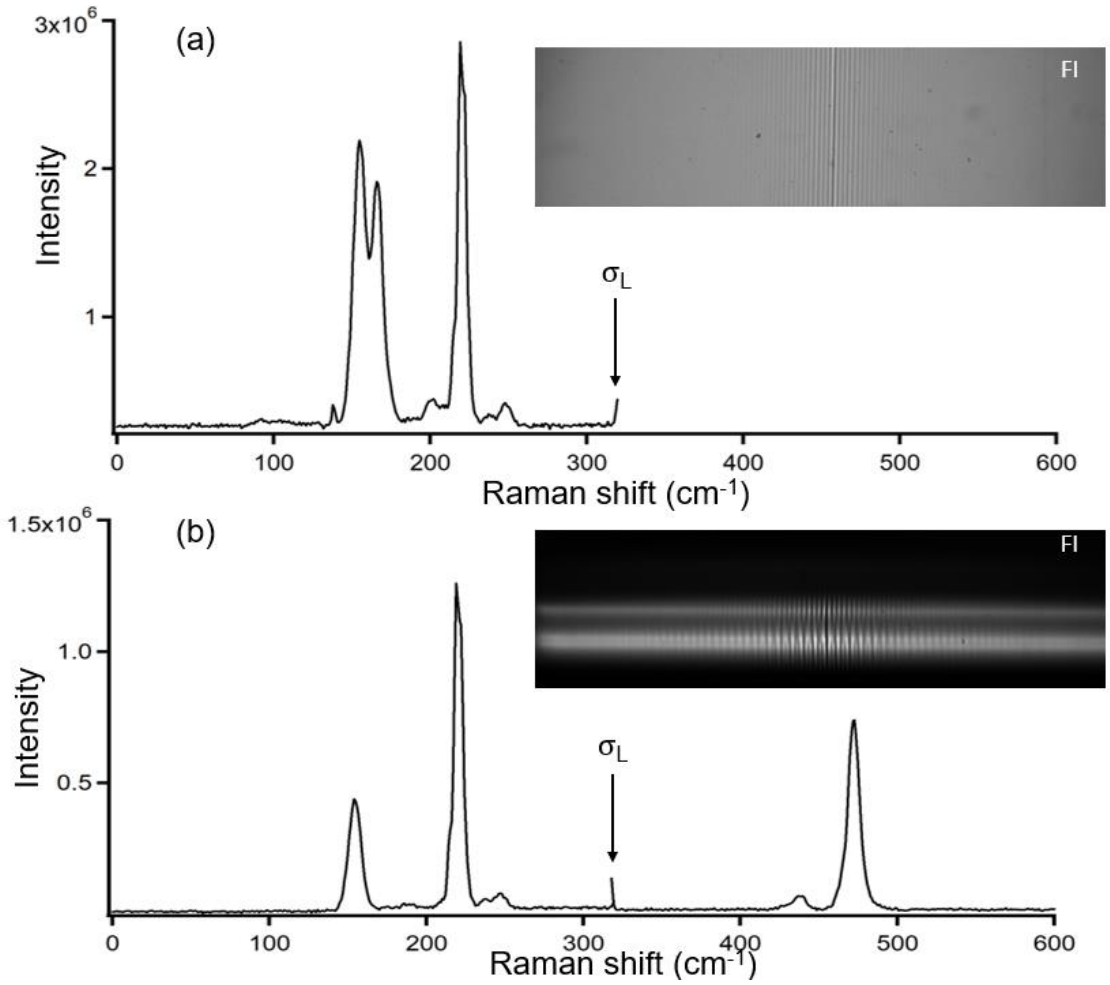

Figure 4.2 Raman spectra of sulfur are measured with the same mSHRS using traditional mSHS technique, 2(a), and using cross dispersion technique (x_gmSHRS), 2(b). The fringe image inserts (FI) are the fringe images of both the traditional mSHRS fringes 2(a) and the cross-dispersion fringes 2(b). For x_gmSHRS, the Raman shift increases as one scans the image from bottom to top. Figure 4.2(a) shows the 473.2 cm^{-1} band overlapping with the 153.8 cm^{-1} sulfur band since the 473.2 cm^{-1} sulfur band would fold over at 151.3 cm^{-1} for traditional mSHRS measurements. With the x_gmSHRS each sulfur band can be separated into its own unique fringe pattern and thus each band can be selected and FFT unambiguously as shown in spectrum 2(b). The two arrows in the spectra point at where the Littrow wavenumber, (σ_L), is located. These measurements were made with a 60 s exposure time.

.

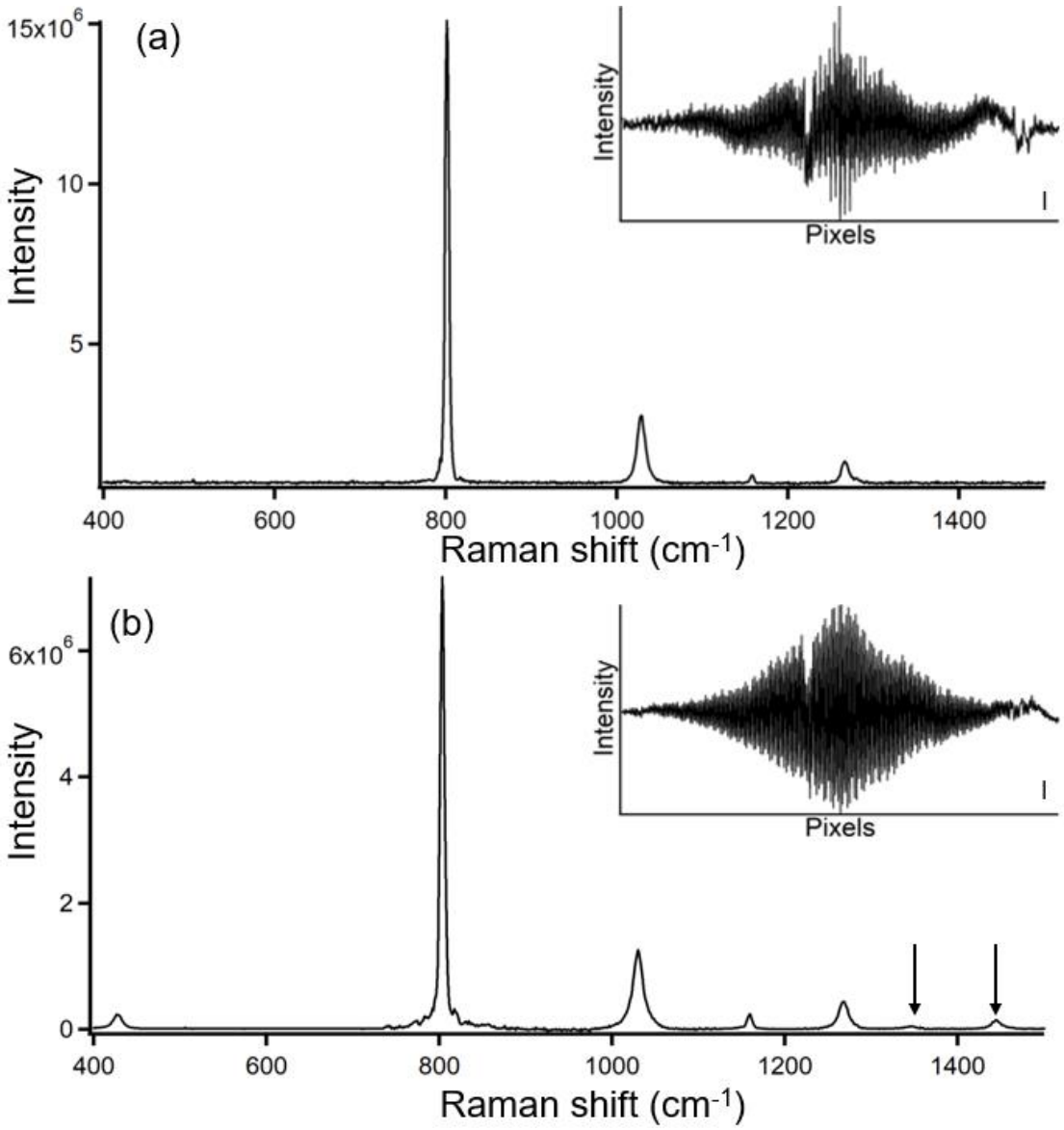

Figure 4.3 Two cyclohexane Raman spectra are shown. Spectrum (a) is measured using traditional mSHRS and spectrum (b) is measured using x_gmSHRS. The two arrows on spectrum (b) point at the 1347 and 1444 cm^{-1} bands. The interferogram cross sections (inset I) for each spectrum are generated by summing the intensity of each column of pixels in the fringe image (inset FI) and applying background subtraction. For x_gmSHRS this would be done using the number of rows in the selected region. Cyclohexane had an exposure time of 60s.The fringe visibility, FV, was 0.18 for (a) and 0.49 for (b).

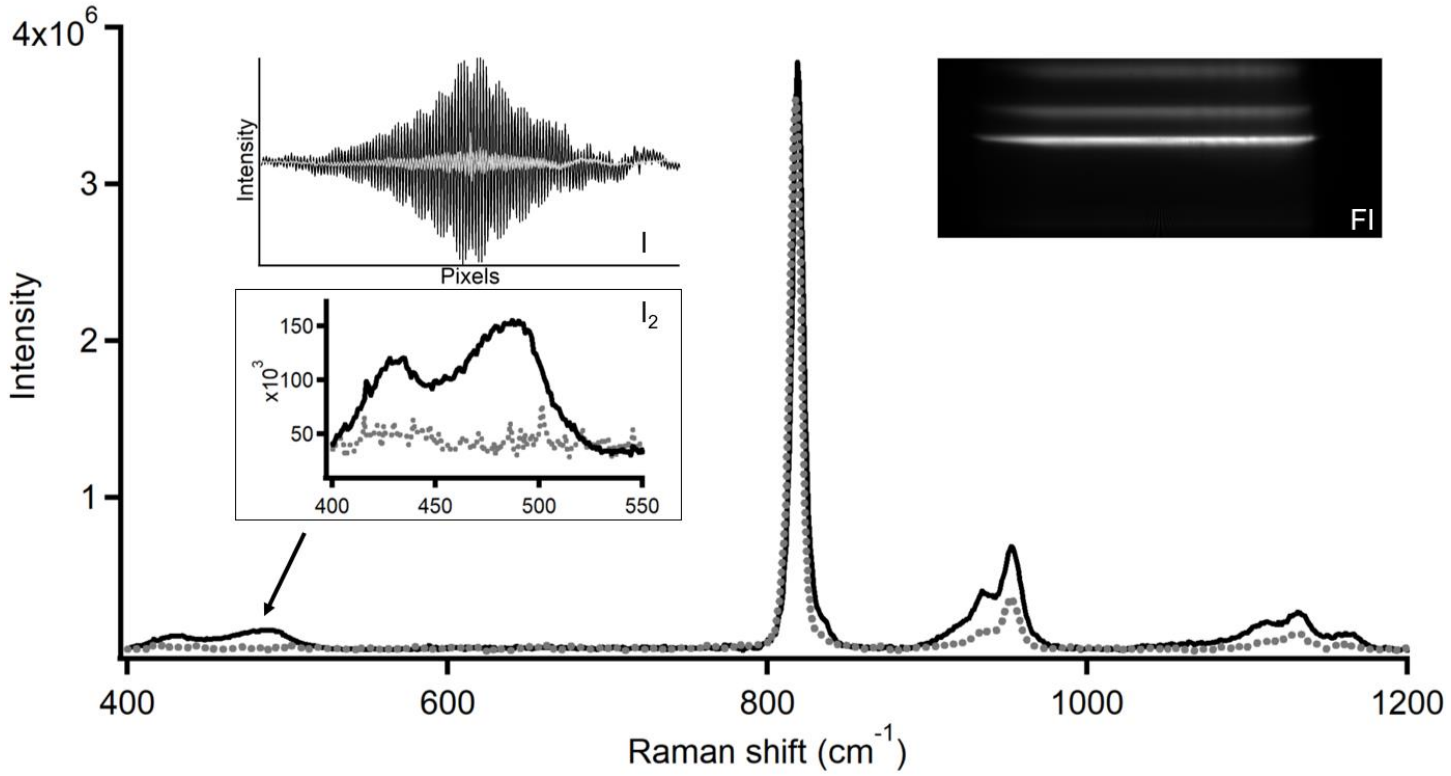

Figure 4.4 Raman spectra of isopropyl alcohol comparing the mSHRS with the x_gmSHRS. The most intense band of the mSHRS measurements was normalized to the most intense band of the x_gmSHRS spectra. The dotted lines are the mSHRS measurements and the solid lines are the x_gmSHRS measurements. The inset I are the cross sections of mSHRS measurements in grey overlapped with the cross sections of the x_gmSHRS measurements in black. The inset FI are the cross-dispersion fringe images for each sample. The FV is 0.19 with traditional mSHRS and 0.46 with x_gmSHRS for isopropyl alcohol, barite, sodium sulfate, and perchlorate respectively. The inset, I_2, in spectrum (a) is zoomed into the 430.2 cm^{-1} and 487.6 cm^{-1} isopropyl alcohol Raman bands that are not detected using the mSHRS technique but are detected when using the x_gmSHRS technique. All spectra were 60s exposures.

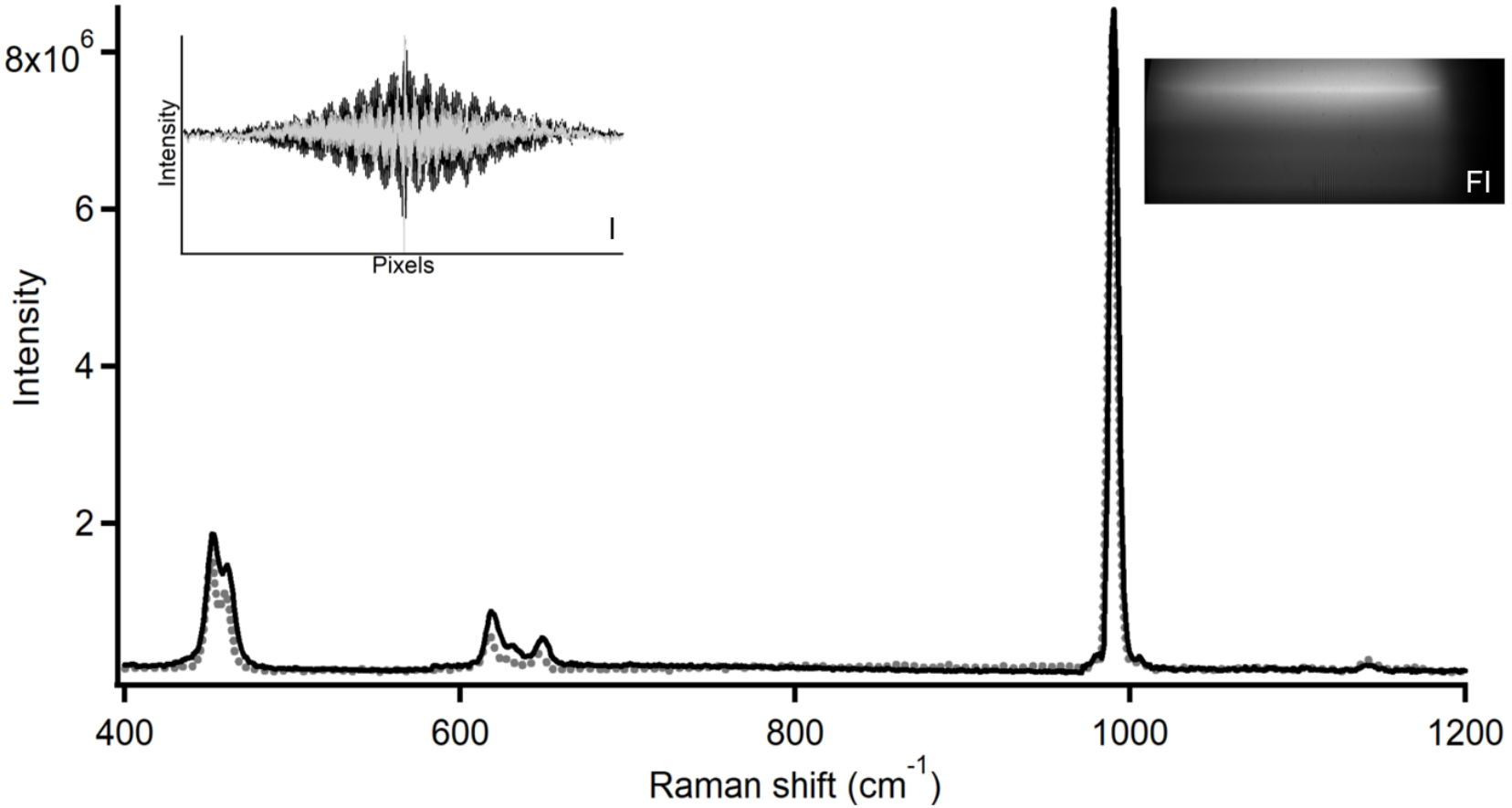

Figure 4.5 Raman spectra of barite comparing the mSHRS with the x_gmSHRS. The most intense band of the mSHRS measurements was normalized to the most intense band of the x_gmSHRS spectra. The dotted lines are the mSHRS measurements and the solid lines are the x_gmSHRS measurements. The inset I are the cross sections of mSHRS measurements in grey overlapped with the cross sections of the x_gmSHRS measurements in black. The inset FI are the cross-dispersion fringe images for each sample. The FV is 0.19 with traditional mSHRS and 0.21 with x_gmSHRS for isopropyl alcohol, barite, sodium sulfate, and perchlorate respectively. All spectra were 60s exposures.

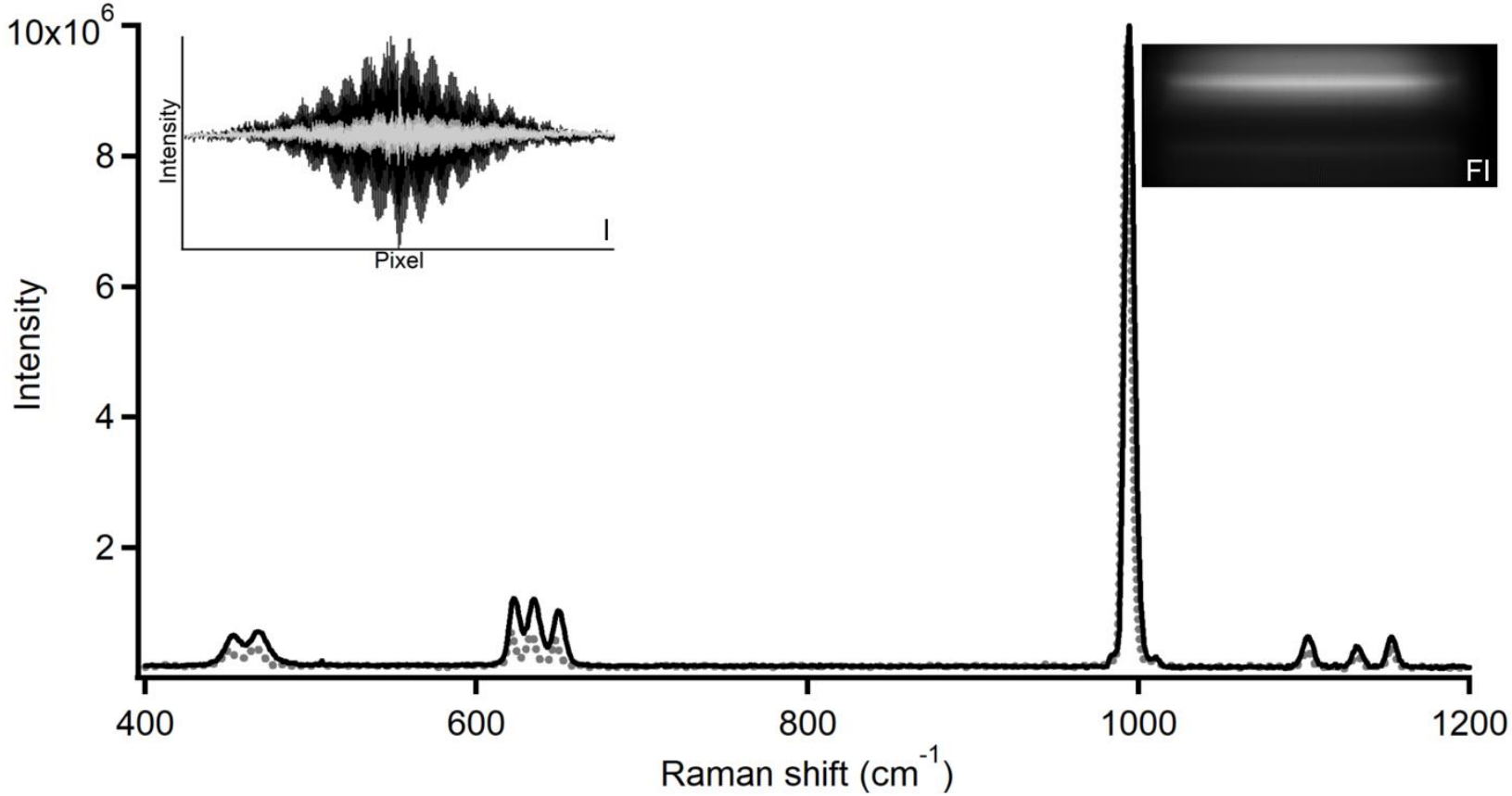

Figure 4.6 Raman spectra of sodium sulfate comparing the mSHRS with the x_gmSHRS. The most intense band of the mSHRS measurements were normalized to the most intense band of the x_gmSHRS spectra. The dotted lines are the mSHRS measurements and the solid lines are the x_gmSHRS measurements. The inset I are the cross sections of mSHRS measurements in grey overlapped with the cross sections of the x_gmSHRS measurements in black. The inset FI are the cross-dispersion fringe images for each sample. The FV is 0.17 with traditional mSHRS and 0.27 with x_gmSHRS for isopropyl alcohol, barite, sodium sulfate, and potassium perchlorate respectively. The inset, All spectra were 60s exposures.

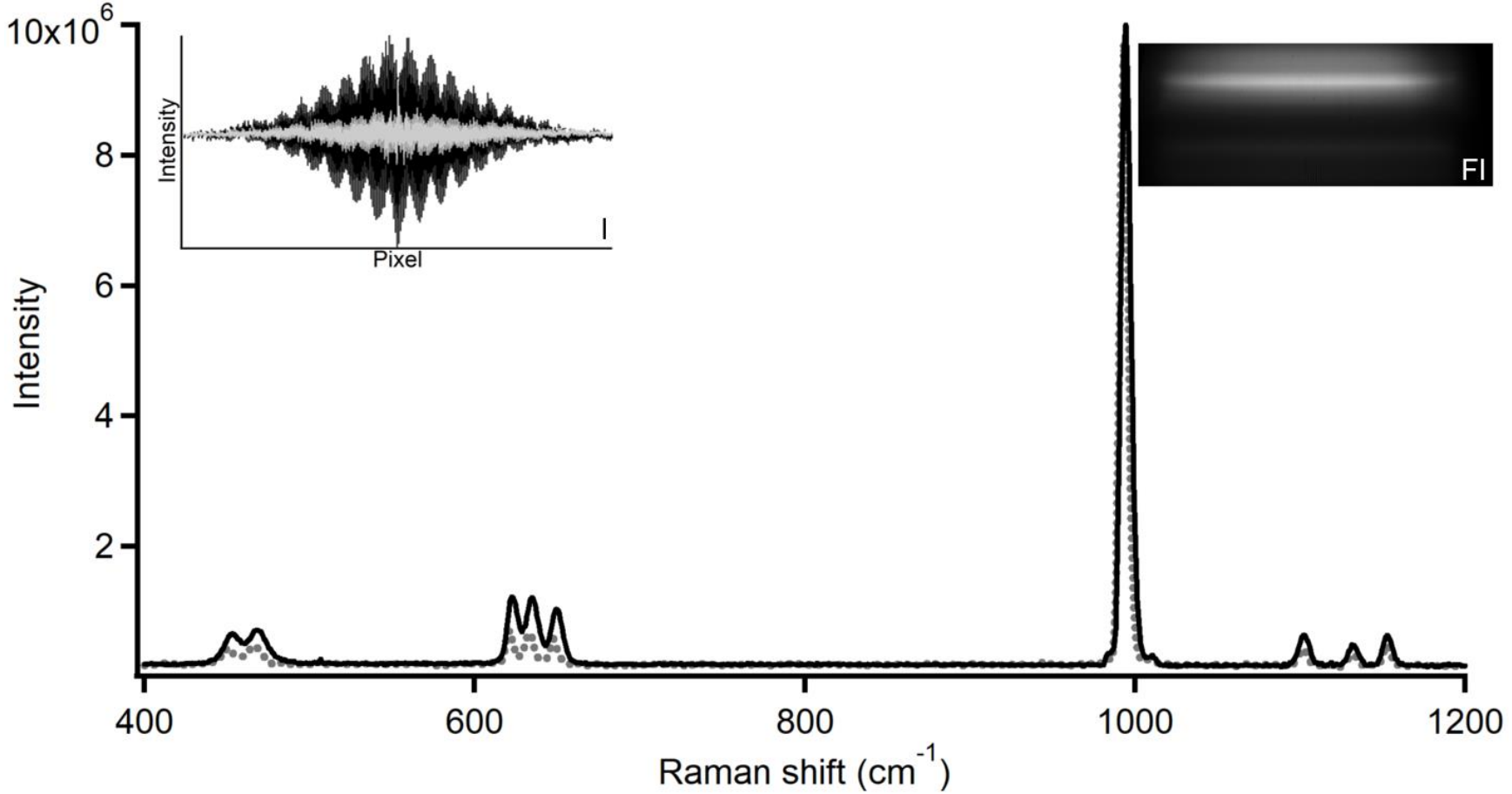

Figure 4.7 Raman spectra of potassium perchlorate comparing the mSHRS with the x_gmSHRS. The most intense band of the mSHRS measurements was normalized to the most intense band of the x_gmSHRS spectra. The dotted lines are the mSHRS measurements and the solid lines are the x_gmSHRS measurements. The inset I are the cross sections of mSHRS measurements in grey overlapped with the cross sections of the x_gmSHRS measurements in black. The inset FI are the cross-dispersion fringe images for each sample. The FV is 0.24 with traditional mSHRS and 0.30 with x_gmSHRS for isopropyl alcohol, barite, sodium sulfate, and perchlorate respectively. The inset, All spectra were 60s exposures.

Table 4.2: Signal to noise ratio (SNR) comparisons of mSHRS and x_gmSHRS SNR are shown along with relative band intensity ratios and x_gmSHRS/mSHRS ratio improvements. For x_gmSHRS, each row on the CCD cross-dispersed image was selected and an FFT was applied to produce the individual band and the SNR was calculated by dividing the band amplitude by the baseline of the individual noise floor cross-dispersed row.

$KClO_4$ Raman bands (cm^{-1})	Predicted SNR for mSHRS	mSHRS SNR	Predicted SNR for x_gmSHRS	x_gmSHRS SNR	Predicted SNR Improvements x_gmSHRS/mSHRS	SNR Improvements x_gmSHRS/mSHRS
461	1390	420	2120	930	1.5	2.2
631	655	198	1592	423	2.4	2.1
942	3593	1085	3426	1068	1.0	1.0
1086	86	26	554	35	6.4	1.3
1102	96	29	574	38	6.0	1.3
Na_2SO_4 Raman bands (cm^{-1})						
450	86	20	635	57	7.4	2.9
621	193	44	1106	173	5.7	3.9
993	3549	818	3132	824	0.9	1.1
1102	94	22	679	38	7.2	1.7
1132	67	15	567	26	8.5	1.7
1153	119	27	678	37	5.7	1.4
Barite Raman bands (cm^{-1})						
452	607	99	1258	300	2.6	3.1
616	186	30	806	85	4.3	2.8
987	3545	575	29001	670	0.8	1.2
Isopropyl alcohol Raman bands (cm^{-1})						
431	-	-	350	57	-	-
818	2597	366	1931	413	0.7	1.1
952	244	34	810	157	3.3	4.6
1114	36	5	421	43	11.8	8.6
1132	68	10	488	58	7.2	6.1
1164	22	3	324	26	14.4	8.1

Table 4.3 SNR comparisons of Amici prism and dispersion grating for cyclohexane.

	Transmission Grating		Amici Prism[11]			
Cyclohexane Raman shift (cm^{-1})	SNR for mSHRS	SNR for x_gmSHRS	SNR for SHRS	SNR for x_ASHRS	SNR Improvements mSHRS/SHRS	SNR Improvements x_gmSHRS/x_ASHRS
426	-	2772.3	-	21.0	-	132.0
801	846.9	481.1	34.2	28.2	24.8	17.1
1028	123.3	202.6	30.6	31.3	4.0	6.5
1157	13.9	103.0	-	14.9	-	6.9
1266	39.0	97.7	20.7	25.5	1.9	3.8
1347	-	30.4	-	8.3	-	3.7
1444	-	54.3	20.5	26.9	-	2.0

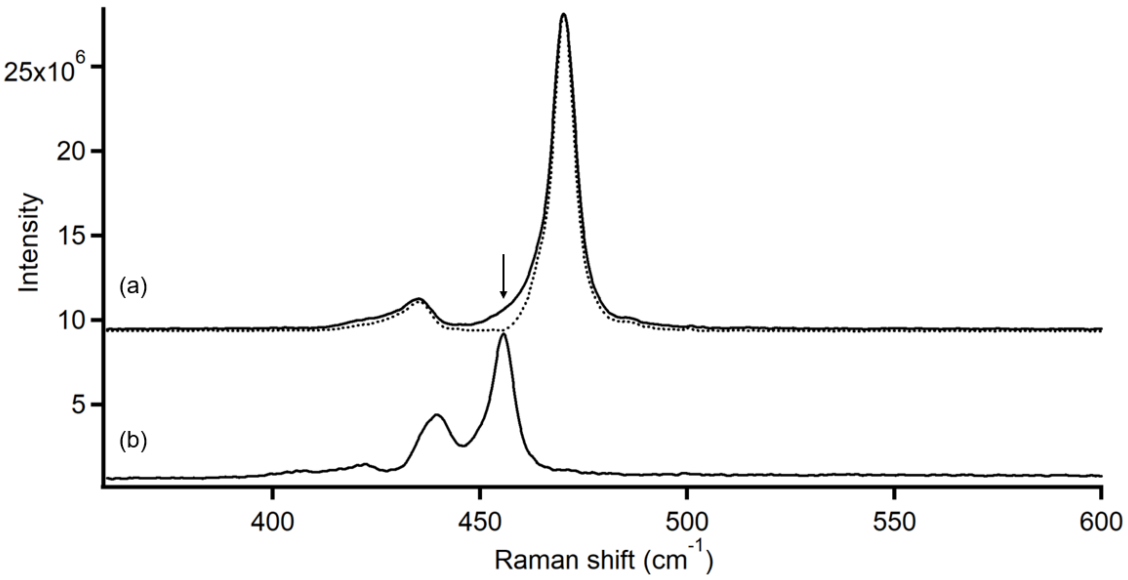

Figure 4.8 Representative spectra measured with the x_gmSHRS (a) natural sulfur (^{Nat}S), ^{32}S, and (b)^{34}S. In (a) the (^{Nat}S) (solid line) is normalized to ^{32}S (dotted line) to show the ^{34}S isotope position which is indicated with an arrow.

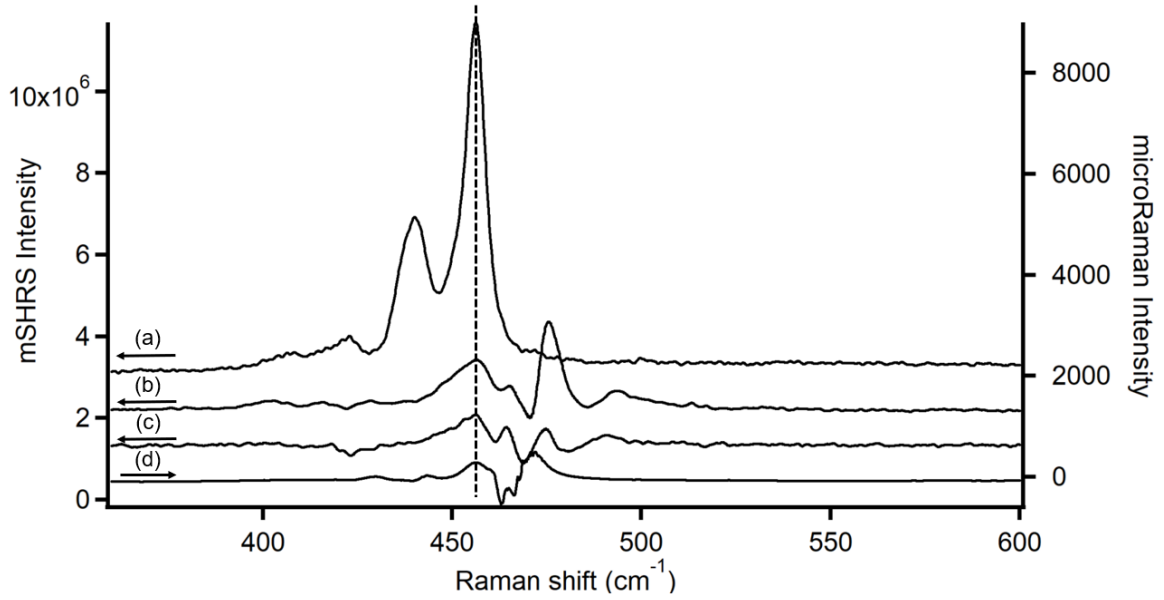

Figure 4.9 Representative x_gmSHRS spectrum of (a) pure ^{34}S and subtracted ^{34}S spectra with x_gmSHRS, (b) x_gmSHRS, (c) mSHRS, and (d) microRaman. For microRaman measurements were made with 60s exposures.

Table 4.4: Sulfur isotope comparison of mSHRS and microRaman spectroscopy versus x_gmSHRS SNR shows a greater improvement in SNR for ^{34}S isotope that is overlapped with ^{Nat}S. The SNR of the x_gmSHRS had ~2x improvement over the mSHRS and the microRaman

^{34}S Raman bands (cm^{-1})	mSHRS SNR	x_gmSHRS SNR	microRaman SNR	SNR Improvements x_gmSHRS/mSHRS	SNR Improvements x_gmSHRS/microRaman
458	37	77	51	2.1	1.5

CHAPTER 5

INITIAL CHARACTERIZATION OF A HALF INCH MONOLITHIC SPATIAL HETERODYNE RAMAN SPECTROMETER

5.1 Introduction

Raman is ideally suited for oceanographic measurements in that it can be used for gases, liquids and solids, providing a molecular fingerprint and is good for complex multi-component samples and determining crystal phase. Raman spectra can also be used to identify organic and inorganic chemical compounds and minerals based on the vibrational frequencies, relative intensities, and number of bands in the spectra with little to no sample preparation.[1-6] Great progress has been made in the development of instrument platforms and sampling systems necessary to support Raman spectroscopy for oceanographic applications and there are many interest that Raman spectroscopy could aid in.[7-17] Those interests include the mineralogy of the sea floor and the chemistry of pore water, gas seeps, and sea floor vents. Also, the need to monitor gas vents for species such as CH_4, CO_2, CO, H_2S, and H_2 and to distinguish speciation that are sensitive to oxygen concentration (e.g., CH_4 vs. CO_2, sulfate vs. sulfide) and pH (e.g., HCO_3^{2-} vs. CO_3^{2-}) and to make time and spatially resolved measurements of the ocean chemistry, e.g., investigate gradients in dissolved gases, such as CO_2, and dissolved aqueous complexes, such as sulfate and carbonate. The concentrations of such species typically are homogeneous and unchanging in the deep ocean.[14] When there are compositional

variations and concentration gradients, however, such as may exist around a hydrothermal vent, they are often transient. There is a need for a technique that could quickly recover in situ, such as Raman spectroscopy, that does not disturb the compositional distribution.[14] Advancement in field deployed Raman spectrometers must overcome a number of limitations to current systems, such as: low sensitivity and probe depth of field, large size and weight; complex procedures for alignment, calibration, laser focusing, and sample positioning; high power usage; and, above all, fragile optics. The sensitivity is also often a disadvantage, requiring improvement for detecting more trace components. To solve these problems, a compact deep-sea in situ Raman spectroscopy system is needed.[17] The Spatial Heterodyne Raman Spectrometer (SHRS) was first developed by Dohi et al. in 1970,[18] and later adapted by Harlander et al. in 1991.[19] The instrumental design is based on the Michaelson interferometer but instead of two mirrors it has two stationary gratings. Since the SHRS is not slit dependent like conventional grating spectrometers, it provides high spectral resolution and spectral range in a very small footprint. The SHRS was first used for Raman applications in 2011 by Gomer et al.[21] and later developed for UV Raman[22,23] remote Raman[22,24] laser-induced breakdown spectroscopy[25,26] and for hyperspectral Raman imaging.[27] One of the advantages of the SHRS design for Raman spectroscopy is its wide field of view. Lamsal et al., showed that the wide field of view can be used to minimize sample degradation in deep-UV Raman measurements by using a defocused laser.[22,23] In the case of remote Raman, the wide acceptance angle and large aperture makes the SHRS relatively easy to couple with telescopic optics and minimizes laser pointing stability issues, because small movements of the laser spot on the target do not reduce the amount of light collected by the

spectrometer aperture, unlike the case of a dispersive spectrometer where the output of the telescope has to be held in focus on a narrow input slit.[24,27]

The monolithic Spatial Heterodyne Spectrometer (mSHRS) design allows for the spectrometer to be extremely small because the spectral resolution is not a strong function of device size and been proven to be a robust Raman spectrometer, immune to shock and vibrations, with increased sensitivity at a size and weight orders of magnitude smaller than current oceanographic Raman instruments. [28-30]

5.2 Experimental

Monolithic Spatial Heterodyne Raman Spectrometer (mSHRS)

The half-inch mSHRS described here was custom-built by LightMachinery, Inc. (Canada). The interferometer consists of two 9 mm x 9 mm diffraction gratings, a 12.5 mm N-BK7 50:50 cube beam splitter, and two N-BK7 spacers that define the angle the gratings are tilted in the horizontal plane (i.e., the dispersion plane), with respect to the optical axis. All optical faces were antireflection coated to minimize spurious reflections from the zeroth- and second-order diffracted beams. The one-dimensional (1D) half-inch mSHRS used 300 grooves/mm gratings blazed at 500 nm, with the grating angle set by the spacers, to give a 529.4 nm Littrow wavelength (spacer angles of 4.555^{o}). The half-inch mSHRS device is about 2.2 x 2.2 x 1.3 cm in size and weighs about 17 g.

Figure 5.1 shows the half-inch mSHRS spectrometer setup that was used to measure Raman spectra using a 180^{o} back scatter geometry along the with an inset, I, image of the half-inch mSHRS in reference to a US quarter and the original monolith. A 532 nm continuous wave (CW) neodymium-doped yttrium aluminum garnet laser (Opto Engine, MGL-FN-532nm-1W) was used as the excitation source for all spectra shown,

with laser power on the sample of 150 mW. For all sample studies, the laser beam was directed onto the sample using a 50 mm diameter, 550 nm long-pass dichroic mirror, M_1, (ThorLabs, DMLP550L) at 45^o, then focused onto the sample using a 25.4 mm, NBK coated, f/4 achromatic lens, L_1, (Thorlabs AC254-100-A). The same lens also collected the Raman scattered light and collimated it, sending the signal into the mSHRS through two mm circular apertures, I_1, placed approximately 25 mm apart, to ensure beam collimation. Two filters (F), a 532 nm long-pass filter (Semrock RazorEdge, LP03-532RE-25) and a 532 nm holographic notch filter (Thorlabs, NF533-17) were placed in front of the mSHRS to remove strong laser scatter. A back-illuminated thermoelectrically cooled charge-coupled device (CCD) detector, UV-enhanced CCD detector with 2048x512, 13.5 um pixels, dark current of 0.001 e-/p/s, and a system read noise of 3.5 e-rms (Princeton Instruments-PI, PIXIS-2048 2K/BUV), cooled to -70 ^{o}C, ran at 100 kHz with ADC gain high and in the low noise setting, and controlled using Lightfield 6.3 software was used to image the grating faces onto the CCD detector at a magnification of 2.5x so as to fill as much of the detector in the horizontal direction as possible. The magnified image filled 1845 pixels in the horizontal direction. For all measurements, a spatial filter, I_3, was placed one focal length behind the imaging camera lens, L_2, on the CCD side, to block higher mSHRS grating diffraction orders. All data processing was done using MatLab version 2020b and Igor Pro 8.

5.3 Samples

Sodium sulfate (Sigma-Aldrich) were purchased at 99% purity and pressed into pellets using a hydraulic pellet press (Carver Laboratory Equipment, model 3912) with a 13mm

stainless steel pellet die. Cyclohexane (Sigma-Aldrich) with 99% purity were measured in 1 cm quartz cuvettes.

5.4 Results and Discussions

Light entering the SHRS is split into two beams by the beam splitter. The beams strike the tilted diffraction gratings and are diffracted back along the same direction. The beams re-enter the beam splitter and recombine to produce a wavelength dependent fringe pattern. The grating tilt angle defines the Littrow wavenumber, the wavenumber at which both beams exactly retro-reflect and produce no fringe pattern at the detector.[10] For any wavelength other than Littrow, the recombined light produces a crossed wave front, of which the crossing angle is wavenumber dependent and produces an interference pattern at the interferometer output. This output is then imaged onto the detector, and the spectrum is revealed upon Fourier Transform. The interference pattern produced on the CCD is an image of vertical fringes with intensity as a function of detector position as shown in Eq.1:

$$I(x) = \int_0^\infty B(\sigma)[1+\cos\{8\pi(\sigma-\sigma_L)x\tan\theta_L\}]d\sigma \qquad 5.1$$

Where $I(x)$ is the intensity distribution of the fringe pattern as a function of the detector position, $B(\sigma)$ is the input spectral intensity at wavenumber σ, σ_L is the Littrow wavenumber, and θ_L is the Littrow angle. The number of fringes, f, across the CCD is related to the Littrow wavenumber by Eq. 2:

$$f = 4(\sigma-\sigma_L)\tan\theta_L \qquad 5.2$$

Where f is in fringes/cm and σ wavenumber of interest. The resolving power, R, is determined by the total number of grooves illuminated on the two gratings shown in Figure 4.1. Eq. 3:

$$R = 2Wd \quad (5.3)$$

where W is the width of the grating and d is the grating groove density (grooves/mm). The theoretical maximum bandpass of the SHRS is determined by the resolving power, R. Figure 5.2 and 5.3 show Raman spectra of sodium sulfate and cyclohexane respectively. Figure 5.2 (a) and 5.3 (a) are half-inch mSHRS measurements compared microRaman measurements with a 150 um confocal hole size and a 600 grooves/mm grating 5.2 (b) and 5.3 (b). The insets, I, are the cross section of the half-inch mSHRS spectra. The full width half max (FWHM) of the 992 cm^{-1} sodium sulfate Raman band was 8.9 cm^{-1} and 5.0 cm^{-1} for the half-inch mSHRS and the microRaman respectively and the FWHM of the 801 cm^{-1} cyclohexane Raman band was 9.8 cm^{-1} and 5.1 cm^{-1} for the half-inch mSHRS and the microRaman respectively. The Nyquist limit sets the highest fringe frequency that can be measured by the detector to the frequency that produces N/2 fringes.[1] The theoretical bandpass, BP, can be calculated using Eq. 4:

$$BP = N\lambda/2R \quad (5.4)$$

Where N is the number of pixels in the horizontal direction, λ is the Littrow wavelength, and R is the resolving power. For the half-inch mSHRS the grating groove density is 300 grooves/mm with a 7 mm spot size on R is 4200. With 1581 pixels being covered on the detector the theoretical band pass, BP, is approximately 2800 cm^{-1}. The measured spectral range is show in figure 5.4. Due to the limitations of running a sample that had a band around 2800 cm^{-1} only a spectral range of up to 2200 cm^{-1} was measured. Figure 5.4 shows Raman spectra of (a) acetaminophen and (b) acetonitrile using a half-inch mSHRS. This shows the measured spectral range up to the 2250 cm^{-1} acetonitrile band. The collection solid angle can be shown in Eq. 5:

$$\Omega = 2\pi/R \quad (5.5)$$

This makes Ω approximately 1.5×10^{-3} sr giving an acceptance angle of 2.2^0.

Compared to conventional Raman spectrometers, the optical throughput, or optical Etendue determines the maximum Raman sensitivity for a given laser power. The optical Etendue of the mSHRS is several orders of magnitude higher than conventional slit based Raman spectrometers of the same resolving power. The amount of light that can be collected by an optical system, the optical Etendue, is shown in Eq. 6:

$$E = \Omega A \quad (5.6)$$

where Ω (in sr) is the collection solid angle of the system and A (in cm^2) is the area viewed. The large entrance aperture of the mSHRS allows for very large diameter fibers to be used. [3,4] This is especially significant for measuring solids or opaque samples because it makes it easier to maintain the proper working distance from the probe to sample and it minimizes changes in measured intensity for small changes in the probe to sample distance. The sensitivity, however, of the SHRS is related to the fringe visibility (FV) as defined in Eq. 7:

$$FV = (I_{max} - I_{min})/(I_{max}+I_{min}) \quad (5.7)$$

where I_{max} is the maximum cross-section intensity and I_{min} is the minimum cross-section intensity. The FV was 0.16 and 0.25 for sodium sulfate and cyclohexane respectively. Bands with larger wavenumber shifts produce higher frequency fringes because of the symmetry in Eq. 2. Spectral features at wavenumbers both above and below Littrow overlap on the detector, and this can cause band overlap. This can be eliminated by adding a bandpass filter but, if wavelengths above and below Littrow are desired,

degeneracy can be avoided by tilting one grating vertically, producing a rotation of the fringe pattern clockwise for bands below Littrow and counterclockwise for bands above Littrow. A 2D Fourier Transform of the resulting interferogram recovers the spectrum with no ambiguity and this technique can also be used to double the spectral range of the SHRS without increasing the number of CCD pixels used.[2] Recently new method was demonstrated for recovering 2D spectra using a mSHRS with one grating rotated around the optical axis.[28]

SHRS measurements have been demonstrated using a complementary metal oxide semiconductor (CMOS) detector in a cell phone and showed that uncooled CMOS detectors offer similar SNR to that of a cooled CCD.[5] Therefore, the size of the detector allows the use of a small low-power CMOS detector, similar to that of a cell phone detector, but cooled. Overall, the half-inch mSHRS offers many advantages over the conventional dispersive Raman systems. These advantages include 10 to 100 times larger acceptance angle, 10^2 to 10^4 higher light throughput, very high spectral resolution, a wide spectral range, and its robustness.[5,6]

5.5 Conclusion

The development of a small, ruggedized ocean Raman spectrometer will require reducing the size of the three main components, the detector—usually a CCD, the laser, and a wavelength discriminator (e.g., a monochromator, spectrograph, or interferometer). This chapter demonstrated on a miniature monolithic Spatial Heterodyne Spectrometer (half-inch mSHS), about 2.2 x 2.2 x 1.3 cm in size and weighing about 17 g, used as the wavelength discriminator in a Raman spectrometer (mSHRS), in a 1D configuration. The spectral resolution of the 1D mSHRS is shown to be about of 8 - 10 cm^{-1}. Although

standard size collection and imaging optics were used with the half-inch mSHRS in these studies, the use of miniature optics should be possible since the resolution of the half-inch mSHS is not a function of size. The use of smaller optics, such as a small diode laser and a small CMOS detector, has previously been demonstrated,[5, 28] should make possible the development of sensitive, high resolution miniature Raman spectrometer.

5.6 References

1. C.V. Raman, "A Change Of Wave-Length In Light Scattering" Nature. 1928. 121-619.
2. S.K. Sharma, "Applications of advanced Raman techniques in earth science". Vibrational Spectra Structure. 1989. 17B: 513-568.
3. A. Wang, J. Han, L. Guo, J. Yu, P. Zeng, "Database of standard Raman-spectra of minerals and related inorganic crystals". Applied Spectroscopy. 1994. 48: 959-968.
4. A. Degen, G. A. Newman, "Raman-Spectra Of Inorganic-Ions". Spectrochimica Acta Part A. 1993. 49:859-887.
5. P. McMillan, A. M. Hofmeister "Infrared and Raman spectroscopy of minerals, in Spectroscopy in Mineralogy and Geology". Reviews of Mineralogy. 1988. 18: 99-159.
6. K. Nakamoto, "Infrared and Raman Spectra of Inorganic and Coordination Compounds". John Wiley and Sons, New York. 1997. 5th ed.
7. S.N. White, R. M. Dunk, E. T. Peltzer, J. J. Freeman, P. G. Brewer, "In situ Raman analyses of deep-sea hydrothermal and cold seep systems (Gorda Ridge and Hydrate Ridge)". Geochemistry Geophysics Geosystems. 2006. 7(5).

8. X. Zhang, P.M. Walz, W.J. Kirkwood, K.C. Hester, W. Ussler, E.T. Peltzer, P.G. Brewer, “Development and deployment of a deep-sea Raman probe for measurement of pore water geochemistry”. Deep-Sea Research. 2010. (1)57: 297–306.
9. X. Zhang, P.M. Walz, W.J. Kirkwood, K.C. Hester, W. Ussler, E.T. Peltzer, P.G. Brewer. “In situ Raman-based measurements of high dissolved methane concentrations in hydrate rich ocean sediments”. Geophysical Research. 2011. 38: L08605.
10. X. Zhang, W.J. Kirkwood, P.M. Walz, E.T. Peltzer, P.G. Brewer. “A Review of Advances in Deep-Ocean Raman Spectroscopy”. Applied Spectroscopy. 2012. 66: 237-249.
11. X. Zhang, Z. Luan, C. Chen, J. Yan. “Development of an in situ Raman spectrometer for measurement of sediment pore water geochemistry in a high-pressure reaction cell”. Oceans - San Diego. 2013. 23-27
12. J. Pasteris. “The laser Raman microprobe as a tool for the economic geologist, Applications of microanalytical techniques to understanding mineralizing processes”. M.A McKibben, W.C Shanks, W.I Ridley (Eds.). 1998. 233–250.
13. J.D. Pasteris, J.J. Freeman, S.K. Goffredi, K.R. Buck. “Raman spectroscopic and laser scanning confocal microscopic analysis of sulfur-precipitating marine bacteria”. Chemical Geology. 2001. 180:3–18.
14. J.D. Pasteris, B. Wopenka, J.J. Freeman, P.G. Brewer, S.N. White, E.T. Peltzer, G.E. Malby. “Raman Spectroscopy in the Deep Ocean: Successes and Challenges”. Applied Spectroscopy. 2004. 58:195A- 208A.

15. D. Yang, J. Guo, Q. Liu, Z. Luo, J. Yan, R. Zheng, “Highly sensitive Raman system for dissolved gas analysis in water”. Applied Optics. 2016. 55(27):7744-7748.
16. S. Yu, X. Li, W. Lu, H. Li, Y.V. Fu, F. Liu. “Analysis of Raman Spectra by Using Deep Learning Methods in the Identification of Marine Pathogens”. Analytical Chemistry. 2021. 93(32): 11089–11098.
17. J. Guo, W. Ye, Q. Liu, F. Qi, K. Cheng, D. Yang, R. Zheng, “Development of a compact deep-sea Raman spectroscopy system and direct bicarbonate detection in sea trials” Applied Optics. 2019. 58(10):2630-2634.
18. T. Dohi, T. Suzuki. “Attainment of High Resolution Holographic Fourier Transform Spectroscopy”. Applied Optics 1971. 10(5): 1137 – 1140.
19. J. M. Harlander. Spatial Heterodyne Spectroscopy: Interferometric Performance at Any Wavelength without Scanning. [Ph.D. Dissertation]. Madison, WI: University of Wisconsin-Madison, 1991.
20. N.R. Gomer, et.al., “Raman Spectroscopy Using a Spatial Heterodyne Spectrometer: Proof of Concept”. Applied Spectroscopy. 2011. 65:849-857.
21. N. Lamsal, S.K. Sharma, T.E. Acosta, et al. ‘‘Stand-off UV and Visible Raman Measurements Using a Gated Spatial Heterodyne Raman Spectrometer’’. Applied Spectroscopy. 2016. 70(4): 666–685.
22. N. Lamsal, S.M. Angel. ‘‘Deep-Ultraviolet Raman Measurements Using a Spatial Heterodyne Raman Spectrometer (SHRS)’’. Applied Spectroscopy. 2015. 69(5): 525–534.
23. N. Lamsal, S.M. Angel, S.K. Sharma, et al. ‘‘Visible and UV Stand Off Raman Measurements in Ambient Light Conditions Using a Gated Spatial Heterodyne

Raman Spectrometer''. Paper 1459, presented at: LPSC 2015. Woodland, TX; March 16–20, 2015.

24. P.D. Barnett, N. Lamsal, S.M. Angel. ''Standoff Laser-Induced Breakdown Spectroscopy (LIBS) Using a Miniature Wide Field of View Spatial Heterodyne Spectrometer with Sub-Microsteradian Collection Optics''. Applied Spectroscopy. 2017. 71(4): 585–590.
25. I.B. Gornushkin, B.W. Smith, U. Panne, et al. ''Laser-Induced Breakdown Spectroscopy Combined with Spatial Heterodyne Spectroscopy''. Applied Spectroscopy. 2014. 68(9): 1076–1084.
26. A.N. Allen, A.M. Waldron, J.M. Ottaway, et al. ''Hyperspectral Raman Imaging Using a Spatial Heterodyne Raman Spectrometer with a Microlens Array''. Applies Spectroscopy. 2020. 74(8).
27. M. Foster, J. Storey, P. Stockwell, et al. ''Stand off Raman Spectrometer for Identification of Liquids in Pressurized Gas Pipelines''. Optics Express. 2015. 3968(8): 730–740.
28. A. Waldron, A. Allen, A. Colón, J.C. Carter, S.M. Angel. "A Monolithic Spatial Heterodyne Raman Spectrometer: Initial Tests". Applied. Spectroscopy. 2021. 75(1): 57-69.
29. A.K. Strange Fessler, A. Waldron, A. Colón, C.J. Carter, S.M. Angel, "A demonstration of spatial heterodyne spectrometers for remote LIBS, Raman spectroscopy, and 1D imaging". Spectrochimica Acta Part B. 2021. 178.
30. E.M. Kelly, M.J. Egan, A. Colón, S.M. Angel, S.K. Sharma. "Remote Raman Sensing using a Single-Grating Monolithic Spatial Heterodyne Raman

Spectrometer—A Potential Tool for Planetary Exploration" Applied Spectroscopy. In press 2022.

31. T.F. Cooney, H.T. Skinner, S.M. Angel. "Comparative Study of some Fiber-Optic Remote Raman Probe Designs. Part I: Model for Liquids and Transparent Solids". Applied Spectroscopy. 1996. 50: 836-848.
32. T.F. Cooney, H.T. Skinner, S.M. Angel. "Comparative Study of some Fiber-Optic Remote Raman Probe Designs. Part II: Tests of Single-Fiber, Lensed, and Flat- and Bevel-Tip Multi-Fiber Probes". Applied Spectroscopy. 1996. 50:849-860.
33. P.D. Barnett, S. M. Angel, "Miniature Spatial Heterodyne Raman Spectrometer with a Cell Phone Camera Detector" Applied Spectroscopy. 2016. Vol. 71(5) 988–995.

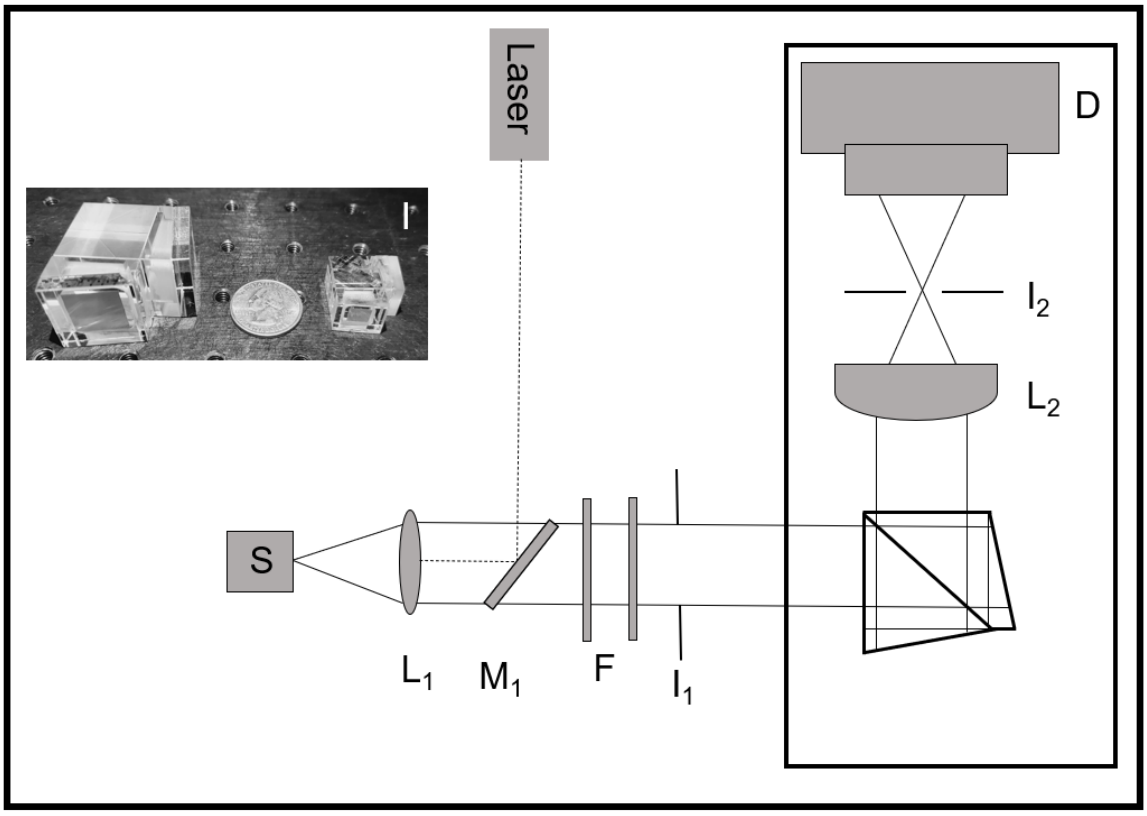

Figure 5.1 Schematic diagram of the mSHRS system. S: sample; L_1: collection lens; M_1: dichroic mirror; F: filters, I_1: iris, L_2: imaging lens, I_3: spatial filter; D: CCD detector. The inset, I: is an image of the miniature mSHRS in reference to a US quarter and the original monolith.

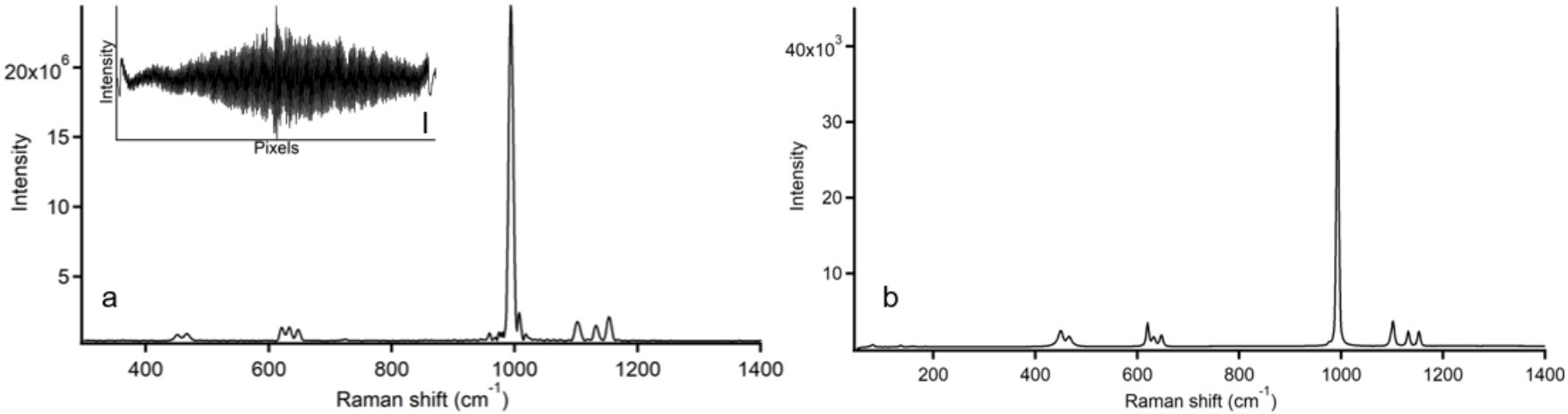

Figure 5.2 Raman spectra of (a) sodium sulfate using a half-inch mSHRS (529.4 nm Littrow, 300 grooves/mm) and (b) sodium sulfate using a microRaman. Exposure time was 60 s for each measurement. The insert shows the cross section for sodium sulfate. The fringe visibility was 0.16.

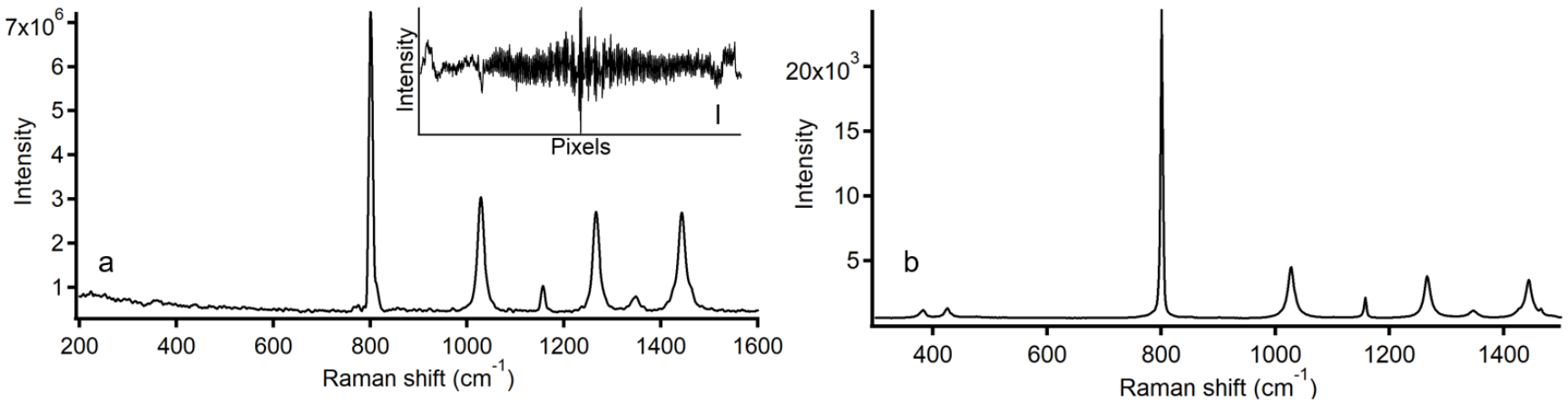

Figure 5.3 Raman spectra of (a) cyclohexane using a half-inch mSHRS (529.4 nm Littrow, 300 grooves/mm) and (b) cyclohexane using a microRaman. Exposure time was 60 s for each measurement. The insert shows the cross section for sodium sulfate. The fringe visibility was 0.16.

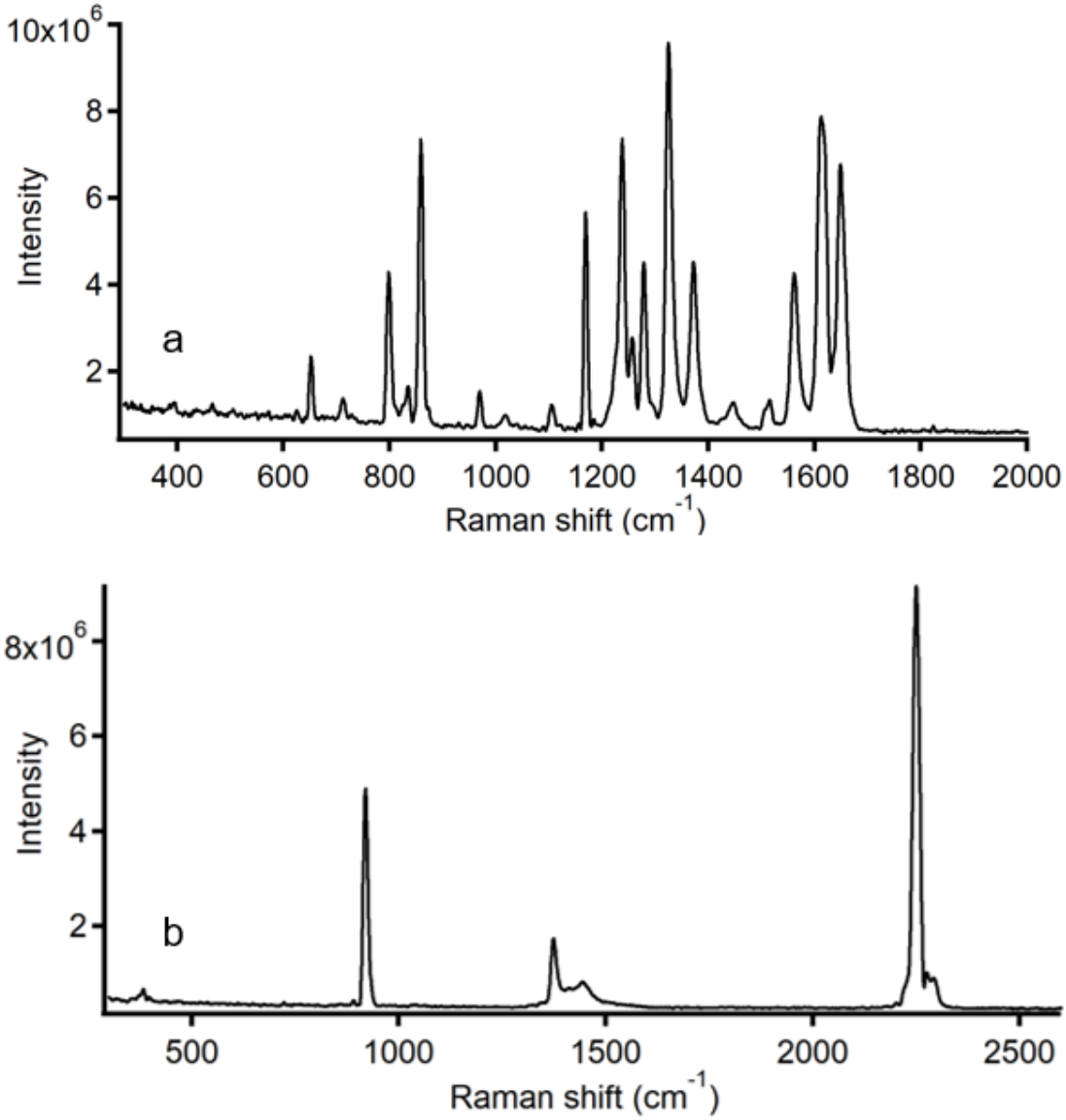

Figure 5.4 Raman spectra of (a) acetaminophen and (b) acetonitrile using a half-inch mSHRS. This shows the measured spectral range up to the 2250 cm^{-1} acetonitrile band.

APPENDIX A: PUBLICATIONS

I.M. Raimundo Jr. S.M. Angel, A. Colón, "Detection of Low Lithium Concentrations using Laser-Induced Breakdown Spectroscopy (LIBS) in High Pressure and High-Flow Conditions" Applied Spec. 2021. 75(11).

Summary

This paper described the effects of laser pulse rate and solution flow rate on the determination of low lithium concentrations at high pressure for water and 2.5% sodium chloride solutions using laser-induced breakdown spectroscopy (LIBS). Preliminary studies were performed with 0-40 ppm Li solutions, at ambient pressure and at 210 bar, and in static and flowing (6 mL $\cdot$ min^{-1}) conditions, for a combination of four different measurement conditions. The sensitivity of calibration curves depended on the pressure and the flow rate, as well as the laser pulse rate. The sensitivity of the calibration curve increased about 10% and 18% when the pressure was changed from 1 to 210 bar for static and flowing conditions, respectively. However, an effect of flow rate at high pressure for both 2 and 10 Hz laser pulse rates was observed. At ambient pressure, the effect of flow rate was negligible, as the sensitivity of the calibration curve decreased around 2%, while at high pressure the sensitivity increased around 4% when measurements were performed in a flow regime. Therefore, it seems there is a synergistic effect between pressure and flow rate, as the sensitivity increases significantly when both changes are considered. When the pulse rate is changed from 2 to 10 Hz, the sensitivity increases 26-31%, depending on the pressure and flow conditions. Lithium detection limit studies were performed with a laser pulse energy of 2.5 mJ, repetition rate of 10 Hz, gate delay of 500

ns, gate width of 1000 ns, and 1000 accumulations. A contentration around 40 ppm was measured for Li solutions in pure water for all four measurement conditions, while a detection limit of about 92 ppm was determined for Li in 2.5% sodium chloride solutions, when high pressure and flowing conditions were employed. The results demonstrated that LIBS is a powerful tool for the determination of Li in deep ocean conditions such as those found around hydrothermal vent systems. Eight different experimental conditions were implemented; static and flow (6 mL min^{-1}) regimes, low (1 bar) and high (210 bar) pressures, and low (2 Hz) and high (10 Hz) pulse rates. For pulse rates of 2 and 10 Hz, the effect of flow rate seemed to be negligible at ambient pressure. The sensitivity increased around 10% and 18% when the pressure was changed from 1 to 210 bar in both static and flowing conditions, respectively, indicating a synergistic effect between pressure and flow rate, as the sensitivity increases significantly when both changes are considered. Increasing the pulse rate from 2 to 10Hz increased the sensitivity from 26 to 31%, depending on the pressure and flow conditions. The determination of Li in low concentrations was performed in water and 2.5% NaCl solution, employing with a laser pulse energy of 2.5 mJ, repetition rate of 10 Hz, gate delay of 500 ns, gate width of 1000 ns, and 1000 accumulations, allowed to achieve detection limits as low as 40 and 92 ppm, respectively.

Contribution to the paper

My contributions to this paper involved mimicking preliminary test and aiding in writing the paper. A summary of my experimental set up and preliminary data is described.

A LIBS system combined with a custom-built high-pressure cell was employed in this study. Figure 1 shows the optical set up. A pulsed laser source (5 ns, Continuum Surelite III Nd:YAG, with a frequency doubling crystal for 532 nm) ran at 2 Hz and 20 mJ of power, a polychromator (Chromex Model 250IS/RF, f/4, 300 grooves/mm, blazed at 1000 nm, slit of 100 µm) and a thermoelectric cooled -25ºC ICCD detector (Princeton Instruments I-Max 1024-E, 1064x256 pixels). The diameter of the laser pulse was first expanded to 2", with a plano-concave lens (1" diameter, focal distance -1"), before being directed to the sample with a dichroic mirror (Thorlabs DMLP550L). The laser pulse was focused into the sample with a biconvex lens; the radiation emitted by the plasma was collected by the same lens and focused onto the optical fiber tip with a 2-mm core, to be guided into the polychromator. The laser pulse energy was adjusted with the laser power control unit, while the repetition rate, gate delay, and gate width were controlled by a BNC model 555 pulse generator. Spectra were acquired with the aid of Winspec32 software, which allowed the adjustment of the number of runs for obtaining a spectrum, the number of spectra, and the ICCD detector gain, among other parameters. The optical system was properly aligned, and the alignment was evaluated by obtaining an emission of a metal copper sample.

The laser pulse was focused into a custom-made stainless steel flow cell with an internal volume of 40 mL with a sapphire window (diameter 25 mm, thickness 6.35 mm). Stainless steel tubing (diameter of 1/8") connected to an HPLC pump (LC5000, Isco) was used to flow the solution throughout the system. The system pressure was adjusted with a proportional relief valve (Swagelok R3A series), which was automatically opened when the pressure rose higher than the back-pressure provided by an internal spring. Figure 2 shows the diagram for operating the flow system. To fill up the pump, valve V_1 must be

closed, while valve V_3 is kept open. To pump the solution into the measuring cell, valves V_2 and V_3 are closed, while valve V_1 is opened. Valve V_4 must be kept open to perform measurements at ambient pressure; if it is closed, the pressure inside the system is controlled by adjusting the pressure of the internal spring of the relief valve. Valve V_2 is used to drain the measuring cell, with the aid of a syringe. As the cell volume (40 mL) is much higher than the maximum flow rate provided by the pump (6.7 mL min^{-1}), draining the cell using only the pump is both inefficient and time consuming.

The lithium (Li) aqueous solutions that will be shown were measured at experimental conditions, 1 ppm Li concentrations at 1 atm of pressure and 40 ppm Li and 40 ppm sodium (Na) solution at 1 atm and 100 atm of pressure. These preliminary tests were done to test the optimal gating for the detection of Li in low and high concentrations. Only up to 100 atm of pressure were measured due to issues with sealing the pressure cell. The figure labeled figure A.3 shows the optimal gate width and gate delay in a 1 ppm Li solution for the 670 nm line. This was tested by using various gate delays in combination with two gate width times 1 us and 2 us. A gate delay of 440 ns and gate width of two us seem to provide the best signal for lithium. The figure labeled figure A.4 shows the optimal gate delay for the determination of 40 ppm concentration of Li in a 40 ppm Na solution. figure A.4 (a) is measured at 1 atm of pressure and (b) is measured at 100 atm of pressure. The arrow in figure A.4 (a) points at the 598 nm sodium line which is not as prominent when a pressure of 100 atm is implemented like in figure A.4 (b). A gate delay of 380 ns and gate width of 2 us were used for both studies.

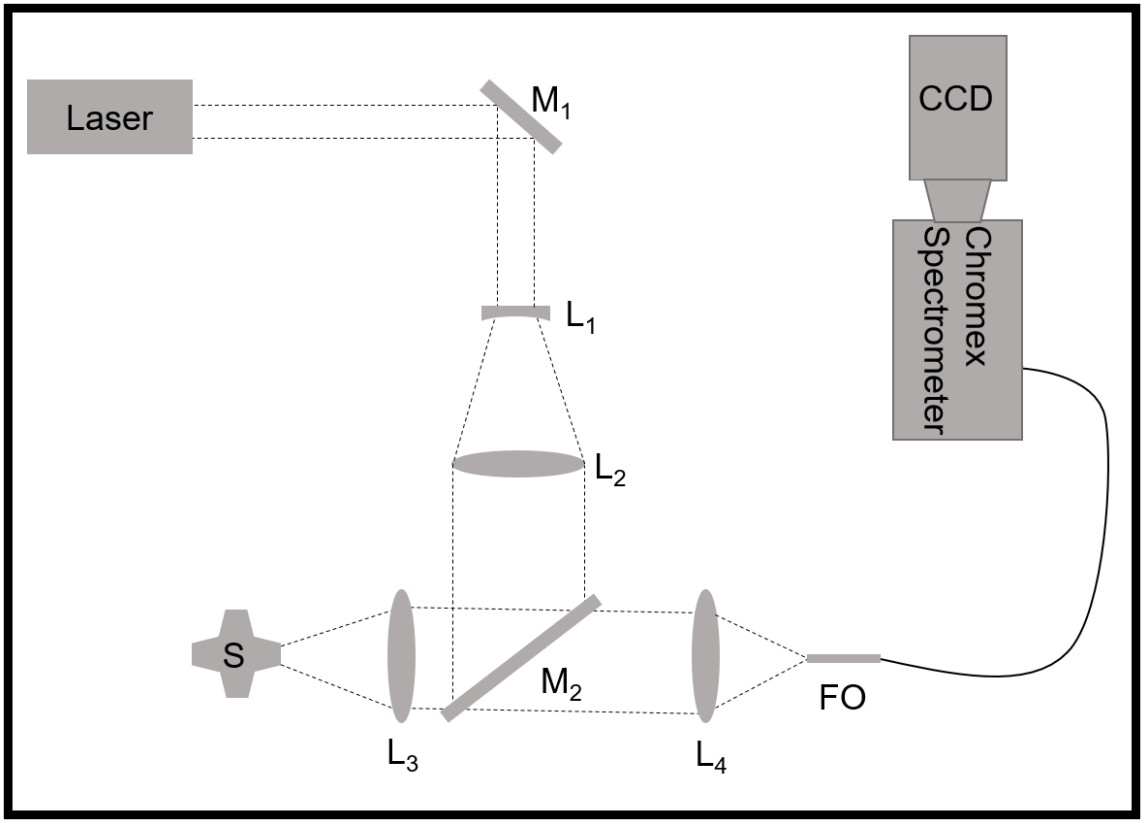

Figure A.1 Schematic diagram of the LIBS high pressure system. S: sample cell, L_1: negative lens, L_2: positive lens, L_3: sample focusing and collimating lens, L_4: fiber optic focusing lens, M_1: reflection mirror, M_2: dichroic mirror; FO: fiber optic, D: CCD detector.

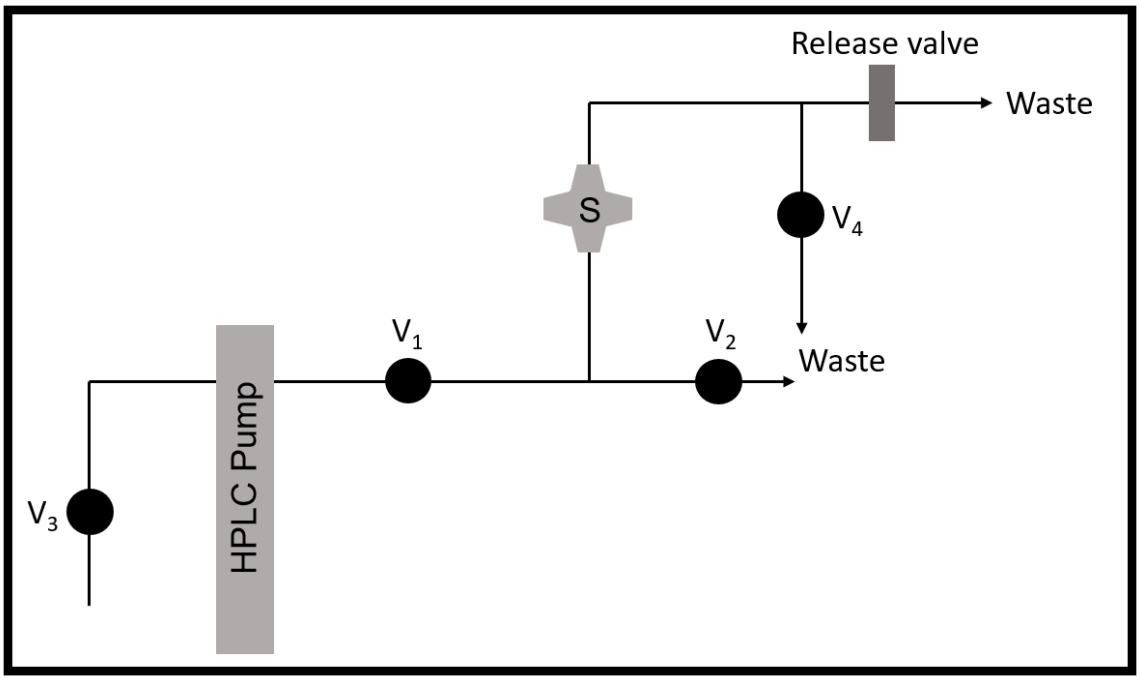

Figure A.2 Diagram of the flow system for LIBS measurements (V_1-V_4, manual valves).

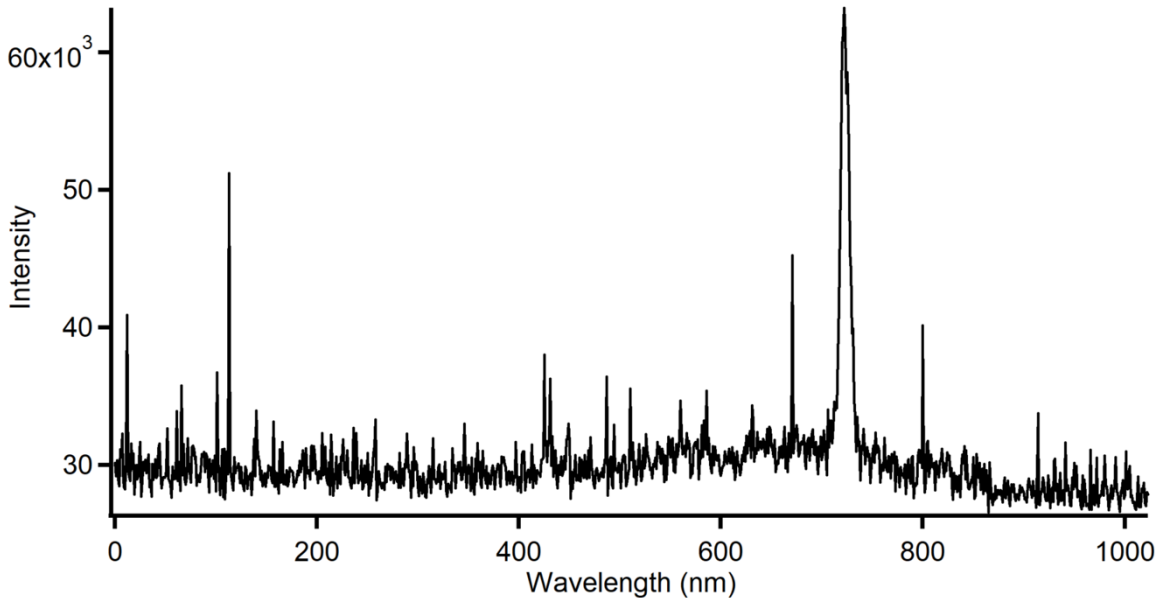

Figure A.3 Lithium at 1 ppm concentration at ambient pressure (1 atm). Gate width 2 us and gate delay 440 ns.

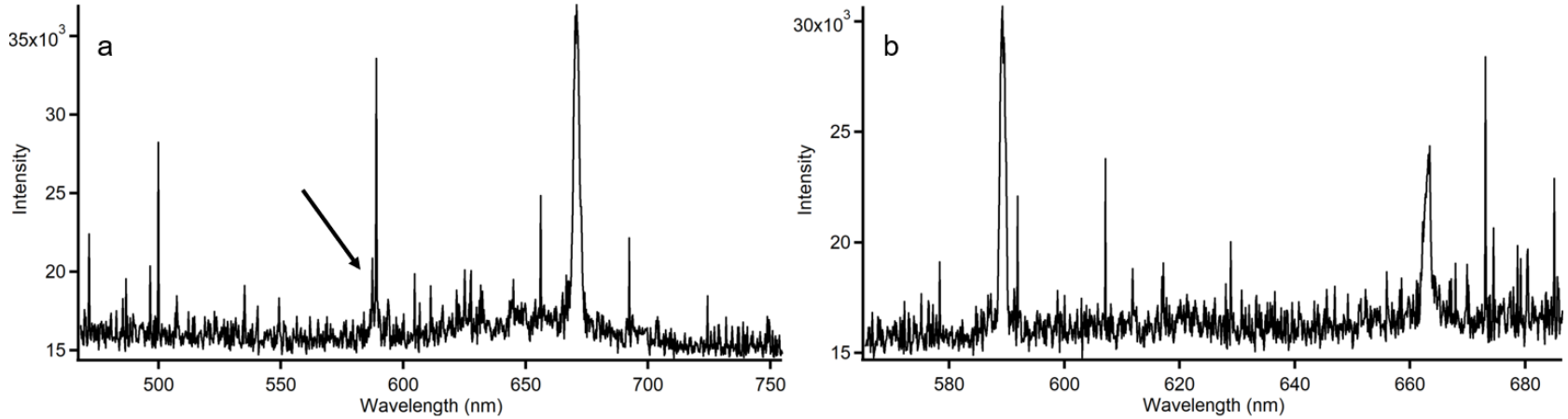

Figure A.4 40 ppm sodium and 40 ppm sodium solution at (a) 1 atm and (b) 100 atm. The gate delay was 380 ns and gate width was 2 us for both studies.

APPENDIX B: MatLab Code

This code is used for running cross-dispersed monolithic Spatial Heterodyne

Spectroscopy row by row blocked grating data. The files should be in “spe” format.

```
clear
Xpixels=1024;
Ypixels=256;
Type='uint32';

[filename, path] = uigetfile('*.*', 'choose Raw image SPE file');

FilenameRaw = strcat(path,filename);
fid = fopen(FilenameRaw);
status = fseek(fid,4100,'bof');

a = fread(fid,[Xpixels,Ypixels],Type);%
fclose(fid);
Raw = a';

[filename, path] = uigetfile('*.*', 'choose grating 1 blocked SPE file',path);
FilenameG1B=strcat(path,filename);
fid = fopen(FilenameG1B);
status = fseek(fid,4100,'bof');
b = fread(fid,[Xpixels,Ypixels],Type);

fclose(fid);
g1b = b';

[filename, path] = uigetfile('*.*', 'choose grating 2 blocked SPE file',path);

FilenameG2B = strcat(path,filename);
fid = fopen(FilenameG2B);
status = fseek(fid,4100,'bof');
c = fread(fid,[Xpixels,Ypixels],Type);%
fclose(fid);
g2b = c';

[filename, path] = uigetfile('*.*', 'choose both gratings blocked SPE file',path);
```

```
FilenameBGB = strcat(path,filename);
fid = fopen(FilenameBGB);
status = fseek(fid,4100,'bof');
d = fread(fid,[Xpixels,Ypixels],Type);
fclose(fid);
bgb = d';

image_corr = Raw-(g1b+g2b)+bgb;

f=image_corr(1:512,1:2048);

mean=mean(image_corr,1);
meanMatrix= repmat(mean,512,1);
RawminusMean= image_corr-meanMatrix;

spectrum_2D = abs(fft(f,[],2));
spectrum = sum(spectrum_2D);

%% Plot spectrum
figure;
plot(spectrum,'f');
xlim([10 2048]);
title('spectrum');
xlabel('Pixels');
ylabel('intensity');

copy = spectrum';
```